PROPERTY MEASUREMENTS AND MOISTURE DIFFUSION SIMULATIONS DURING POTASH CAKING AND CAKE STRENGTH PREDICTIONS

A Thesis

Submitted to the College of Graduate Studies and Research

in Partial Fulfillment of the Requirement for the Degree of

Master of Science

In the Department of Mechanical Engineering

University of Saskatchewan

Saskatoon

By

Shaoyu Gao

PERMISSION TO USE

In presenting this thesis in partial fulfilment of the requirements for a Postgraduate degree from the University of Saskatchewan, I agree that the Libraries of this University may make it freely available for inspection. I further agree that permission for copying of this thesis in any manner, in whole or in part, for scholarly purposes may be granted by the professor or professors who supervised my thesis work or, in their absence, by the Head of the Department or the Dean of the College in which my thesis work was done. It is understood that any copying or publication or use of this thesis or parts thereof for financial gain shall not be allowed without my written permission. It is also understood that due recognition shall be given to me and to the University of Saskatchewan in any scholarly use which may be made of any material in my thesis.

Requests for permission to copy or to make other use of the material in this thesis in whole or part should be addressed to:

Head of the Department of Mechanical Engineering

University of Saskatchewan

Saskatoon, Saskatchewan (S7N 5A9)

ABSTRACT

Researchers have demonstrated that the hygroscopicity of bulk potash exposed to humid air causes the adsorption and condensation of water vapour on potash particle surfaces. The accumulated water forms liquid bridges near contact points between potash particles and dissolves salt impurities on potash particle surfaces until the brine bridges are saturated. When the ambient air becomes dry, the accumulated water evaporates, the dissolved salt recrystallizes, and the crystalline bridges form between potash particles. A sufficient number of crystal bridges per unit volume in bulk potash can cause strong potash cakes. This can lead to costly handling problems. It is the purpose of this research to investigate the effects of external compressive load and ambient air humidity on caking properties and cake strengths of bulk potash during long duration storage. The research is separated into the four parts: discrete element modelling, potash sample preparation and fracture testing, simulation of water vapour diffusion into test cells, and cake strength correlations.

The discrete element method (DEM) was used to predict the tensile force distributions on particles and cake strength of a compressed potash ring specimen when the specimen is fractured in the centrifuge. In the planar DEM model, a tensile force concentrating on an inter-particle contact region can be transformed to the local-averaged tensile stress distributed on the equivalent cross section corresponding to the particle. The local-averaged tensile stresses are consistent with the microscopic tensile stresses in the solid continuum model when the Poisson's ratio is small. The DEM model indicates that the tangential tensile forces are the main factor causing fractures of potash specimens while the radial tensile forces are insignificant. The uniform tangential tensile forces imply that the fracture interface of a specimen should be parallel to the radial direction of the specimen (i.e. normal to the main tensile force).

During sample preparation, potash ring specimens were subjected to four nominal sample depths (0, 4, 8, and 16 m) and three values of moisture adsorption humidity (69, 75, and 84%). Two values of moisture desorption humidity (52 and 11%) were used to make crystal bridges in the potash samples. Test sample preparation periods from weeks to months were used. Springs

were used to generate the external compressive loads equivalent to the nominal sample depths. The caking properties of potash specimens, such as mass, height, porosity, and moisture content, were measured during sample preparation. After caking, specimens were ruptured in the centrifuge to test their fracture rotary speeds. Data for fracture rotary speed were input into the DEM model to compute cake strengths of potash specimens. The data analyses showed that the higher external equivalent loads during sample preparation cause the bigger variations of sample height and porosity. The moisture content of potash specimens was determined by the moisture adsorption and desorption humidity. When the moisture adsorption humidity was not higher than 75%, cake strengths of potash samples were enhanced with an increase of the external equivalent load. If the moisture adsorption humidity reached 84%, the external load hardly affected the potash cake strength.

A numerical model of water vapour diffusion with the boundary condition of free mass convection was developed for two sub-groups of uncompressed potash specimens corresponding to those with the complete and reduced top sample surfaces exposed to the ambient air. The numerical model predicted the spatial distributions of local relative humidity and moisture content in transient states inside a potash specimen and the variations of free mass convection coefficient and macroscopic sample moisture content over time. The predictions of sample moisture content for the two sample sub-groups were in agreement with the corresponding experimental data. The big free mass convection coefficient during moisture desorption meant a high mass transfer rate near the potash sample top surface. The almost uniform spatial distributions on the maximum and residual local moisture contents in a potash specimen showed that the variations of local moisture content were similar inside the specimen during moisture adsorption and desorption. It was also expected that the crystal bridges forming in the specimen after caking were analogous.

A correlation was developed to predict cake strengths of potash specimens by using the ambient air humidity for moisture adsorption and desorption and the external equivalent load. The upper limitations of relative humidity and external load were 75% and 16 m. The correlation showed that cake strength of potash specimens was enhanced with an increase of moisture adsorption relative humidity conditions and external load, and with a decrease in moisture desorption relative humidity conditions.

ACKNOWLEDGMENTS

I would firstly express my sincerest respect and gratitude to my supervisors, Professor Robert W. Besant and Professor Richard W. Evitts. It is the two professors who offer me the important opportunity for the development of my career. Their persistence on research pursuits deeply impresses me. Their patience and encouragement make me full of self-confidence. Their wisdom and knowledge lead me to academic success.

The same thankfulness is shown to my advisory committee members, Professor David A. Torvi and Professor Reza Fotouhi and my external examiner, Professor Leon D. Wegner. Their constructive suggestions make my scope wider and my research more reasonable.

The hearty appreciation is expressed to Dr. Xiaodong Nie and Mr. Anton Siaotong, PhD student, for their unselfish assistance with my thesis writing.

The thanks are shown to Mr. Dave Deutscher and Mr. Rick Retzlaff who provide me with necessary technical supports on experimental measurements and equipment calibrations.

I am also grateful to the Natural Science and Engineering Research Council of Canada (NSERC) and the Potash Corporation of Saskatchewan (PCS) for their financial support.

DEDICATION

This thesis is dedicated to my wife, Xinping Wang.

TABLE OF CONTENTS

LIST OF TABLES

LIST OF FIGURES

NOMENCLATURE

ENGLISH SYMBOLS

A	Correlation coefficient or Cross section area of potash crystal bridge [m^2]
A_b	Top surface area of a potash specimen [m^2]
A_{cr}	Contact area between idealized potash particles in the radial direction [m^2]
A_{ct}	Contact area between idealized potash particles in the tangential direction [m^2]
A_p	Nominal cross section area of a potash particle
A_{sl}	Area of the cross section through the short axis of an idealized potash particle [m^2]
a	Exponential constant for correlation
a_{cr}	long radius of elliptic contact region in the radial direction [mm]
a_{ct}	long radius of elliptic contact region in the tangential direction [mm]
B	Correlation coefficient
b	Exponential constant for correlation
b_{cr}	short radius of elliptic contact region in the radial direction [mm]
b_{ct}	short radius of elliptic contact region in the tangential direction [mm]
C	Correlation coefficient
c	Exponential constant for correlation
D	Correlation coefficient
D_v	Diffusion coefficient of water vapour in air [m^2/s]
$D_{v,eff}$	Effective diffusion coefficient of water vapour in a potash specimen [m^2/s]
d_p	Short axis diameter of and idealized ellipsoidal potash particle [mm]
d_{pcl}	Curvature circle diameter at the end of long axis of an ideal potash particle [mm]

d_{pm} Mean value of short axis diameters of idealized ellipsoidal potash particles [mm]

E The Young's modulus of potash crystal bridge [Pa]

F Tensile force on a contact region between potash particles [N]

F_b Tensile fracture force of crystal bridge [N]

F_c Centrifugal force [N]

F_{el} External load [N]

g Gravity acceleration [m/s^2]

H External load equivalent to nominal sample depth [m]

h Potash sample height [m]

h_{ic} Initial compressed potash sample height [mm]

h_{if} Initial free potash sample height [mm]

h_{ca} Post-adsorption compressed potash sample height [mm]

h_{cd} Post-desorption compressed potash sample height [mm]

h_m free convection coefficient for mass transfer [m/s]

k Stiffness coefficient of crystal bridge [N/mm]

L Length of potash crystal bridge [m]

L_c Characteristic length of potash specimen [m]

m_d Post-desorption dried potash sample mass [kg]

m_i Initial dry potash sample mass [kg]

m_l Mass of water accumulated in a potash sample [kg]

m_w Post-adsorption wetted potash sample mass [kg]

$\dot{m}$ Mass rate of phase change per unit volume [kg/m^3·s]

N Quantity of idealized potash particles in a radial direction

n Exponential constant or quantity of potash particles in a ring

P_a Partial pressure of dry air [Pa]

P_{atm} Atmosphere pressure [Pa]

P_b Top surface perimeter of a potash specimen [m]

P_c Compressive contact force at the end of long axis of an ideal potash particle [N]

P_{sv} Saturation pressure of water vapour [Pa]

P_v Partial pressure of water vapour [Pa]

q Number of forces concentrating on a common object

R Universal gas constant [kJ/(kmol·K)]

Ra The Rayleigh number

R_a Dry air constant [J/(kg·K)]

R_{bi} Inner radius of a potash ring specimen [m]

R_{bo} Outer radius of a potash ring specimen [m]

R_c Radius at the center of an idealized potash particle or ring radius of a potash specimen [m]

R_m Average radius of a potash ring specimen [m]

R_v Water vapour constant [J/(kg·K)]

r_b Cross section radius of crystal bridge [m]

r_{cl} Contact region radius at the end of long axis of an ideal potash particle [mm]

$\hat{r}$ Correlation coefficient of linear regression

S characteristic parameter [$min^{0.4}$·mm^{-2}] or random error of measurement

S' Modified characteristic parameter [$mm^{0.96}$]

Sc Schmidt number

Sh Sherwood number

T Constant room temperature for potash specimens and ambient air [K]

t Sample storage time [day]

t_a Moisture adsorption time constant for potash specimens [min] or [day]

t_d Moisture desorption (drying) time constant for potash specimens [min] or [day]

t_o Dimensionless sample storage time

U Uncertainty of measurement

V_b Liquid bridge volume [m3]

W_c Complementary work [J]

W_e Elastic work [J]

X Potash sample moisture content [%]

X_e Maximum potash sample moisture content [%]

X_i Post-adsorption maximum potash sample moisture content [%]

X_o Dimensionless potash sample moisture content

X_r Post-desorption residual potash sample moisture content [%]

X_m Correlation coefficient

x Vertical height coordinate in a potash ring specimen or grid size [m]

GREEK SYMBOLS

β Angle corresponding to an idealized potash particle

δ Displacement of force [m]

δ_{cl} Deformation at the end of long axis of an idealized ellipsoidal potash particle [mm]

δ_{cs} Deformation at the end of short axis of an idealized ellipsoidal potash particle [mm]

ε Tensile strain or porosity of potash ring specimen

ε_{ic} Initial compressed potash sample porosity

ε_{if} Initial free potash sample porosity

ε_{ca} Post-adsorption compressed potash sample porosity

ε_{cd} Post-desorption compressed potash sample porosity

ε_g	Volume fraction of gas phase in a potash ring specimen
ε_l	Volume fraction of liquid phase in a potash ring specimen
ε_s	Volume fraction of solid phase in a potash ring specimen
ε_{sl}	Strain on the cross section through the short axis of an idealized potash particle [Pa]
ε_{ss}	Strain in the short axis direction of an idealized potash particle [Pa]
η	Equation coefficient
λ	Empirical coefficient
ν	Dynamic viscosity of air [m^2/s]
ρ_a	Partial density of dry air [kg/m^3]
ρ_b	density of potash ring specimen [kg/m^3]
ρ_g	Total gas density [kg/m^3]
ρ_l	Water density [kg/m^3]
ρ_p	Density of an idealized potash particle [kg/m^3]
ρ_s	Density of potash crystal [kg/m^3]
ρ_v	Partial density of water vapour [kg/m^3]
σ	Tensile stress [Pa]
σ_b	Tensile fracture strength of crystal bridge [Pa]
σ_c	Cake strength of a potash specimen [Pa]
σ_{sl}	Uniform compressive stress on the cross section through the short axis of an idealized potash particle [Pa]
τ	Tortuosity of potash ring specimen
υ	Poisson's ratio
Φ	Complementary energy [J]
Φ_s	Total complementary energy [J]

ϕ Relative humidity in a potash ring specimen [%]

ϕ_A Relative humidity for moisture adsorption [%]

ϕ_D Relative humidity for moisture desorption [%]

ϕ_∞ Relative humidity in ambient air [%]

ω Fracture rotary speed of a potash specimen [rad/s]

Γ_c Dimensionless radius corresponding to R_c

Δ Variation of physical parameter

Δh_r Relative difference of potash sample height between h_{ic} and h_{cd} [%]

Δt Time step [s]

ΔX Maximum difference of potash sample moisture content between X_i and X_r [%]

$\Delta \varepsilon_r$ Relative difference of potash sample porosity between ε_{ic} and ε_{cd} [%]

$\Delta \rho_{g,eff}$ Effective difference of total gas density [kg/m^3]

Θ Dimensional centrifuge load factor

Ψ Dimensionless tensile force a contact region between potash particles

Ω Dimensionless stress corresponding to F and Ψ

SUPERSCRIPTS

i Number of ideal potash particle in the radial direction or Number of ring inside a specimen

k Number of force

l Number of displacement

SUBSCRIPTS

m Mean value

p Potash particle

r Radial direction in a potash ring specimen

s Total of a physical parameter

t	Tangential direction in a potash ring specimen
∞	Ambient air

CHAPTER 1

INTRODUCTION

1.1 Background

Bulk potash products are used as fertilizers to maintain good potassium levels in soil because potassium is a crucial chemical element to improve yield, quality, and disease resistance of crops (Garrett, 1996). For example, granular potash fertilizer is widely applied to banana plantations in tropical regions because bananas need high potassium levels. Forage crops rich in potassium are essential feeds for livestock as well. People must ingest sufficient levels of potassium from food to keep good health. With the environmental deterioration, arable land decrease, and food shortage on a worldwide scale, the potash industry has an extensive market prospect in the global economy.

Canada has a widespread potash resource, mainly in Saskatchewan. Canadian potash producers annually export bulk potash fertilizer by ship and rail to many countries, e.g. China, India, Brazil, and others, where agriculture plays a significant role in their national economy. During a series of processes of potash production, transportation, storage and usage, bulk potash particles with a wide range of particle sizes from 0.5 mm to 5 mm (Figure 1.1(a)) are piled together outdoors and indoors where the stored potash is exposed to ambient conditions for weeks or months. It is often found that significant fractions of the irregular-shaped potash granules near the air-potash interfaces of the stored potash are agglomerated to form strong cakes after exposure to alternating high and low ambient air humidity. These cakes have properties like that of solids, as shown in Figure 1.1(b). Because caked bulk potash is not uniformly spread in soil by agricultural machines, the potassium content in soil cannot be effectively utilized (Garret, 1996).

The study of caking mechanism and the measurement and prediction of cake strength for bulk potash are of some concern to potash companies because these theoretical and experimental research investigations can offer the information useful to reduce the caking and the associated costs. The literature in Sections 1.2 and 1.3, respectively, show the recent research developments related to caking and cake strength.

(a) (b)

Figure 1.1 Bulk potash products: (a) irregular-shaped potash granules and (b) solid potash cakes

1.2 Mechanism of Potash Caking

Caking is a common physical phenomenon for many types of granular media. Seville et al. (1997) presented that mechanical interactions inside granular media are classified into elastic contacts, viscous forces, intermolecular forces, electrostatic forces and multi-phase bonding forces. For caked bulk potash, crystal bridges make potash particles strongly agglomerated together. Substantial research presented in Section 1.2.1 reveal that the hygroscopicity of bulk potash causes moisture condensation and evaporation processes in potash granular specimens. These processes are coupled with variations in the temperature and humidity in bulk potash. Once water vapour is adsorbed and condensed on potash granules, the accumulated water will be concentrated near contact points between particles by surface tension and changed to saturated brine bridges with salt dissolution. When most of the water is evaporated in a dry environment, the salt in brine bridges will be recrystallized to form crystal bridges. In other words, the heat and moisture transfer causes salt recrystallization and crystal bridge formation in potash

specimens. Rumpf (1958) pointed out that the number and strength of crystal bridges inside a granular sample determine the macroscopic tensile strength of the sample. Some research that has contributed the understanding of salt recrystallization and bridge formation is presented in Section 1.2.2.

1.2.1 Heat and mass transfer

Potash is composed of sylvite (KCl), with the small quantities of halite (NaCl) and carnallite (KMgCl3·6H2O) and other soluble salts (Garrett, 1996). Peng et al. (1999) found that potash could adsorb water vapour from the surrounding air when the relative humidity was 52% or higher. This is a critical relative humidity, the lower bound, for occurrences of potash moisture adsorption. Because potash granular products are often transported to tropical regions, these potash products will inevitably experience cyclic moisture adsorption and desorption processes which are accompanied by variations of temperature and humidity.

Peng et al. (2000) designed an experimental setup to study the convective heat and moisture transportation in a potash bed through which the humid air passed at constant flow rates. A numerical model corresponding to the experimental setup was developed. Because of being in agreement with the numerical results of Burch et al. (1976), the model was demonstrated to be applicable for the convective heat and mass transfer in a potash granular bed. Experimental data showed that the bed temperature was higher than the humid air flowing through a bed and the humid air became drier after passing through the bed. It was also found that the enthalpy change inside a potash granular bed was obviously different from the latent heat of water vapour condensation especially during the initial experimental stage.

Peng et al. (2001) continued to use the experimental setup mentioned above to investigate the enthalpy change caused by the adsorption and condensation of water vapour and the dissolution of salt on potash particle surfaces during convective heat and moisture transfer. They thought that the enthalpy change was impacted by the moisture content, the environmental humidity, the potash chemical and physical properties (e.g. composition and specific area) and the ambient air temperature. Two groups of potash granules with the two average particle diameters of 0.8 mm and 2.2 mm were used. The correlations between the enthalpy change and

the low moisture content for a potash bed were obtained. The enthalpy change results determined by using the correlations were in agreement with the experimental data of Hansen et al. (1998) under their measurement uncertainties. The correlations indicated that the enthalpy change of bulk potash particles was bigger compared with the heat of vaporization for water within the low moisture content ranges. While the moisture content continued to increase, the enthalpy change would decrease and approximate to heat of vaporization for water with the difference of 15% because of the influence of the heat of solution for salt.

Zhou (2000) designed an experimental apparatus to study the heat conduction and moisture diffusion processes in a potash bed with forced humid air convection on the top surface of the bed. He measured the altered properties of the potash bed during experimentation. Zhou developed a numerical model to predict the variations of temperature and moisture content inside a potash bed. His numerical solutions were in agreement with the corresponding experimental data. On the basis of Peng's work, Zhou developed a multistage isothermal correlation between equilibrium moisture content and relative humidity.

Chen (2004) developed correlations to predict physical properties of dry potash particulate beds with wide particle size distributions by using experimental data of potash specimens prepared for small particle size ranges. He defined an important concept, irreducible saturation, the critical value of which implied the variation of moisture transportation mechanism inside bulk potash. Water vapour diffusion dominated the moisture adsorption and water condensation processes in a potash bed before the irreducible saturation reached its critical value. The water capillarity and gravity sustained moisture movements in the same bed after the irreducible saturation exceeded its critical value. Applying the irreducible saturation, Chen developed two numerical models to show local moisture content variations in a potash bed with the two moisture transfer mechanisms.

1.2.2 Crystal bridging between particles

Tanaka (1978) designed a model of two ideal spherical particles in contact to obtain the mathematical expressions for the geometric conditions of a liquid bridge. He assumed that the bridge volume and shape remained constant as the liquid bridge was transformed to the

corresponding crystal bridge after recrystallization. He thought that the cake strength of particle media depended on the particle size, the number of contact points per unit volume, and the fracture force of crystal bridges. His theoretical results and experimental data showed an agreement within the same order of magnitude of his data. Tanaka pointed out that the cake strength was proportional to the square root of the initial moisture content of a particle bed.

Sun et al. (2006) measured the tensile fracture force of two crystal particles connected by recrystallized salt. The two particles, in contact at the smooth interface, were placed in a sealed container to experience moisture adsorption and desorption processes for a preset period. Subsequently, the two agglomerated particles were taken out of the sealed container and fractured by a measured external load. The average fracture stress and the number of crystal bonds on a contact surface were determined by the fracture force, the contact surface area, and the tensile strength and cross section area of crystal bond. The experiments were repeated separately for two kinds of salt material, NaCl and KCl. The experimental data showed that a small fraction of the contact interface was connected by recrystallized salt. Sun showed the AFM image about the rough contact surfaces of fractured particles. Data of contact surface roughness qualitatively characterized the crystal bonds on the contact interface between agglomerated particles.

Wahl et al. (2008) used an apparatus, termed as Device to Apply Pressure on Particles (DAPP), to produce a pair of fertilizer particles in contact. A liquid/crystal bridge at the contact point was generated with the alternation of humid/dry ambient air. The sizes and tensile fracture force of the crystal bridge were measured after particle agglomeration. The experimental process was reproduced with the variations of environmental humidity, moisture adsorption time, external load, and granular material, such as NPK-fertilizer, Enzyme, and Urea. Their data showed that the diameters and fracture forces of crystal bridges were enhanced by the extension of moisture adsorption time and the increase of environmental temperature. They also illustrated that the critical relative humidity, causing moisture adsorption, decreased while the environmental temperature rose. Wahl demonstrated that the liquid bridge at a contact point could be sufficiently transformed to the crystal bridge occupying the whole contact region in a

long moisture desorption period. Otherwise, a small amount of salt was recystallized from the liquid bridge and deposited around the contact point.

Wang et al. (2008) developed a numerical model to investigate the recrystallization processes affected by the following three factors: initial moisture content, evaporation rate, and supersaturation degree of liquid bridge. Their numerical results showed that the higher initial moisture content and the slower evaporation rate were able to cause more salt to be deposited at contact points. Similarly, the higher supersaturation degree of liquid bridge made more salt accumulated near contact points. Their numerical results are qualitatively consistent with the experimental data on cake strength of Wang et al. (2006). Their research supplied the fundamentals of recrystallization modeling for more complex contact conditions.

1.3 Mechanical Strength of Caked Potash Granules

1.3.1 Strength measurement of consolidated granular cake

Several typical test apparatus, such as Jenike shear cell (ASTM Std. D6128-06), Schulze ring shear tester (ASTM Std. D6773-08), and uniaxial caking tester (Schwedes et al. 2003), are used to measure compressive and shear strengths of caked granular specimens. Shear cells shown in Figure 1.2 (a) and (c) require external normal and shear loadings. The uniaxial tester shown in Figure 1.2 (b) needs an external compressive force. Caked bulk granules, behaving like a brittle solid material, are more easily fractured by external tensile loadings relative to the compression failure (Budynas 1999, Tomas 2004). Measurements for the tensile strength of caked bulk granules are worthwhile for the handling and use of caked granular products. Some researchers developed their own tensile strength testing setups.

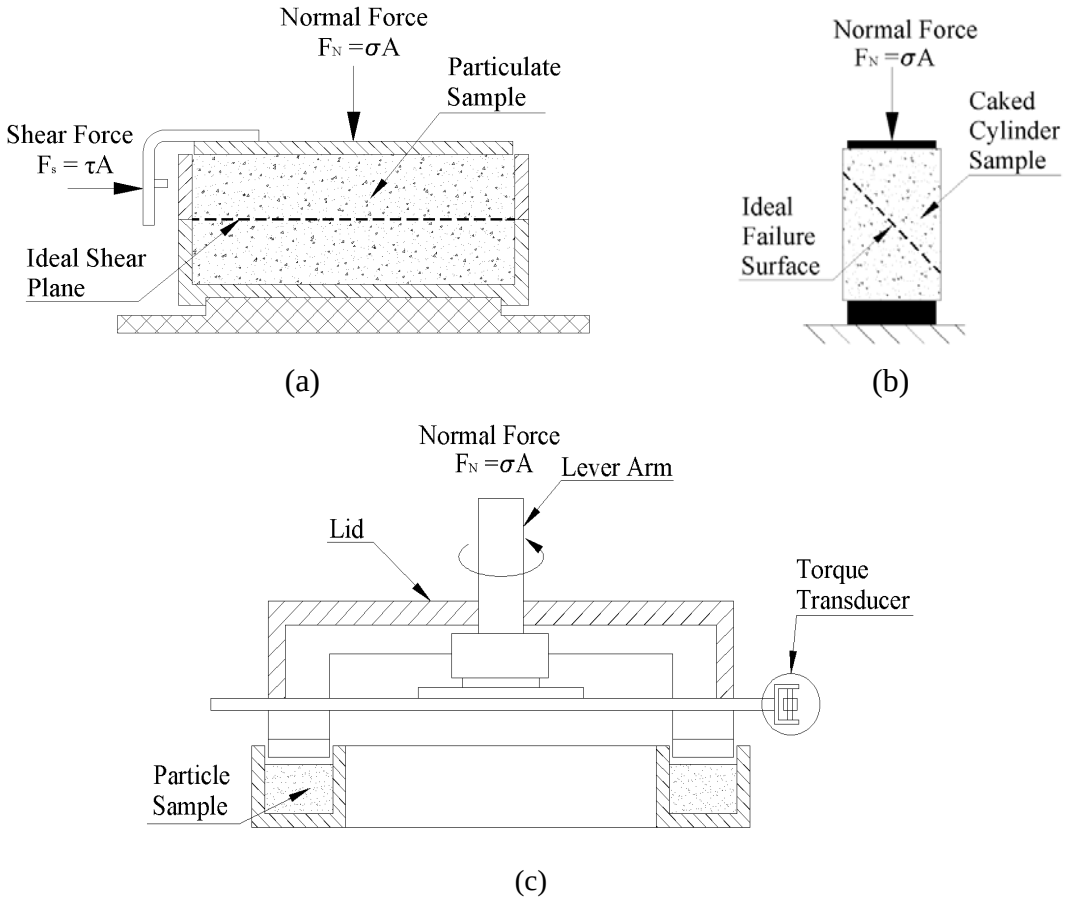

Figure 1.2 Strength testers of caked particle materials: (a) Jenike shear cell, (b) uniaxial caking tester, (c) Schulze shear tester

Schweiger et al. (1999) designed their tensile strength test cell for lactose and corn powder. A watch glass slice was adhered to a powder sample by using white petrolatum as shown in Figure 1.3(a). After consolidation, the powder bed in the sample container was separated from the watch glass slice (Refer to Figure 1.3 (b)). The data acquisition cell was used to obtain the tensile force necessary to cause the separation and to calculate the tensile strength, which could quantify the cohesion of powder. Schweiger pointed out that the cohesion ratio between lactose and corn starch derived from the tensile strength test cell was consistent with the corresponding data measured by using Jenike shear cell. However, Schweiger' tensile test cell generated smaller tensile strength data than Jenike shear cell. Thus, it was shown that the two devices had their own systematic biases on the tensile strength measurements for powder media.

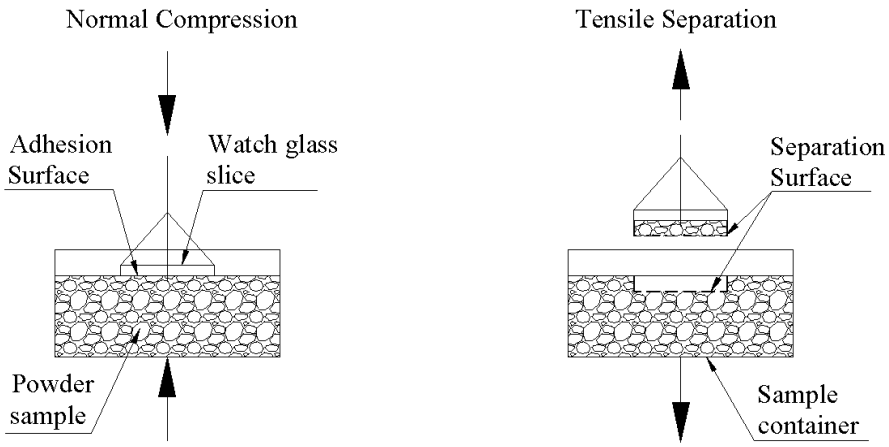

Figure 1.3 Schematic of the tensile strength test cell of Schweiger et al. (1999): (a) the adhesion of watch glass slice on a powder sample and (b) the fracture separation of watch glass slice from a powder sample

Leaper et al. (2003) developed a tensile strength test method for disc-like caked sugar granular beds (shown in Figure 1.4 (a) and (b)), which experienced multiple cyclic processes of moisture adsorption and desorption. Based on the research of Rumpf (1958) and Tanaka (1978), it was theoretically predicted that the tensile strength of a sugar bed was proportional to the square root of the number of moisture adsorption and desorption cycles. Their experimental data were in agreement with the theoretical correlation. Moreover, Leaper et al. used their experimental data to calculate the tensile strengths of sugar crystalline bridges.

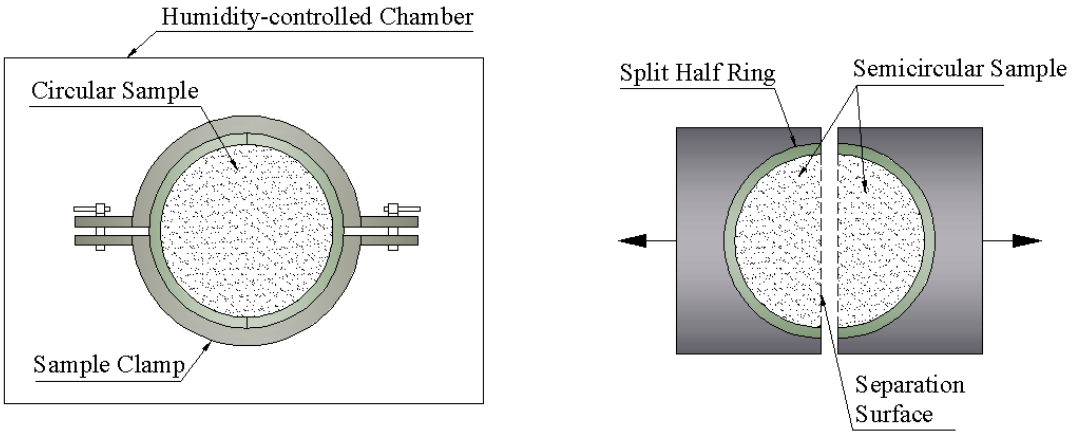

Figure 1.4 Schematic for the tensile strength test of Leaper et al. (2003): (a) the circular sugar granular sample preparation and (b) the sample separation

Wang et al. (2006) presented a centrifuge test method of cake strength for ring potash samples. They added a known amount of water into dry potash particles to preset the initial moisture content of potash granular specimens. Test samples were dried and caked using the three methods: static air drying with the relative humidity of 52%, oven drying, and dry air flow drying. These caked samples were fractured in the centrifuge. The sample fracture rotary speed was input into Wang's continuum model to compute the sample cake strength. The air flow drying method had the fastest drying rate. The static air drying process with the relative humidity of 52% was the slowest. The cake strength data of potash specimens showed that a slower drying rate resulted in stronger potash lumps. It was also found that the cake strength was linearly related to the initial moisture content.

1.3.2 Prediction for mechanical behaviour of granular cake

Tensile strength measurements for caked granules had to result in high costs of sample preparation. If a mathematical model uses limited fundamental data on physical properties of granular media to successfully predict the mechanical stresses inside caked particulate samples, the time and cost spent on sample preparations will be reduced. Analogous equations, separately presented by Rumpf (1958) and Tanaka (1978), can predict the average tensile strength for granular media by using the data on porosity, average particle size, and crystal bridge fracture force. Caked potash specimens always have different internal structures since irregular potash granules are randomly packed in each test cell. It is difficult to obtain sufficient experimental data about crystal bridge fracture force for potash specimens. Some other researchers developed their own numerical models to study the microscopic mechanical behaviour in caked granular media.

1.3.2.1 Current mathematical methods

Christakis et al. (2006) developed a numerical continuum model to predict the tensile strength of a sugar granular bed. The continuum model was based on the test sample preparation of Leaper et al. (2003). At first, they applied principles of the heat and moisture transfer in their model to study variational spatial distributions of local moisture content inside a sugar granular bed with multiple cyclic alternations of high and lower environmental humidity. Their numerical

results for local moisture content, Leaper's crystal bridge strength data, and equations of Tanaka and Rumpf were used to compute the tensile stress state and strength of the sugar bed. Christakis's numerical solutions for the tensile strength of sugar beds were consistent with the corresponding experimental data of Leaper under a small measurement uncertainty. Their continuum model demonstrated that the moisture content could determine the tensile strength of a sugar granular bed while the physical properties of sugar granules, such as crystal bridge fracture strength, porosity, and mean diameter, were kept constant.

Wang et al. (2006) presented a theoretical model to predict the stress state in a ring-shaped potash specimen rotationally ruptured in the centrifuge. Potash specimens were assumed to be elastic continua. The specimens were slowly accelerated in the centrifuge until they were fractured at almost constant rotary speeds. The fracture rotary speed data were input into Wang's model to compute the tensile stress states and cake strengths of the specimens. His theoretical solutions of tensile stress state showed that the tangential tensile stress was the main factor in the centrifugal fracture of potash ring specimens because it was much bigger than the radial tensile stress. Hence, the tangential tensile stress was used to determine cake strengths of potash specimens. However, the stress is not a physical property existing in a potash specimen rotating in the centrifuge. In other words, Wang's model cannot show the inter-particle contact behaviour inside a rotational specimen.

Wahl et al. (2008) developed the contact-dynamics model to estimate compressive failure strengths of granular media by using the strength data of crystal bridges between particles. They obtained the crystal bridge strength data through the DAPP test method mentioned in Section 1.2.2. The uniaxial tester was applied to measure the compressive failure strengths of cylindrical urea granular specimens. The results of contact-dynamics model are only in qualitative agreement with the data measured by the uniaxial tester. They thought that some physical factors, like adhesion, lead to the difference between experiment and simulation. Because the elastic compressed contacts between particles were neglected, the contact-dynamics model failed to characterize the inter-particle mechanical behaviour in a urea granular specimen.

1.3.2.2 Discrete element method

These known mathematical models have their own limitations on the simulation of solid granular agglomerates. Cundall et al. (1979) presented a mathematical method, termed as the Discrete Element Method (DEM), to describe the accelerations, velocities, and positions of particles in a dynamic particle system, on the basis of elastic collisions and deformations among particles. Iwashita et al. (2000) described the inter-particle mechanical behaviour such as spring force, viscous damping, friction, elastic torque, and slip, as shown Figure 1.5 (a) and (b). DEM has successfully predicted the mechanical behaviour of multiply dynamic granular systems.

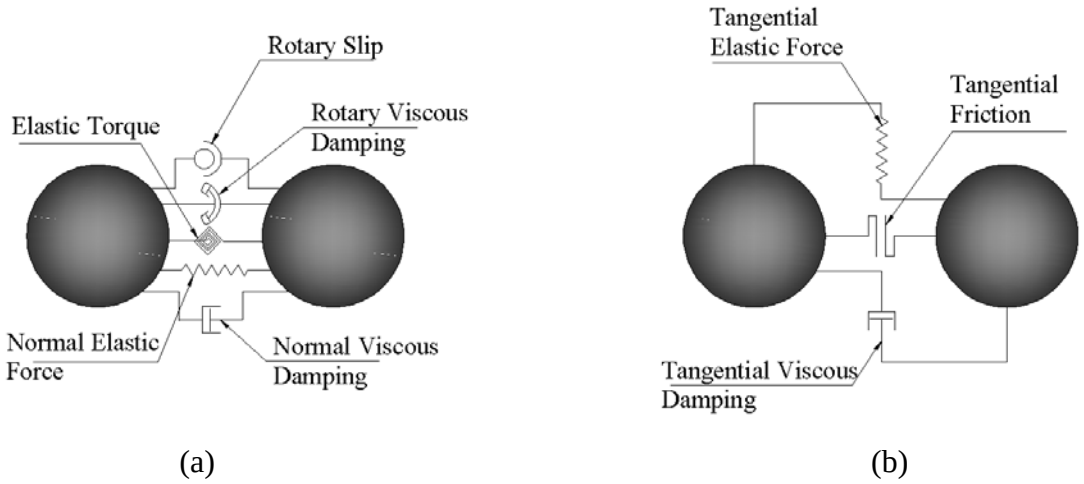

(a) (b)

Figure 1.5 Interactions between elastic particles (Iwashita et al. 2000): (a) normal elastic force, elastic torque, rotary slip, and normal/rotary viscous damping, (b) tangential elastic force, viscous damping, and relative friction

Kawaguchi et al. (1998) developed 2D and 3D models for bulk particle movements in fluidized beds. The local-averaged Navier-Stokes and continuity equations were used to describe the states of gas and solid phases in fluidized beds. The motions of bulk particles in their models were predicted by DEM. The interactions between gas and solid phases were thought of as the drag forces. The bulk particle movements, simulated by the 2D and 3D models, were in agreement with the physical phenomena demonstrated by the relevant experiments of fluidization in steady state. In addition, the 3D model could show the phenomenon of bulk particle stagnation near the corners of a fluidized bed, relative to the 2D model.

Li et al. (2003) used a DEM model to simulate the separation process of the mixed soybean and mustard seeds. Their DEM model was based on the vibrating screen, which had been used to sift granular materials in industry for a long time. Two mixed ratios of soybean and mustard seeds were respectively 1: 1 and 1: 84. By comparing simulation results for the two mixed ratios, they concluded that the soybean and mustard seeds, mixed by the latter ratio, had the higher separation efficiency, because there were more relative small mustard seeds to form continuous percolation flows through the bigger soybeans and sieving screen. Li et al. simultaneously observed kinetic behaviours of particles on the sieving screen. Thus, they thought that DEM is a preferable tool to investigate the separation principles of complex solid mixtures.

Following the successful applications of the Discrete Element Method on dynamic granular systems, researchers have begun to use it on quasi-static particulate media.

Ouwerkerk (1991) measured the compressive strength of a single porous silica granule. The criterion of crushing a single silica granule was the breakup into smaller fractions. A statistical distribution for the number of crushed silica granules and the compressive strength of single granule was used to determine the average compressive strength of a single silica granule. The compressive strengths of silica granular beds were tested according to the criterion that five percent of granules were crushed. His shear resistance test generated the experimental data on the varied mass percentage of ground silica particles with the increase of shear strain. Ouwerkerk applied TRUBAL, a computer code of the DEM developed by Cundall et al. (1979), to predict the particle displacements and contact force distributions inside compressed and sheared silica granular beds. The numerical results of compressive strength and shear strain computed by TRUBAL were consistent with the corresponding experimental data.

Kruyt et al. (2001) developed their DEM model for a static particle system, which was composed of 50,000 elastic particles under variational external compressive and shear loads. The microscopic mechanical behaviours between particles, such as relative displacement, contact force, and contact deformation, were predicted by the DEM model. The altered physical properties of the particle system loaded by compressive and shear forces, including contact number, porosity, system stiffness, and total elastic energy, could be statistically analyzed by the DEM model.

Gröger et al. (2003) developed a cohesive discrete element model (CDEM) to estimate the contact force distributions and average mechanical strengths inside a wetted particle bed with external static loads. The mechanical interactions between particles were considered to be the cohesive force of liquid bridge and the Hertzian contact force. They pointed out that tensile failure loci of agglomerated particulate materials were obtained by extrapolating measured strength loci in compression and shear states in many cases. Through changing the external static loads, their CDEM model was able to directly generate the whole yield loci of particle beds in compression, shear, and tension states. Furthermore, it was shown that the compressive and shear strength parts of the simulated yield loci were in a good agreement with the corresponding experimental data of Schulze et al. (2001).

1.4 Research Objectives

1.4.1 Introduction

In the literature review, it is evident that the physical properties of potash granules, such as porosity, moisture content, crystal bridge fracture strength, number of crystal bridges per unit volume and so on, could be factors in determining cake strength of potash specimens. Some researchers have developed correlations between physical properties and cake strength of potash. Data acquisition of the potash physical properties is the prerequisite for applications of these correlations to cake strength predictions of bulk potash.

Relative to recent literature, the current research is aimed to enhancing the knowledge base on potash caking process and cake strength. The experimental studies and numerical simulations in this work show that the effects of external load and ambient air relative humidity on the physical properties and cake strength of bulk potash.

1.4.2 Goals

This project was separated into four parts: fracture strength modelling, caked sample preparation and fracture test, moisture transfer simulation, and cake strength correlation. The DEM of Cundall et al. (1979) and the centrifuge method of Wang et al. (2006) were used respectively for the fracture strength modelling and the fracture test. Wang's sample preparation

process was modified by using loading springs and humidity-controlled chambers to prepare caked potash specimens in compression states. In order to accomplish all parts, the research objectives are stated as follows:

a) To develop a DEM model to predict the interparticle mechanical behaviour inside a potash specimen and compute the specimen cake strength;

b) To measure varied properties of compressed potash specimens, including mass, height, porosity, and moisture content, during sample preparation and analyse impacts of the external load and relative humidity on these properties. To test the fracture rotary speeds of caked potash specimens in the centrifuge, compute the cake strengths of specimens by using the DEM model, and study variations of cake strength caused by the external load and environmental humidity;

c) To develop a numerical model to predict moisture adsorption and desorption processes of uncompressed potash specimens during sample preparation and investigate the moisture transfer and accumulation within uncompressed potash specimens;

d) To build a correlation to estimate the cake strength of bulk potash with variations of the potash pile height and ambient air humidity by combining data analyses of potash mechanical properties and numerical simulations of moisture adsorption and desorption.

1.5 Thesis Overview

The thesis is organized in the order of listed research objectives and separated into six chapters to show the accomplishments of the objectives.

Chapter one makes a general introduction about the background information of potash industry, the present literature for potash particle systems, and the research objectives of this thesis.

Chapter two elaborates the DEM model used to predict inter-particle contact forces in a caked potash specimen. The DEM model is compared with the developed continuum model. The cake strength of potash sample is computed by the DEM model. In Appendix A, the complementary energy theory is used to formulate the geometry compatibility in the DEM model. The estimation on the contact area between compressed potash particles is shown in Appendix B.

Chapter three specifies the sample preparation course of compressed potash specimens and the fracture test of caked samples. Effects of the external load and environmental humidity on caking properties and cake strengths of potash samples are studied through the experimental data analyses. The relevant measurement uncertainties analyses are illuminated in Appendix C. The experimental data are shown in Appendix D.

Chapter four shows the numerical model of water vapour diffusion for the water vapour condensation and liquid water evaporation in a potash specimen without external compression. The numerical results of sample moisture content are compared with the relevant experimental data. The spatial distributions of local relative humidity and moisture content in transient state inside a specimen are shown during moisture adsorption and desorption. Physical properties of bulk potash and ambient air are listed in Appendix E. The numerical discretions of theoretical equations are specified in Appendix F.

Chapter five illuminates the effects of the caking properties of a potash specimen on the cake strength of the specimen. The correlation between cake strength, external load, and environmental humidity is presented.

In Chapter six, the summary and relevant conclusions of this research are enumerated. The future work is presented on the basis of this research.

CHAPTER 2

DEM SIMULATIONS ON FRACTURE TESTS OF COMPRESSED POTASH SPECIMENS

2.1 Introduction

2.1.1 Fracture tests for caked granular media

The potash caking can cause some problems, such as the cost increase of handling, the non-uniform fertilization, and the ineffective potassium absorption in soil (Garrett, 1996). Cake strength is used as the caking index of bulk potash to characterize the macroscopic mechanical behaviour of agglomerated potash specimens. The cake strength measurement is of primary concern to potash suppliers and researchers. The strength test apparatus, such as the Jenike shear cell (ASTM Std. D6128-06), the Schulze ring shear tester (ASTM Std. D6773-08), and the uniaxial caking tester (Schwedes et al. 2003) were extensively applied to measurements on the compressive and shear strengths of caked granular media. The brittle fracture is a common occurrence in caked bulk potash (Seville et al. 1997). The tensile fracture strength is worthy of being measured for caked bulk potash. Schweiger et al. (1999), Leaper et al. (2003), and Wahl et al. (2008) separately presented their own test apparatus and procedures for the tensile strength of caked granular media. These tensile strength testers have their own defects which cause significant systematic biases.

In the tensile strength test of Schweiger et al., a watch glass slice was used to adhere to the top surface of a powder sample. After consolidation, the glass slice, as well as a small fraction of powder was separated from the sample by a measurable tensile force as shown in Figure 1.3(a) and (b). Benenati et al. (1962) pointed out that the local porosity in surface regions of a granular specimen was higher than the internal porosity of the specimen. According to the

research of Rumpf (1958) and Tanaka (1978), it was concluded that the tensile force was affected by the porosity of a specimen. The tensile strength data obtained through the adhesion and separation of the glass slice on the top surface of a powder specimen cannot characterize the macroscopic mechanical behaviour in the specimen. Thus, Schweiger's tensile strength data of powder samples were lower relative to the data estimated by the extrapolation of the failure locus obtained by using the Jenike shear cell.

Leaper et al. (2003) exerted the known load on a split cell to break a caked sugar specimen in the cell into halves as shown in Figure 1.4(a) and (b). Wang et al. (2006) pointed out the flaw of the fracture test for caked bulk sugar. Wang et al. considered that the fracture of a caked sugar specimen possibly occurred at any position besides the interface preset by the split cell because the internal microscopic structures inside the specimen were randomly variable. Hence, it is expected that the preset fracture interface in a sugar sample can cause measurement deviations on the tensile strength of sugar sample.

Wahl et al. (2008) used the Device to Apply Pressure on Particles (DAPP) to measure the tensile fracture forces between caked fertilizer particles. They input the fracture force data of crystal bridges into their contact-dynamics model to compute the failure strengths of caked bulk fertilizers under uniaxial compression. In the contact-dynamics model, fertilizer particles were assumed to be in two modes, rigid contact and undeformed separation (i.e. brittle crystal bridge fracture). The numerical results of the model obviously differed from the data measured by using the uniaxial tester because the contact deformations between particles and the stretches of crystal bridges were neglected. If particles are irregular in shape (e.g. potash particles), a large number of DAPP fracture tests should be done to collect sufficient data on the fracture forces of various crystal bridges between irregular particles. Otherwise, the probability distributions for the fracture forces of crystal bridges cannot be obtained. It is impractical to test all of crystal bridges in various shapes. The neglect of contact deformations and crystal bridge stretches and the shortage of data on crystal bridge fracture forces are obstacles to apply the DAPP test and contact-dynamics model to multiple granular materials.

In order to eliminate the defects of the experimental setups mentioned above, Wang et al. (2006) presented a centrifuge test method to fracture caked potash particles configured into a

cylindrical ring and to collect data on fracture rotary speed. The centrifuge fracture test depends on the internal tension in a rotating ring specimen as the specimen is ruptured. That is to say, the random occurrences of fracture locations in Wang's centrifuge tests can avoid the systematic errors caused by the fractures artificially determined under external loadings. Finally, the data on fracture rotary speed were input into the solid continuum (SC) model developed by Wang et al. (2006) to predict the tensile stress distributions inside potash ring specimens and compute the cake strengths of specimens.

2.1.2 Application of DEM

The microscopic tensile stress used in the SC model is not a physical quantity which can describe the mechanical behaviour in a caked potash sample. Potash particles are agglomerated by inter-particle crystal bridges on contact regions. The cake strength of a caked potash sample should be determined by the tensile fracture forces and number of the crystal bridges inside the sample. As mentioned in Sub-section 1.3.2.2, the discrete element method (DEM) might be used to solve the deformation and loading of each crystal bridge in a potash sample by predicting the relative displacement, velocity, and acceleration of each particle. Hence, a DEM model is developed in this chapter to estimate inter-particle tensile forces and cake strengths for potash samples while Wang's centrifuge fracture test is used to measure the fracture rotary speed of the specimen.

2.2 DEM Modeling of Potash Ring Fracture

The DEM model can be applied to randomly arranged potash particles connected with one another by crystal bridges in a specimen if the physical properties of the crystal bridges, such as the Young's modulus, cross section sizes, and tensile fracture strength, are known. However, it is very difficult to measure these properties of crystal bridges inside a caked potash specimen since these crystal bridges are randomly shaped and orientated between irregular potash granules. DEM modelling for randomly distributed potash particles cannot be easily formulated.

Harr (1977) presented that the dominant inter-particle forces in a granular system determined the macroscopic mechanical behaviour of the granular system. That is to say, the

secondary mechanical behaviour between potash particles is insignificant. The literature of fracture mechanics (e.g. Felbeck et al. 1984) states that brittle materials tend to be unyieldingly fractured under normal tensile forces. The SC model of Wang et al. (2006) qualitatively revealed that the normal tensile forces tangential to a potash ring specimen resulted in the rupture of the specimen. When the secondary mechanical interactions between potash particles may be neglected, the DEM model should show how the tangential tensile forces fracture a caked potash specimen in the centrifuge.

2.2.1 Model assumptions

The potash granules compressed by a huge potash pile was the main concern in this research. A series of assumptions based on caked potash ring specimens under compression were applied in the DEM model.

a. Physical properties of caked potash

In a ring-like test sample, the geometric principal axes of irregular potash particles are almost evenly oriented in various directions, because each specimen cell is randomly packed with tens of thousands of potash particles. Potash specimens are assumed to be homogeneous and isotropic in the planar DEM model.

b. Application of idealized potash particulate elements

A group of idealized potash ellipsoids and spheres, in place of irregular potash particles in a potash specimen, are radially packed in the planar DEM model (Refer to Figure 2.1). These idealized potash particulate elements have the parallel planar stress tensors while the DEM model rotates at a given rotary speed. The sizes of idealized ellipsoidal and spherical particles are determined by the size range of bulk potash granules, the regular arrangement of idealized potash particles and the interval between inner and outer plastic rings (i.e. Parts 1 and 3 shown in Figure 2.1 (b)). Table 2.1 shows the sizes of idealized potash ellipsoids and spheres.

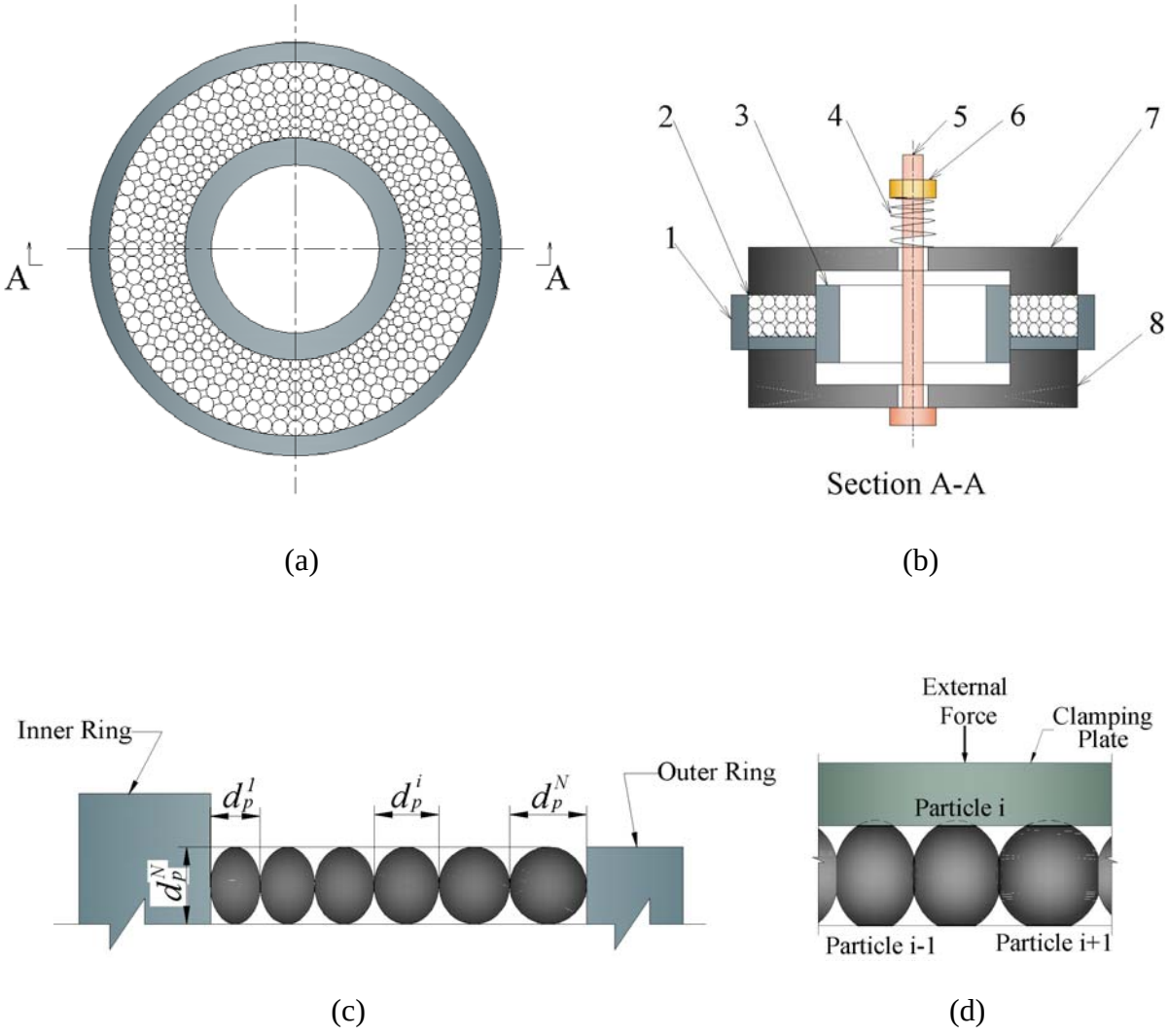

Figure 2.1 Schematics of the DEM model: (a) the planform of idealized planar DEM model, (b) the cross section of idealized DEM model during sample preparation, 1-outer plastic ring, 2-potash ring specimen, 3-inner plastic ring, 4-spring, 5-bolt, 6-nut, 7-top clamping plate, 8-bottom clamping plate, (c) a sequence of idealized potash ellipsoids and spheres in the radial direction, (d) the compressed contact regions on potash particles under an external force

Table 2.1 Dimensions of idealized potash ellipsoids and spheres for bulk potash granules with the size range of 0.9-1.18 *mm*

Element No. (*i*)	Short Axis Diameter of Ideal Particle (d_p^i) (mm)	Long Axis Diameter of Ideal Particle (d_p^{12}) (mm)
1	0.922	1.075
2	0.934	
3	0.948	
4	0.961	
5	0.974	
6	0.988	
7	1	
8	1.016	
9	1.03	
10	1.045	
11	1.06	
12	1.075	

c. Stiffness of potash particles

During the preparation of potash test samples under an external load, these idealized particles slightly deformed at each contact point in Figure 2.1 (d). The contact points were changed to the contact regions, on which the liquid/crystal bridges were mainly formed during sample preparation. These idealized ellipsoids and spheres are regarded to be fixed in their own original positions in the planar DEM model because the inner and outer plastic rings can effectively confine potash particles to their own locations in a ring test cell. These idealized particles are considered to be the rigid ellipsoids and spheres. That is to say, they do not deform when crystal bridges between potash particles are stretched during rotation in the centrifuge (Refer to Figure 2.2).

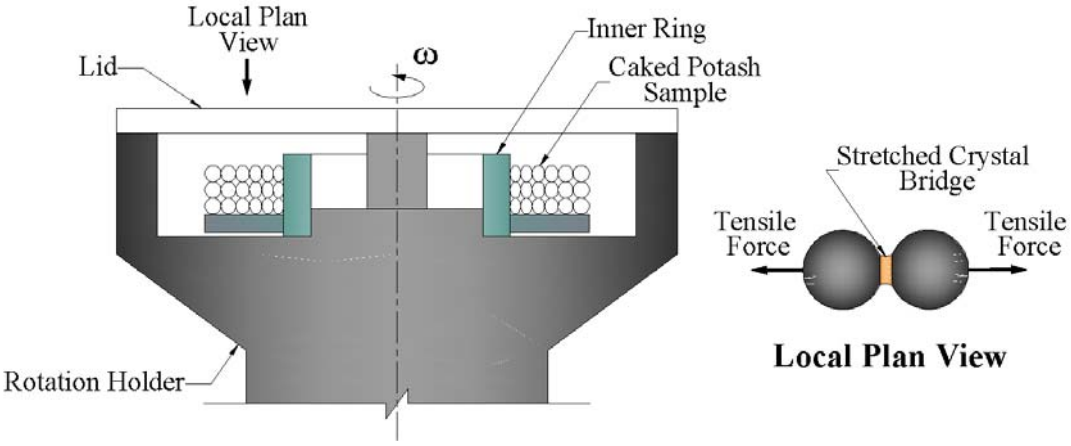

Figure 2.2 Schematic for the cross section of a caked potash specimen rotating in the centrifuge and a crystal bridge in tension

d. Macroscopic deformations of potash ring specimens

During sample preparation, bulk potash particles in a test cell were compressed under a hydrostatic pressure equivalent to a depth in a stored potash pile. Because the structure stiffness of a top clamping plate is high in terms of its special geometry, the deflection of the clamping plate should be neglected during sample preparation. That is, potash particles are uniformly compressed by the external vertical load and have the same elastic-plastic deformation in the direction of external force, as shown in Figure 2.1 (d).

e. Inter–particle forces inside potash specimens

During moisture adsorption, accumulated water mainly concentrated on contact regions between potash particles to dissolve salt and form salt saturated solution. It is thought that projecting parts on a contact region can be dissolved more into the liquid bridge compared with even and concave parts because they are sufficiently exposed to the liquid bridge, as shown in Figure 2.3. The contact regions between wetted potash particles during moisture adsorption become smooth relative to the rough surfaces of dry potash particles. Hence, it is assumed that shear contact forces can be neglected on contact regions during sample preparation. Only normal contact forces exist in each potash specimen during sample preparation.

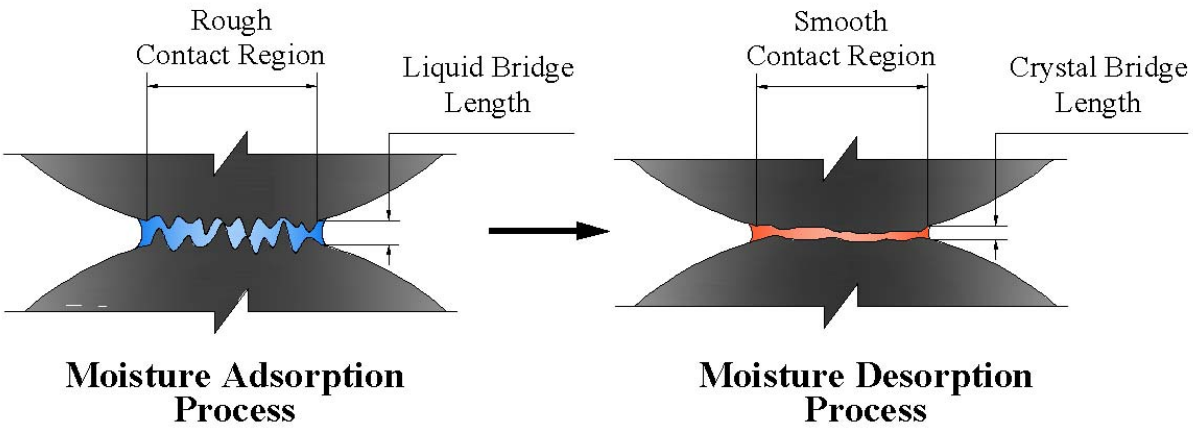

Figure 2.3 Schematic of a liquid/crystal bridge on a contact region

f. Boundary conditions of potash specimens

In terms of Assumption e, the shear contact forces are assumed to be neglected anywhere inside a potash test cell during sample preparation. The inner and outer plastic rings cannot influence the effect of an external load on the compressed elastic-plastic deformation of a specimen during moisture adsorption. Since the height of a specimen was hardly altered by the external load during moisture desorption, the shear contact forces between the specimen and its plastic rings were considered not to occur. It is assumed that the inner and outer plastic rings of a test cell hardly impact the external load acting on a potash specimen during sample preparation.

During fracture test, the radial stress acting on the external edge of a caked specimen was assumed to be zero when the specimen rotated in the centrifuge (Figure 2.2). Wang (2006) pointed out that the number of contact points per unit area on the internal wall and bottom of each test cell was much less than between particles inside the potash sample. It is thought that the mechanical strengths or stresses on the side and bottom interfaces between the potash specimen and the inner plastic ring are much smaller compared with the strength or stresses inside the sample. Wang's experimental data can confirm this conjecture. Hence, the stresses acting on the interior wall and bottom of a potash specimen are assumed to be zero similar to the exterior edge of the specimen.

g. Liquid/crystal bridges at contact regions

It is expected that the moisture content homogeneously distributed in any level throughout a potash specimen. This means that a similar quantity of water concentrated on each contact region in the same level. Each salt component has its own steady concentration in the salt saturated solution situated on contact regions. In the process of moisture adsorption, there are similar saturated brine bridges in a same level composed of potash particles with the analogous sizes.

A similar amount of salt is recrystallized on each contact region in the same level in the same moisture desorption process. This implies that similar crystal bridges are generated on the contact regions in any level of a potash specimen during sample preparation. The crystal bridges on all contact regions in the same potash particle layer are assumed to have similar Young's moduli and bridge lengths after moisture desorption. The cross sectional areas of crystal bridges are mainly determined by the areas of contact regions between compressed potash particles, as shown in Figure 2.3.

h. Physical conditions of caked potash specimens rotating in the centrifuge

After sample preparation, caked potash specimens were rotationally fractured in the centrifuge to obtain data for fracture rotary speed. Figure 2.2 shows that fracture tests of caked potash specimens finished in a closed space. It is assumed that the final porosities of caked potash samples after drying are invariable though crystal bridges inside these samples are slightly stretched during centrifugal rotation. That is, the ambient air conditions cannot affect the cake strengths of potash specimens rotating in the closed part of the centrifuge.

2.2.2 Constitutive laws of planar centrifugal fracture DEM model

Before a caked potash test specimen is fractured in the centrifuge, the specimen behaves like a solid in spite of very small fractions of gas and liquid phases contained in the bed. So, the analysis for the mechanical behaviour of a potash specimen is completed in the frame of solid

mechanics. Microscopic mechanical equilibrium and relative displacement coordination for every idealized potash ellipsoid or sphere are resolved.

2.2.2.1 Mechanical equilibriums

Provided that a potash ring sample rotates at a constant speed, each potash particle is loaded by a centrifugal force, as well as tangential and radial traction forces caused by the surrounding potash particles in contact with the particle. When these forces are tensile, a mechanical balance may be expressed as,

$$F_r^{i-1} + 2\sin\frac{\beta}{2}\cdot F_t^i - F_r^i = F_c^i \tag{2-1}$$

where symbols, F_t^i, F_r^i and F_c^i, respectively denote the tangential tensile force, radial tensile force, and centrifugal force acting on a potash particle in the i^{th} ring. The symbol, β, is the angle corresponding to the potash particle shown in Figure 2.4.

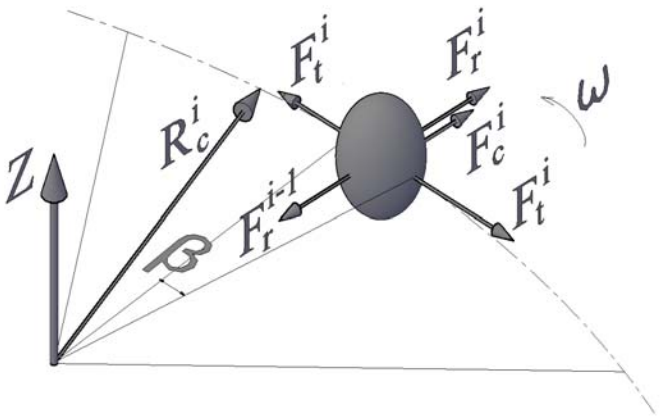

Figure 2.4 Forces acting on an ellipsoidal potash particle

The centrifugal force in the rotating coordinate system, shown in Figure 2.4, F_c^i, may be written as,

$$F_c^i = \frac{1}{6}\pi \cdot \beta \cdot \rho_p \cdot d_p^N \cdot d_p^i \cdot \omega^2 \cdot \left(R_c^i\right)^2 \tag{2-2}$$

where the symbol, ω, is the fracture rotary speed of a caked potash specimen, the symbol, d_p^i, is the short axis diameter of the potash particle in the i^{th} ring, the symbol, d_p^N, expresses the diameter of the potash spherical particle in the N^{th} ring or the long axis diameter for all potash particles. The symbol, R_c^i, is the radius of the i^{th} ring shown in Figure 2.4, and the symbol, ρ_p, denotes the density of idealized potash particles.

2.2.2.2 Translation compatibility of potash particles

Displacements and coordination of idealized potash elements are determined by the regular network of crystal bridges in the DEM model. The Complementary-Energy theorem (Budynas 1999) was used to find relations between displacements of potash particles and complementary strain energies of crystal bridges in order to formulate the geometric compatibility in a potash specimen (Appendix A). The typical formula is as follows,

$$-F_t^i - \frac{A_{ct}^i}{A_{cr}^i}\beta \cdot F_r^i + \frac{A_{ct}^i}{A_{ct}^{i+1}}F_t^{i+1} = 0 \tag{2-3}$$

where the symbols, A_{ct}^i and A_{cr}^i, respectively denote the contact areas of a potash particle in the tangential and radial directions.

2.2.3 Estimations of contact areas

The Hertz contact stress theory (Budynas 1999) is used to estimate the contact areas between particles caused by a known exterior compressive load during sample preparation (Appendix B). When a potash specimen rotates in the centrifuge, these contact areas are assumed not to be altered.

The contact area between potash particles in the direction tangential to potash rings may be expressed as

$$A_{ct}^{i} = \pi \cdot \delta_{cs}^{i} \cdot d_{p}^{N} \tag{2-4}$$

The contact area between potash particles in the radial direction may be written as

$$A_{cr}^{i} = \frac{\pi \cdot d_{p}^{N} (\delta_{cs}^{i} + \delta_{cs}^{i+1})}{(d_{p}^{i} + d_{p}^{i+1})} \sqrt{d_{p}^{i} \cdot d_{p}^{i+1}} \tag{2-5}$$

2.2.4 Boundary conditions

Based on Assumption f in Section 2.2.1 and Figure 2.2, the inner and outer edges and bottom of a potash ring specimen are assumed to be unconfined when the specimen rotates in the centrifuge. With the nonrestraint boundary conditions, the centrifugal fracture test of the potash ring specimen is similar to the uniaxial tension test of brittle media.

2.2.5 Dimensionless representation of tensile forces and stresses

In order to conveniently compare numerical solutions for the mechanical behaviours of potash sample groups with variable particle size ranges, the mechanical quantities, the tensile forces are nondimensionalized. The dimensionless tensile forces are expressed as presented in the following paragraphs.

The dimensionless tangential tensile force corresponding to F_t^i in Figure 2.4 is,

$$\Psi_{t}^{i} = \frac{F_{t}^{i}}{d_{pm} d_{p}^{N} \Theta} \tag{2-6}$$

The dimensionless radial tensile force corresponding to F_r^i in Figure 2.4 is,

$$\Psi_r^i = \frac{F_r^i}{d_{pm} d_p^N \Theta} \tag{2-7}$$

where the symbol, Θ, is defined as the dimensional centrifuge load factor,

$$\Theta = \rho_b \cdot \omega^2 \cdot R_m{}^2 \tag{2-8}$$

where the symbol, ρ_b, is the average density of a caked potash specimen; the symbol, R_m, is the average radius of the caked potash specimen. Its expression is,

$$R_m = \left(R_{bi} + R_{bo}\right)/2 \tag{2-9}$$

where R_{bi} and R_{bo} respectively represent the inner and outer radii of the caked potash specimen.

The dimensionless ring radius is written as,

$$\Gamma_c^i = \frac{R_c^i}{R_m} \tag{2-10}$$

In the DEM model, the dimensionless tensile forces concentrated on contact regions between potash particles can be transformed to the equivalent dimensionless tensile stresses, termed as the local-averaged dimensionless tensile stresses, based on nominal cross sections of particles corresponding to contact regions. The local-averaged tensile stresses can be compared with the microscopic tensile stresses derived from Wang's SC model.

The local-averaged dimensionless tangential tensile stress, corresponding to Ψ_t^i, is expressed as,

$$\Omega_t^i = \frac{F_t^i}{A_p^i \cdot \Theta} \tag{2-11}$$

The local-averaged dimensionless radial tensile stress, corresponding to Ψ_r^i, is expressed as,

$$\Omega_r^i = \frac{F_r^i}{A_p^i \cdot \Theta} \tag{2-12}$$

where the symbol, A_p^i, denotes the nominal cross section area of a potash particle through its center point in the i^{th} ring,

$$A_p^i = d_p^i \cdot d_p^N \tag{2-13}$$

2.2.6 Calculation of cake strength

The cake strength, σ_c, of a potash specimen is determined by the tangential tensile forces between particles,

$$\sigma_c = \frac{\sum_{i=1}^{N} F_t^i}{\sum_{i=1}^{N} A_p^i} \tag{2-14}$$

2.3 Numerical Results and Discussions

Figure 2.5 (a) and (b) respectively show the stair-like distributions of local-averaged dimensionless tangential and radial tensile stresses obtained by the DEM model with three particle size ranges, d_p, and the microscopic dimensionless tangential and radial tensile stress curves derived from Wang's SC model for three values of the Poisson's ratio, υ. The value, 0.3, is the Poisson ratio of pure potash crystal, 0.11 is that of a caked potash cylindrical sample (Wang 2006), and zero is a value for materials in which the strains normal to a compressive or tensile load do not occur.

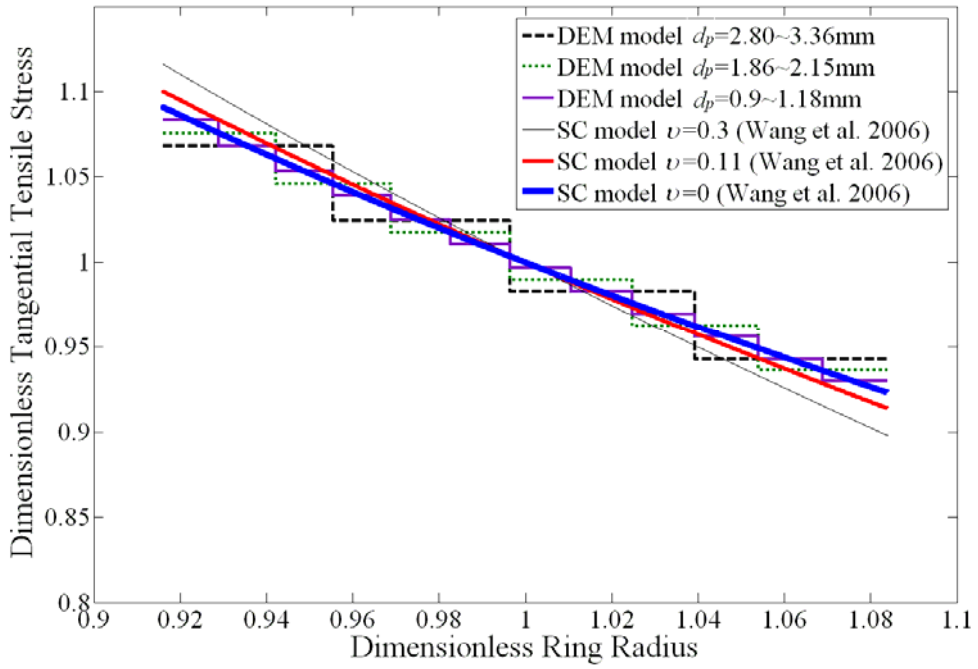

(a)

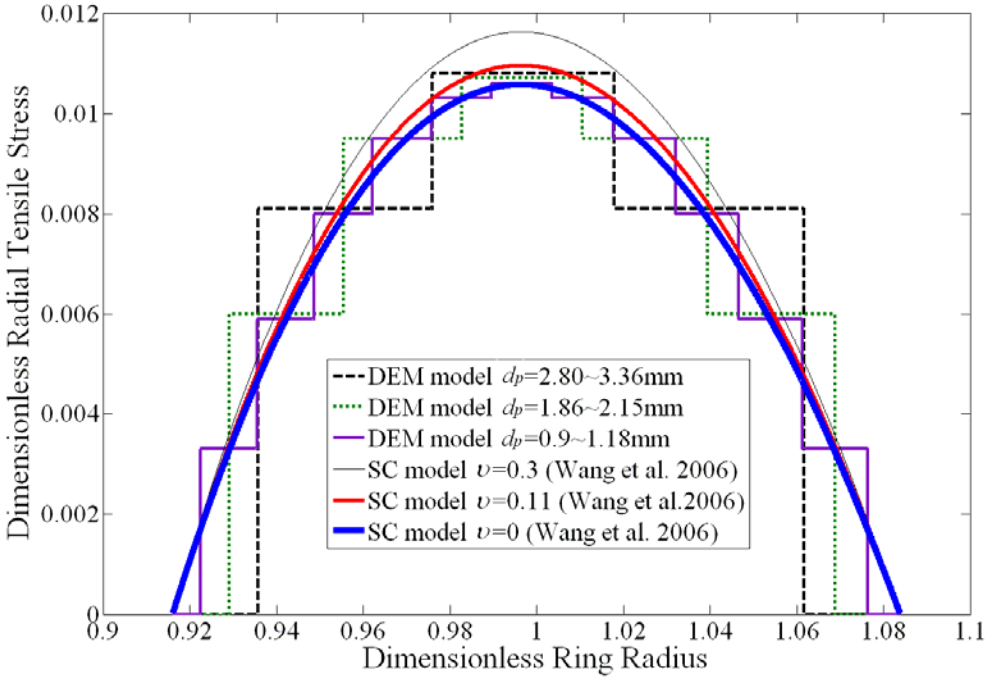

(b)

Figure 2.5 Plots of dimensionless tangential (a) and radial (b) tensile stresses versus dimensionless ring radius

The three groups of stair-like stress distributions of the DEM model are agreeable with the three sets of stress curves of Wang's SC model. Especially for the case with the zero Poisson ratio, the oblique tangential stress curve in Figure 2.5 (a) and the parabola-shaped radial stress profile in Figure 2.5 (b) are nearly parallel to the mean values of stairs in the local-averaged stress distributions. The two numerical models show that the dimensionless tangential stress is much bigger than the dimensionless radial stress, often by a factor of more than 100. It implies that the centrifuge fracture test of a caked potash specimen is equivalent to the uniaxial tension test of a cylindrical potash sample because the radial tensile stresses are trivial.

Figure 2.6 (a) and (b) also show that the dimensionless tangential tensile forces are much bigger than the dimensionless radial tensile forces inside a potash specimen rotating in the centrifuge. The radial tensile forces have the distributions similar to the corresponding radial stresses in Figure 2.5 (b). However, the tangential tensile forces slightly increase in the radial direction of a specimen within a very small range, as shown Figure 2.6 (a). Because the incremental change of the nominal cross section areas (Equation (2-13)) in the radial direction is bigger than the tangential tensile forces situated on the corresponding nominal cross sections, the local-averaged tangential tensile stresses decrease, as shown in Figure 2.5 (a). Relative to the tensile stresses, the fictitious quantities for potash granular media, the tangential tensile forces actually concentrating on contact regions between potash particles are the crucial factor to determine the cake strengths of potash specimens (Equation (2-14)). The tangential tensile forces inside a specimen are almost the same as shown in Figure 2.6 (a), because the relative difference between the maximum and minimum tangential tensile forces is about 0.1%. When a specimen fractures in the centrifuge, the tangential tensile forces acting on crystal bridges between particles almost simultaneously reach the maximum tensile fracture load, which crystal bridges can bear, and fracture interfaces are similar to radial cross sections of the specimen. Pictures about the fracture moment of a caked potash specimen, taken by Wang et al. (2009), can demonstrate the conjecture.

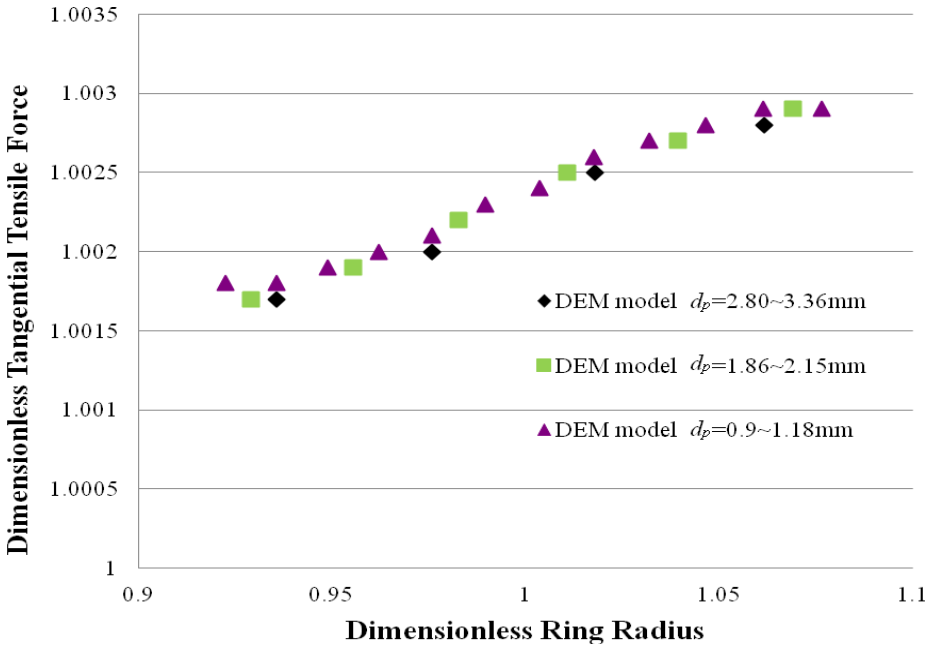

(a)

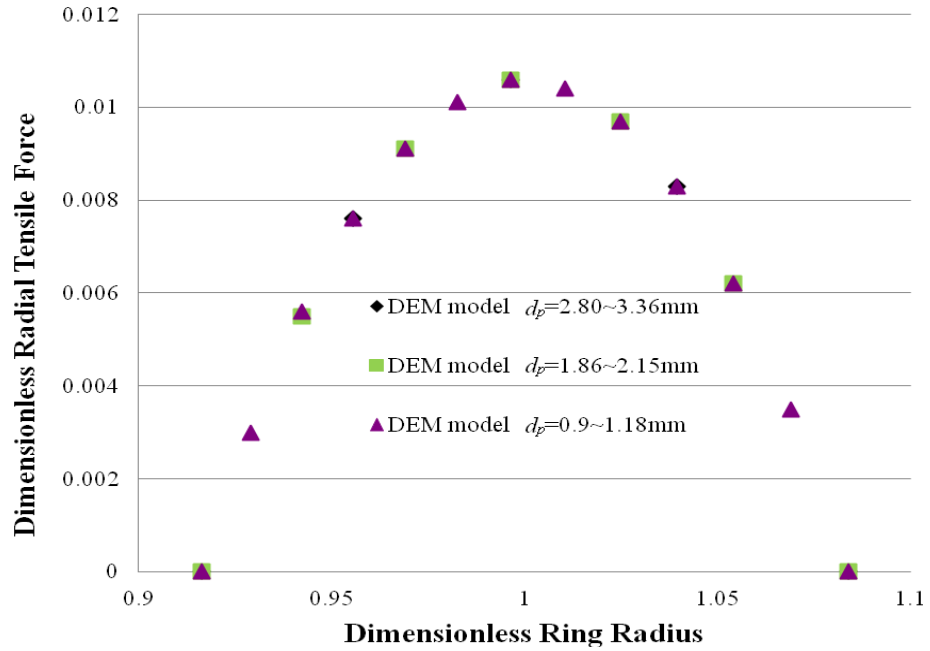

(b)

Figure 2.6 Plots of dimensionless tangential (a) and radial (b) tensile forces versus dimensionless ring radius

Figure 2.5 (a) and (b) show that the microscopic dimensionless stress curves of Wang's SC model deviate from the local-averaged dimensionless stress distributions of the DEM model with the increase of the Poisson's ratio. A caked potash sample is assumed to be a continuum in Wang's SC model. The tangential (t) and radial (r) elastic relations between stress, σ, strain, ε, the Young modulus, E, and the Poisson ratio, υ, may be written as (Budynas, 1999),

$$\sigma_t = \frac{E}{1-\upsilon^2}\left(\varepsilon_t + \upsilon \cdot \varepsilon_r\right) \tag{2-15}$$

$$\sigma_r = \frac{E}{1-\upsilon^2}\left(\varepsilon_r + \upsilon \cdot \varepsilon_t\right) \tag{2-16}$$

From Equation (2-15) and (2-16), it is found that the tensile stresses in the t or r direction are determined by both the strain in the same direction and the strain in the normal direction multiplied by the Poisson ratio. For the case with the zero Poisson's ratio, the stress is just proportional to the strain in the same direction, that is,

$$\sigma_t = E\varepsilon_t \tag{2-17}$$

$$\sigma_r = E\varepsilon_r \tag{2-18}$$

Each idealized potash particle is of concern in the DEM model. The tensile forces and stretched deformations of crystal bridges are used to describe the mechanical behaviour among idealized potash particles. For an idealized potash particle and its accompanying crystal bridges in the i^{th} ring, force-deformation relations in t and r directions can be formulated as,

$$F_t^i = k_t^i \cdot \Delta L_t^i \tag{2-19}$$

$$F_r^i = k_r^i \cdot \Delta L_r^i \tag{2-20}$$

where the symbols, ΔL_t^i and ΔL_r^i, denote the tensile deformations of similar crystal bridges in t and r directions; the corresponding stiffness coefficients of crystal bridges, k_t^i and k_r^i, are

determined by the Young modulus, E^i, the length of, L^i, and the cross section area, A^i, of similar potash crystal bridges. That is,

$$k_t^i = k_r^i = \frac{E^i \cdot A^i}{L^i} \tag{2-21}$$

When Equation (2-21) is substituted into Equation (2-19) and (2-20), the formulas consistent with Equation (2-17) and (2-18) can be obtained to imply that the agreement between the SC and DEM models is best when the Poisson's ratio is zero.

It is observed that the tangential tensile stress curves of the SC model deflect clockwise from the stair-shaped distributions of the DEM model with the increase of the Poisson ratio in Figure 2.5 (a). The tangential tensile strains can keep the entire potash ring sample tensioned and the radial tensile strains are caused by the contractions of specimen cross sections in Figure 2.7. If the trivial growth of the central axis, the chain line in Figure 2.7, is neglected, the exterior and interior edges will move toward the chain line with the nonzero Poisson's ratio. The stretch of the interior edge results in the bigger tangential stress. The contraction of the exterior edge decreases the tangential stress. Hence, the tangential tensile stress curves of Wang's SC model with nonzero Poisson's ratios have bigger gradients than the stair-like tangential tensile stress distributions of the DEM model.

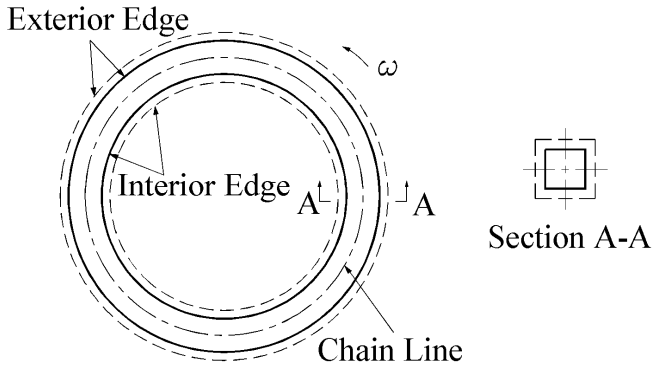

Figure 2.7 Deformation of a potash SC model on rotation

2.4 Conclusions

Agreeable stress predictions between the DEM and SC models signify that the DEM is an effective numerical method for quasi-static granular media. If potash specimens are thought of as elastic continua, tangential tensile stress profiles of the SC model have higher gradients than the DEM model, when the Poisson's ratio is bigger than zero. Dimensionless tensile force distributions derived from the DEM model show that the tangential tensile force, much bigger than the radial tensile force, is the dominant factor to fracture a potash ring specimen. Fracture interfaces are nearly the same as radial cross sections of a caked potash specimen since tangential tensile forces on a radial cross section almost simultaneously increase to the maximum fracture load which crystal bridges can bear.

CHAPTER 3

MEASUREMENTS OF CAKING PROPERTIES AND FRACTURE TESTS FOR COMPRESSED POTASH SPECIMENS

3.1 Introduction

3.1.1 Background of potash caking experiments

Research on cake strength measurements of granular media (Tanaka 1978, Leaper et al. 2003, Wang et al. 2009) has shown that the cake strength of a granular sample is correlated with the macroscopic properties of the sample such as porosity, moisture content, and average particle size. Because the macroscopic properties of bulk potash can be used to characterize the caking process of bulk potash and estimate the cake strength of potash lumps, they are termed as the caking properties of bulk potash. Some caking properties of potash samples such as mass, height, and average particle size are directly measured. Two properties, porosity and moisture content, are calculated by using these measured properties.

Dry sample porosity, ε, is the volume fraction of gas phase in a potash specimen. That is,

$$\varepsilon = 1 - \frac{\rho_b}{\rho_s} \tag{3-1}$$

where the symbol, ρ_b, denotes the density of a potash specimen and the symbol, ρ_s, is the density of potash crystal.

Sample moisture content, X, is defined as,

$$X = \frac{m_l}{m_i} \tag{3-2}$$

where the symbol, m_l, denotes the mass of water accumulated by a dry potash specimen, the symbol, m_i, is the initial mass of the dry potash specimen, and m_l equals the difference between m_i and m_w or m_d as shown in Table 3.2.

3.1.2 Purposes of experiment studies in this chapter

Literature of heat and mass transfer and salt recrystalization in bulk potash (Peng et al. 2000, Sun et al. 2006, and Wang et al. 2008) reveals that the relative humidity variation of the ambient air around a potash pile is the main cause of bulk potash caking. On the other hand, it is found that the potash lumps in a huge potash pile have higher cake strengths. That is to say, variations of potash cake strength within a potash pile imply that the macroscopic properties are altered by the depth of the potash pile. Hence, the experimental research presented in this chapter focuses on the effects of potash pile depth and ambient air relative humidity on the caking properties and cake strength of bulk potash.

A sample preparation process was needed for the experimental research. Wang et al. (2006) presented their process to prepare caked potash ring specimens in the uncompressed state. In their process, dry potash samples without compression directly obtained their moisture by the addition of known quantities of water to dry potash particles. In a huge potash pile, most particles in the compressed state actually adsorb and desorb moisture through the ambient air during long storage periods (i.e. from a few weeks to many months). For this experimental research, the method of Wang et al. was first applied to make dry potash ring specimens. The specimens were loaded with the external compressive forces equivalent to depths of a potash pile and placed in humidity-controlled chambers to adsorb and desorb moisture. Once the specimens were caked, their fracture rotary speeds were tested in the centrifuge.

The whole experimental procedure included the two parts: sample preparation and fracture testing. The objectives in this experimental part were as follows,

a) To apply the sample preparation process to make caked potash specimens with the multiple variations of external compressive load and ambient air humidity and measure the altered caking properties of potash specimens including mass, height, porosity, and moisture content during sample preparation;

b) To test the fracture rotary speeds of caked potash specimens and compute their cake strength; and

c) To analyze the impacts of external compressive load and environmental humidity on the caking properties and cake strength of bulk potash.

3.2 Experimental Procedure

3.2.1 Potash sample preparation

The potash sample preparation constituted the following four functional parts: bulk potash sieving, dry potash particle filling, external loading, and sample moisture adsorption/desorption storage. When the sample moisture content reached the expected values shown in Table 3.1, moisture adsorption and desorption processes were considered to be completed. With the moisture adsorption and desorption, the sample preparation process was separated into three stages: initial state, post adsorption and post desorption. The caking properties were also classified by the three stages of sample preparation. These caking properties and their individual symbols in every stage are shown in Table 3.2.

Table 3.1 Saturated salt solutions, relative humidity, and expected values of moisture content, which dry potash specimens can acquire during moisture adsorption and desorption

	Moisture Adsorption Process			Moisture Desorption Process	
Saturated Salt Solution	KI	NaCl	KCl	$Mg(NO_3)_2$	LiCl
Relative Humidity (RH)	69%	75%	84%	52%	11%
Expected values of Sample Moisture Content (MC)	0.8%	1%	3%	The mass of each specimen cannot change any more.	

Table 3.2 Caking properties and their symbols in all experimental stages

	Initial State	Adsorption Process	Desorption Process
Mass (kg)	initial dry sample mass m_i	post-adsorption wetted sample mass m_w	post-desorption dried sample mass m_d
Height (mm)	initial free sample height h_{if} initial compressed sample height h_{ic}	post-adsorption compressed sample height h_{ca}	post-desorption compressed sample height h_{cd}
Porosity	initial free sample porosity ε_{if} initial compressed sample porosity ε_{ic}	post-adsorption compressed sample porosity ε_{ca}	post-desorption compressed sample porosity ε_{cd}
Moisture Content		post-adsorption maximum sample moisture content X_i	post-desorption residual sample moisture content X_r

The four functional parts in order of sample preparation are elaborated as follows:

a. Selection of potash particles

Potash fertilizer is composed of the mixture of granules with a wide range of particle sizes from 0.5 mm to 5 mm shown in Figure 3.1(a). The rotary sieving machine and the set of sieve trays in Figure 3.1(b) were used to obtain potash particles with the small size range from 0.9 mm to 1.18 mm. These selected potash granules were heated and dried in an oven at the temperature of 70^{o}C for 24 hours prior to cooling for 2 hours in sealed plastic bags. The processed potash particles, like those in Figure 3.1(c), were used for the preparation of potash ring specimens.

(a) (b) (c)

Figure 3.1 Selection of potash particles: (a) a pail of unprocessed potash granules, (b) the set of sieve trays mounted in the shaker machine, (c) sieved and dried potash particles

b. Preparation of dry potash ring samples

As shown in Figure 3.2 (a) and (b), a pair of internal and external plastic rings was clamped by a metal strap to form a cylindrical ring space, the inner and outer radii of which were 65.5 mm and 77.5 mm. Dried potash granules were packed into each of these cells, as shown in Figure 3.2 (c). About 30 potash ring specimens were prepared as a group at one time for a fixed external compressive load. For new groups, internal and external plastic rings were mixed and then randomly paired for each new specimen.

(a) (b) (c)

Figure 3.2 Making of a dry potash ring specimen: (a) a pair of internal and external plastic rings and a clamping strap, (b) a ring container generated by the set of plastic rings and the strap, (c) a dry potash ring specimen

c. Applications of exterior equivalent loads

Since bulk potash granules are usually stored in huge piles, e.g. 3 to 15 metres high, the three nominal depths in a potash pile shown in Table 3.3 were used to determine the three corresponding compressive forces, which were respectively loaded on the three groups of potash specimens, each of which had about 30 potash samples. The nominal pile depths can be simulated by applying the compressed springs on the top surfaces of the potash ring samples. The spring deformations in Table 3.3 were converted into the external loads equivalent to the nominal pile depths with the spring force-deformation relation calibrated after experiments, as shown in Appendix C.

Table 3.3 External equivalent loads and spring deformations corresponding to nominal sample depths in potash pile

Nominal sample depth in potash pile (*m*)	0	4	8	16
Converted external load equivalent to nominal pile depth (*m*)	0	3.9±0.41	7.8±0.41	15.9±0.42
Applied spring deformation (*mm*)	0	7.2±0.035	14.4±0.032	29.4±0.14

As shown in Figure 3.3 (a), (b), (d), and (e), a ring screen and a pair of clamping plates separately were placed on and under a potash specimen for the uniform compression to the specimen. A compressive force was generated and loaded on the specimen while a calibrated spring was centrally located on the specimen and compressed by using a nut, bolt, and washer (Refer to Figure 3.3 (c) and (f)). The loading process was repeated for a group of about 30 potash specimens. Corresponding to the three nonzero external loads listed in Table 3.3, the three groups of specimens, over 90 samples in total, were prepared. The each sample group was subdivided into three sub-groups for the following sample storage stage. The two subgroups of extra specimens for the zero external loads were prepared for the comparative analysis with the samples of Wang et al. (2006). The sample caking properties in the initial state (Table 3.2) were measured by using the calibrated balance and callipers (Appendix C) at this stage.

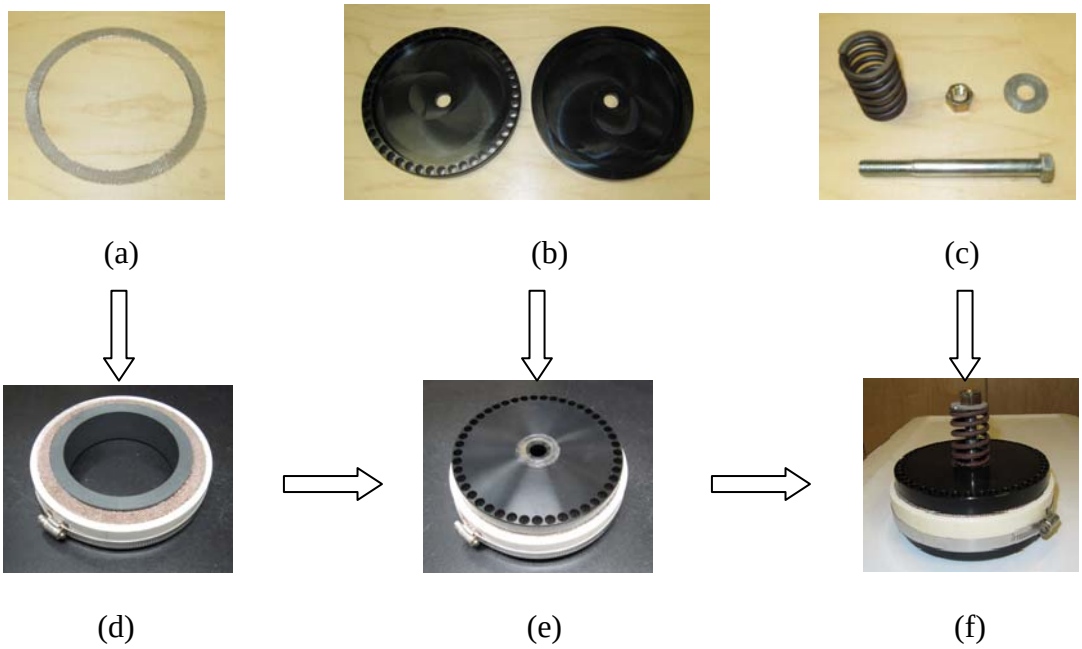

Figure 3.3 Externally loading on a potash specimen: (a) a ring screen, (b) a pair of top and bottom clamping plates, (c) a set of calibrated spring, bolt, nut, and washer, (d) a ring potash granular specimen covered by a ring screen, (e) the specimen stacked up by the top clamping plate with circular holes for moisture adsorption and desorption and the bottom clamping plate, (f) a compressed specimen ready for exposure to ambient air humidity in a sample conditioning chamber

d. Storage of potash samples

Each sub-group of potash specimens was placed in a sealed chamber (Figure 3.4) at a fixed relative humidity within which the water vapour was adsorbed by the test specimens. The constant relative humidity in each closed sample preparation chamber was maintained by a certain type of saturated salt solution (ASTM Std. E104-02 and Rockland 1960), as shown in Table 3.1. At the room temperature, the three types of saturated brine (potassium iodide (KI), sodium chloride (NaCl), and potassium chloride (KCl)) were used for the moisture adsorption processes of the potash specimens. When the maximum average moisture content, X_i, of a sub-group of samples reached the expected value listed in Table 3.1, the process of water vapour adsorption was cut off. Subsequently, these samples were transferred to another chamber with a low relative humidity and dried until the mass of them did not change. The saturated brines of

magnesium nitrate ($Mg(NO_3)_2$) and lithium chloride (LiCl) were used to generate the dry ambient air in the chambers (Refer to Table 3.1). The caking properties of the potash specimens during moisture adsorption and desorption (See Table 3.2) were measured and calculated at this stage.

(a) (b)

Figure 3.4 Potash sample storage: (a) sealed chambers maintained at a fixed relative humidity, (b) compressed potash specimens inside a chamber

3.2.2 Fracture test

The centrifuge and tachometer (Figure 3.5 (a)) were used to rupture caked potash samples and acquire the fracture rotary speed data. The testing process was divided into the following steps.

a. Judgment of caking completion

During moisture desorption, it was shown by weighing test cells that the mass of potash samples did not change, as mentioned in Table 3.1. In other words, the potash specimens were considered to be dried and caked without any more mass reduction. Hence, the moisture desorption stage ended.

b. Disassembly of sample-making cell

After drying, the cells (refer to Figure 3.3 (f)) were taken apart to obtain caked potash ring specimens with internal plastic rings, as shown in Figure 3.5 (b).

(a)

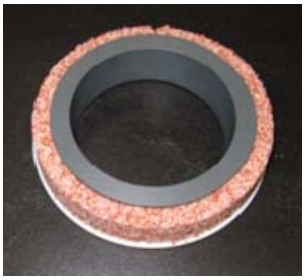

(b)

(c)

(d)

(e)

Figure 3.5 Potash sample fracture test: (a) the centrifuge and tachometer with an optical sensor mounted at the edge, (b) a caked potash ring specimen, (c) sample installation in the tray, (d) a transparent cover fixed on the tray, (e) sample rotation fracture in the centrifuge

c. Installation of potash sample

As shown in Figure 3.5 (c), a caked potash ring sample was placed in the circular tray. A transparent cover (Figure 3.5 (d)) was used to form a closed space, which could prevent potash particles from splashing from the circular tray. The optical part of the tachometer was adjusted to aim at the reflective band on the transparent cover.

d. Rupture of potash sample

After the sample installation and tachometer adjustment, the centrifuge was switched on to break the potash sample. In the beginning, the power knob was turned towards the one-fourth of the full scale to rotationally accelerate the sample. When the sample rotary speed was not increased, the power knob was turned up to make the sample accelerated at a small spin acceleration until sample fracture (Figure 3.5 (e)). For example, the rotary speed indicated by the

tachometer constantly increased at the rate of 2 rpm. Hence, it was considered that the sample was rotated and fractured at the quasi-steady state with the small spin acceleration. When the fracture occurred, the reading of the tachometer was the fracture rotary speed of the sample, ω. After the fracture testing, a vacuum was used to clean up the centrifuge. The testing process was repeated for a sub-group of about ten samples to obtain the data of fracture rotary speed, which were input into the planar DEM model to compute the cake strength of the sample sub-group with a pre-determined external load and moisture adsorption humidity.

After a group of about 30 potash specimens were fractured in the centrifuge for an external load and the three levels of moisture adsorption humidity, all of about 30 sets of internal and external plastic rings were cleaned and mixed. These internal and external rings were paired randomly to prepare a new group of potash samples. The sample preparation and fracture test were then repeated for the other external loads.

3.3 Experimental Data and Analyses

In the long sample preparation and data measurement processes, instruments, such as weight balance, callipers, tachometer, and springs, are frequently used to bring about bias and random errors. Uncertainty analysis (ASME PTC 19.1 2005) was used to estimate the effects of these errors. The calibration data for the measurement instruments are presented in Appendix C. The analysis showed that compared with large random errors, bias errors caused by these instruments may be neglected. The measurement uncertainty was mainly dependent on the random errors derived from caking properties' measurements and fracture tests of potash specimens, as shown in Appendix C.

3.3.1 Sample preparation and measurements of caking properties

As mentioned in Parts c and d of Subsection 3.2.1, the nine sub-groups of potash specimens were prepared for the three nominal pile depths and three levels of moisture adsorption humidity. In addition, the two sub-groups of specimens without compression, termed as Case 0* and Case 0**, were prepared for the mass transfer study and the comparison with the experimental data of Wang et al. (2006). The moisture adsorption/desorption periods for the

eleven sub-groups of potash specimens are shown in Table 3.4. The explanations of terms (Case 0* and Case 0**) and the uses of saturated salt solutions for moisture desorption are provided in the notes below Table 3.4.

Table 3.4 Eleven test sub-groups showing moisture adsorption/desorption periods in days for different levels of nominal sample depth and moisture adsorption humidity

		Moisture Adsorption Humidity ϕ_A		
		69%	75%	84%
Nominal sample depth (m)	0*		14/10¤	
	0**		123/23	
	4	93/38	37/73	14/73
	8	18/52	28/49	28/77
	16	18/10¤	18/10¤	15/10¤

* Top surfaces of specimens were completely exposed to the ambient air in a chamber (i.e. no top clamping plate), as shown in Figure 3.2 (c).
** Top plates with circular holes were located on potash samples. These top plates can reduce the exposure areas of samples to the ambient air, as shown in Figure 3.3(e).
¤ The saturated brine of magnesium chloride ($Mg(NO_3)_2$) was used for moisture desorption. Other sub-groups without the superscript (¤) used the saturated brine of lithium chloride (LiCl) for drying.

3.3.1.1 Sample mass

Moisture adsorption and desorption caused the mass of potash specimens to change during sample preparation. Sample mass data at different experimental stages are shown in Table 3.5. When the three groups of specimens were prepared for the three levels of external load in Part c of Subsection 3.2.1, mass data for dry potash specimens were influenced by the random errors of measurements and the size biases of plastic rings. Given that the size biases were neglected, the three groups of independent specimens should conform to the three similar normal distributions of mass data. Actually, the statistical cumulative probability distributions of the three datasets were similar especially for the interval from 1% to 90% as shown in Figure D-1 of

Appendix D. Figure D-1 and Table 3.5 indicate that the three sample mass datasets had analogous mean values of initial sample mass. This means that the size biases of the plastic rings were insignificant and negligible in the following uncertainty analysis. It is further deducible that the three groups of specimens prepared using the same experimental procedure should come from a common assembly of independent samples. Figure D-2 of Appendix D showed that the three mass datasets satisfies a common normal probability distribution. The consistency convinces the conjecture that all of about 90 specimens belonged to a common sample assembly with the mean value of initial sample mass, 176.5±1.1 g. Data for m_w and m_d were obviously influenced by the relative humidity values for moisture adsorption and desorption listed in Table 3.1. The data for sample mass at the different stages of sample preparation were used to calculate the moisture contents of potash specimens.

Table 3.5 Data on initial sample mass, m_i, post-absorption sample mass, m_w, and post-desorption sample mass, m_d

			Moisture Adsorption Relative Humidity ϕ_A			Mean Value
			69%	75%	84%	
Nominal sample depth (m)	4	m_i (g)	177.8±1.2	173.0±2.3	178.0±2.8	176.7±2.1
		m_w (g)	178.6±1.2	174.9±2.4	183.0±2.7	
		m_d (g)	177.9±1.2	173.0±2.3	177.9±2.8	
	8	m_i (g)	180.1±4.6	172.5±2.5	178.9±2.0	176.6±2.4
		m_w (g)	181.6±4.5	174.4±2.6	180.3±4.3	
		m_d (g)	180.2±4.6	172.7±2.6	177.9±4.4	
	16	m_i (g)	180.3±6.5	171.9±1.5	178.4±2.9	176.4±1.4
		m_w (g)	181.7±4.1	173.7±1.5	183.9±4.0	
		m_d (g)	180.6±4.1	172.2±1.5	180.0±3.7	

3.3.1.2 Sample height

Sample height data for two groups of compressed potash specimens are shown in Table 3.6. It was found that these potash samples had a consistent mean value of the initial free sample height, h_{if}, which was equal to 28.9±0.1 mm at the confidence interval of 95%.

Data on post-adsorption and post-desorption compressed sample heights (h_{ca} and h_{cd}) in Table 3.6 show that the compressed heights of potash specimens hardly changed during moisture desorption. The two average compressed sample heights (h_{ca} and h_{cd}) of each sub-group were therefore considered to be equivalent to each other. The statistical analysis in Table D-1 of Appendix D shows that the external equivalent load, relative to the environmental humidity, had a stronger impact on the post-desorption compressed sample height (h_{cd}). Figure 3.6 illustrates that a higher external equivalent load caused larger compressed deformations of potash specimens.

Table 3.6 Data on initial free height (h_{if}), the initial compressed height (h_{ic}), the post-absorption compressed height (h_{ca}), the post-desorption compressed height (h_{cd})

			Moisture Adsorption Relative Humidity ϕ_A			Mean Value
			69%	75%	84%	
Nominal sample depth (m)	4	h_{if} (mm)	29.1±0.1	28.4±0.2	29.3±0.4	28.9±0.2
		h_{ic} (mm)	28.7±0.1	28.0±0.2	28.8±0.4	28.5±0.2
		h_{ca} (mm)	27.8±0.1	27.0±0.2	27.7±0.4	
		h_{cd} (mm)	27.8±0.1	27.0±0.2	27.8±0.4	
	8	h_{if} (mm)	28.8±0.2	28.8±0.2	29.1±0.2	28.9±0.1
		h_{ic} (mm)	28.4±0.1	28.3±0.2	28.4±0.1	28.4±0.1
		h_{ca} (mm)	27.0±0.2	27.0±0.2	26.9±0.2	
		h_{cd} (mm)	26.9±0.2	27.0±0.2	26.9±0.4	

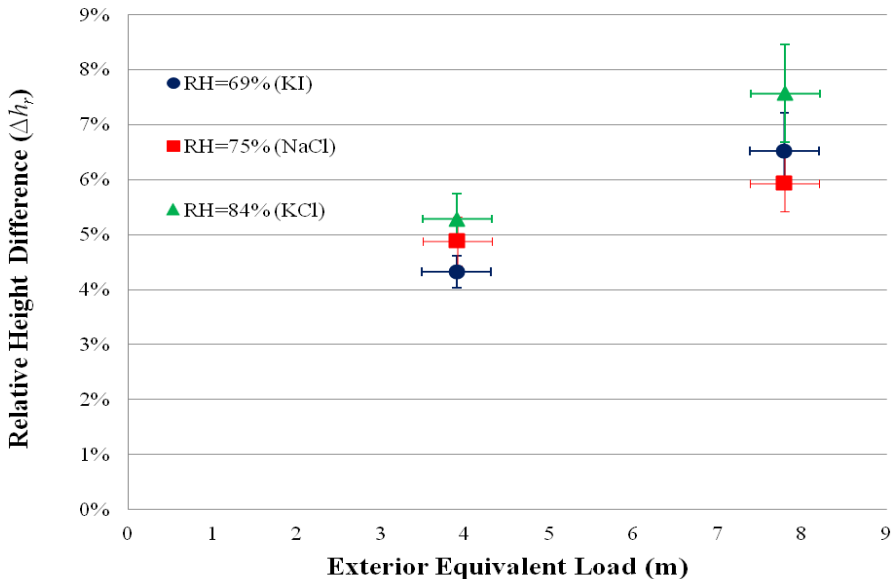

Figure 3.6 Relative difference between initial free and post-desorption compressed heights of specimens (Δh_r = (h_{if} - h_{cd})/ h_{if}) versus external equivalent load

3.3.1.3 Sample porosity

Because the sub-groups of potash samples had similar mean values of m_i and h_{if}, as shown in Table 3.5 and 3.6, these sub-groups had a common average of the initial free sample porosity (ε_{if}) equal to 0.430±0.004. Table 3.7 shows that the mean values of initial free, initial compressed, post-adsorption, and post-desorption sample porosities (ε_{if}, ε_{ic}, ε_{ca}, and ε_{cd}) for sample sub-groups with the nominal sample depths of 4 and 8 m. It was found that the mean value of ε_{ca} for each sample sub-group was smaller than its mean value of ε_{cd} because sufficient quantities of condensed water inside potash specimens were evaporated to leave the non-negligible gaseous space during moisture desorption. The statistical analysis in Table D-2 indicates that the post-desorption sample porosity, ε_{cd}, was altered mainly by the external equivalent load. Figure 3.7 illustrates that a higher external load resulted in a bigger variation of the sample porosity.

Table 3.7 Data about initial free porosity, ε_{if}, the initial compressed porosity, ε_{ic}, the post-absorption compressed porosity, ε_{ca}, and the post-desorption compressed porosity, ε_{cd}

			Moisture Adsorption Relative Humidity ϕ_A			Mean Values
			69%	75%	84%	
Nominal sample depth (m)	4	ε_{if}	0.429±0.004	0.432±0.007	0.432±0.006	0.431±0.003
		ε_{ic}	0.421±0.003	0.424±0.007	0.424±0.006	0.423±0.003
		ε_{ca}	0.398±0.004	0.390±0.008	0.366±0.006	
		ε_{cd}	0.402±0.003	0.403±0.007	0.403±0.007	
	8	ε_{if}	0.416±0.016	0.440±0.007	0.431±0.014	0.429±0.008
		ε_{ic}	0.407±0.016	0.430±0.007	0.419±0.014	0.419±0.007
		ε_{ca}	0.365±0.019	0.390±0.009	0.362±0.015	
		ε_{cd}	0.375±0.020	0.403±0.008	0.379±0.017	

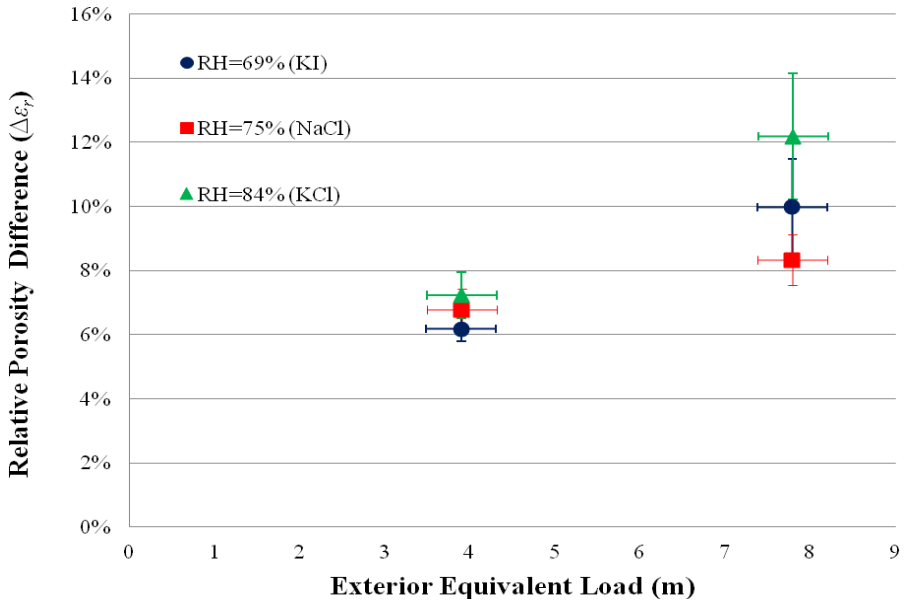

Figure 3.7 Relative difference of initial free and post desorption compressed porosities of specimens ($\Delta\varepsilon_r = (\varepsilon_{if} - \varepsilon_{cd})/\varepsilon_{if}$) versus external equivalent load

3.3.1.4 Sample moisture content

The sample moisture content, calculated by using Equation (3-2), can macroscopically quantify the water vapour condensation and water evaporation of a whole potash specimen during moisture adsorption and desorption. The mean values of maximum and residual sample moisture contents (X_i & X_r) for eleven sub-groups are given in Table 3.8. The mean value of X_i for each sample sub-group tended to be consistent with the expected value of sample moisture content listed in Table 3.1. The comparison between Case 0* and 0** in Table 3.8 indicates that a lower moisture desorption humidity can result in a smaller residual sample moisture content (X_r). It is expected that the maximum and residual sample moisture contents were mainly determined by the ambient air humidity in chambers.

Table 3.8 Maximum and residual sample moisture content (X_i & X_r)

			Moisture Adsorption Relative Humidity ϕ_A		
			69%	75%	84%
Nominal sample depth (m)	0*	X_i		(1.01±0.16)%	
		X_r¤		(0.21±0.01)%	
	0**	X_i		(1.07±0.09)%	
		X_r		(0.11±0.04)%	
	4	X_i	(0.46±0.03)%	(1.08±0.13)%	(2.80±0.23)%
		X_r	(0.06±0.01)%	(-0.02±0.03)%	(-0.07±0.08)%
	8	X_i	(0.83±0.08)%	(1.10±0.10)%	(1.75±0.23)%
		X_r	(0.01±0.03)%	(0.10±0.02)%	(0.40±0.21)%
	16	X_i	(0.79±0.09)%	(1.06±0.09)%	(3.08±0.41)%
		X_r¤	(0.18±0.01)%	(0.16±0.02)%	(0.93±0.10)%

Symbols (*, **, and ¤) denote the same notes as Table 3.4.

Figure 3.8 shows the variations in dimensionless sample moisture content for the five sample sub-groups and the corresponding theoretical curve during moisture adsorption. The theoretical curve of dimensionless moisture content and time (X_o & t_o) is expressed as

$$X_o = 1 - e^{-t_o} \tag{3-3}$$

During moisture adsorption, the dimensionless quantities (X_o & t_o) are determined by the following equations.

$$X_o = \frac{X}{X_e} \tag{3-4}$$

$$t_o = \frac{t}{t_a} \tag{3-5}$$

where X_e is the equilibrium moisture content determined by Equation (4-21) with the relative humidity of 75%; the symbol, t, is the storage time and the symbol, t_a, denotes the moisture adsorption time constant, which is defined as the time required to achieve 63% of the maximum possible moisture content change after a step change in the relative humidity.

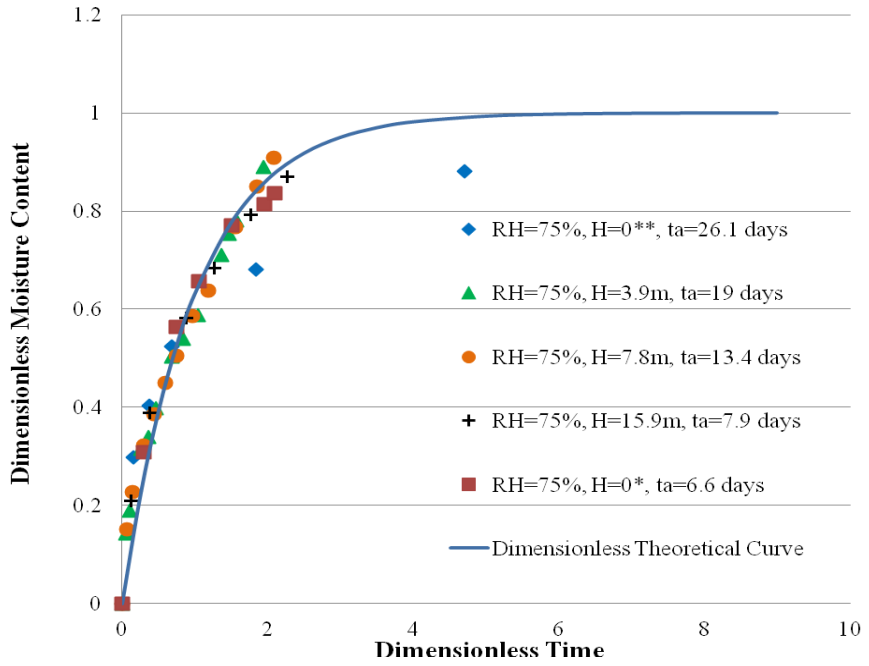

Figure 3.8 Variations of dimensionless sample moisture content with dimensionless time during moisture adsorption

The five sub-groups of potash samples accomplished their moisture adsorption with the same relative humidity (75%) and their own external equivalent loads (0*, 0**, (3.9±0.41), (7.8±0.41), & (15.9±0.42) metres). It is found that most of the data agree with the corresponding theoretical curve. As shown in Figure 3.8, the time constant (t_a) increased as the external equivalent load diminished. However, for Case 0* without the external equivalent load and top clamping plates, potash specimens consumed the shortest time for moisture adsorption because the whole top surfaces of potash specimens were exposed to the high humid air in the storage chamber and this expedited the moisture adsorption process.

Figure 3.9 shows the dimensionless sample moisture content data for the five sample sub-groups in their subsequent moisture desorption processes, as well as the corresponding theoretical curve. Similar to Equation (3-3), the theoretical curve for moisture desorption is expressed as

$$X_o = e^{-t_o} \tag{3-6}$$

$$t_o = \frac{t}{t_d} \tag{3-7}$$

where symbol, t_d, is moisture desorption (drying) time constant, which is defined as the time taken for the moisture content to reduce 63% of the maximum possible value after a step change in the relative humidity.

It is shown that the data are in agreement with the corresponding theoretical curve in the early moisture desorption stage and are above the theoretical curve at the final stage. This observation implies that some water is sealed inside potash specimens by recrystallized salt bridges. For most of the five cases, a lower moisture desorption humidity caused a faster moisture desorption process and shorter drying time constant (t_d).

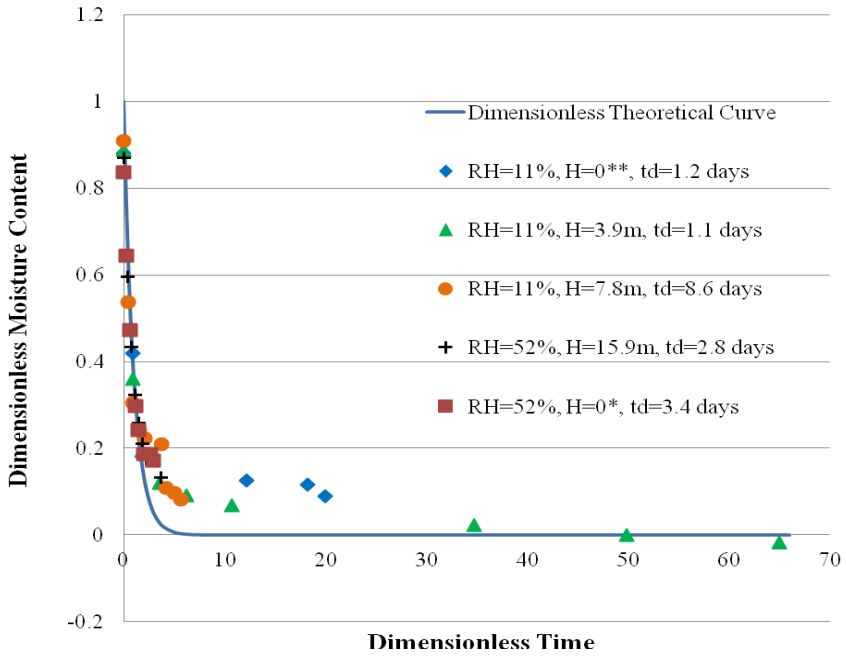

Figure 3.9 Variations of dimensionless sample moisture content with dimensionless time during moisture desorption

By comparing Figure 3.9 with 3.8, it is found that the moisture absorption time constant (t_a) of each sample sub-group is bigger than its moisture desorption time constants (t_d). In other words, the moisture desorption processes of potash specimens in the steady state storage consumed less time relative to their moisture adsorption processes.

In Figure 3.9, the sample sub-group with an external equivalent load of (3.9±0.41) metres had negative mean values of sample moisture content, below its theoretical curve; this is because the set of potash specimens, which were prepared in summer, adsorbed extra water from the ambient air before their moisture adsorption storage. The occurrence of negative sample moisture content implies that some uncontrollable factors outside humidity-controlled chambers caused significant measurement deviations of the sample moisture content. A new process quantity, ΔX, the difference between X_i and X_r shown in Table 3.9, was used to investigate the effects of external load and environmental humidity on the moisture adsorption and desorption inside potash specimens, since the moisture content difference can reduce or offset impacts from those uncontrollable factors. Figure 3.10 shows that higher moisture adsorption humidity and lower desorption humidity can generate bigger sample moisture content differences (ΔX). Data

points shown in the figure imply that the external equivalent load seemingly has no effective influence on the sample moisture content difference. For example, the squares, which denote the sample moisture content differences of the sample sub-groups with the same moisture adsorption humidity (75%) and four external equivalent loads, lie at similar levels within their own measurement uncertainties, as shown in Figure 3.10.

Table 3.9 Data of the difference (ΔX) between X_i and X_r

		Sample Preparation Adsorption Relative Humidity ϕ_A		
		69%	75%	84%
Nominal sample depth (m)	0*		(0.81±0.16)%	
	0**		(0.96±0.08)%	
	4	(0.40±0.02)%	(1.10±0.13)%	(2.86±0.24)%
	8	(0.83±0.07)%	(1.00±0.10)%	(1.37±0.21)%
	16	(0.61±0.08)%	(0.90±0.09)%	(2.15±0.45)%

* and ** denote the same notes as Table 3.4.

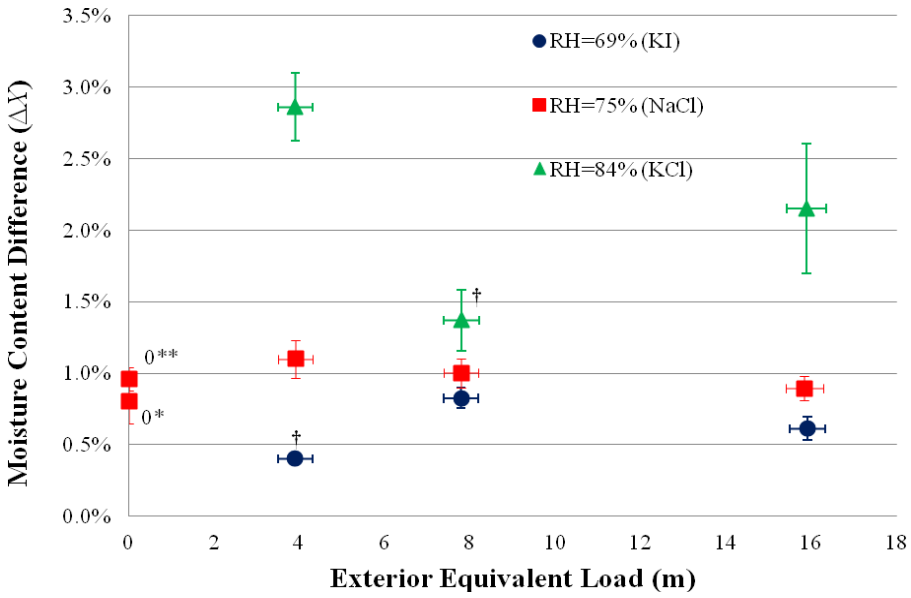

Figure 3.10 Sample moisture content difference (ΔX) versus external equivalent load with variations of ambient air humidity (data points noted by symbol, †, correspond to the sample subgroups, X_i values (as shown Table 3.8) of which are less than expected values of MC in Table 3.1)

3.3.2 Fracture tests of caked potash specimens

Data for the mean values of the fracture rotary speed and cake strength for eleven sample sub-groups are shown in Table 3.10. A comparison of data between Figure 3.10 and 3.11, except for the cases with the moisture adsorption humidity of 84%, shows that the trends for cake strength are inconsistent with the distributions of moisture content difference. The external load enhanced the cake strength of potash specimens. Data points for Case 0* and 0** in Figure 3.11 imply that a lower moisture desorption humidity can also generate stronger caked potash specimens, though it results in a faster drying process. The fact appears contradictory to the conclusion of Wang et al. 2009.

Table 3.10 Fracture rotary speed (ω) and average cake strength (σ_c) with the varied external loads and environmental humidity

			Moisture Adsorption Relative Humidity ϕ_A		
			69%	75%	84%
Nominal sample depth (m)	0*	ω (rpm)		451±109	
		σ_c (kPa)		13.2±6.4	
	0**	ω (rpm)		794±335	
		σ_c (kPa)		44.3±37.4	
	4	ω (rpm)	1120±125	1517±294	2218±171
		σ_c (kPa)	86.5±19.4	$(1.54\pm0.60)\times10^2$	$(3.39\pm0.53)\times10^2$
	8	ω (rpm)	1556±365	1691±175	1455±191
		σ_c (kPa)	$(1.69\pm0.80)\times10^2$	$(1.91\pm0.40)\times10^2$	$(1.46\pm0.36)\times10^2$
	16	ω (rpm)	1811±173	2025±161	1630±441
		σ_c (kPa)	$(2.30\pm0.44)\times10^2$	$(2.73\pm0.44)\times10^2$	$(1.85\pm1.00)\times10^2$

* and ** denote the same notes as Table 3.4.

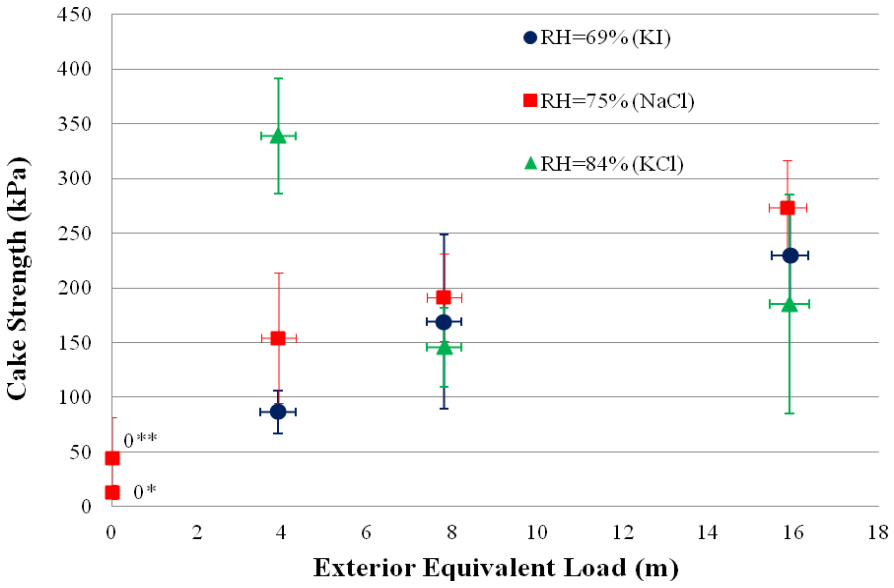

Figure 3.11 Cake strength versus external equivalent load with the variations of ambient air humidity

The analogous formations of data points (triangles) in Figure 3.10 and 3.11 signify that the external load hardly affects the cake strengths of potash specimens when the moisture adsorption humidity reach very high levels (e.g. 84%). In order to explain the observed result, the caking properties of the sample subgroups corresponding to the triangles should be analyzed. Sample porosity data in Table 3.7 illustrate that the internal gaseous space inside a potash specimen is obviously reduced when the potash specimen is strongly compressed with the high external load and moisture adsorption humidity. As shown in Table 3.8, the mean value data of X_r for the two sample sub-groups with the external equivalent loads ((7.8±0.41) and (15.9±0.42) metres) and adsorption humidity (84%) indicate that quite a bit of water remained inside each potash specimen. During the fracture test, it was observed that quite a few potash granules in each test cell were still in the wet state when the two sub-groups of potash samples were ruptured in the centrifuge. It can be reasoned that the reduced gaseous space in the top part of a potash specimen is possibly blocked by the recrystallized salt bridges in the same part during moisture desorption. The water evaporation and formation of crystal bridges were prevented in the closed bottom region of the specimen. The potash specimens with a high external load and adsorption humidity (e.g. 16 m and 84%) were partly caked in their top parts during drying. Once these specimens were tested in the centrifuge, the breaches first occurred in their non-caked bottom

parts and subsequently their caked top parts were fractured. The measured data of fracture rotary speed and calculated results of cake strength cannot effectively characterize the macroscopic caking states of these specimens. In other words, the very high external load and air humidity probably prevented the caking of potash granules lying deep in a bulk potash pile.

3.4 Summary

The sample preparation process was able to produce potash ring specimens with initial caking properties in steady state. The randomly paired internal and external plastic rings were capable of eliminating the mass biases of potash specimens originating from the size deviations of plastic rings.

The two factors, the external equivalent load and ambient air humidity, affected the caking properties and cake strength of potash specimens during sample preparation. A higher external load caused bigger reductions of compressed heights and porosities of potash specimens and sped up moisture adsorption processes inside potash specimens. The heights of potash specimens were hardly altered by the external load during moisture desorption. A rise of moisture adsorption humidity caused a corresponding increase of sample moisture content. The low moisture desorption humidity expedited the moisture desorption processes and generated small residual moisture contents of potash specimens. Higher moisture adsorption humidity and lower desorption humidity combined to result in higher moisture content differences of potash specimens.

Cake strengths of potash specimens were enhanced with an increase of moisture adsorption humidity and external load and a decrease of moisture desorption humidity when the moisture adsorption humidity did not exceed 75%. If the moisture adsorption humidity and external equivalent load reached very high levels (e.g. 84% and 16 m), some brine was sealed in the bottom part of a potash specimen and by the recrystallized salt in the top part of the specimen. The crystal bridges between potash particles did not form in its bottom part. Thus, the very high exterior load and air humidity prevent the strong agglomeration of potash granules situated deep in a huge potash pile.

CHAPTER 4

SIMULATION OF WATER DIFFUSION AND SORPTION IN POTASH SPECIMENS

4.1 Introduction

4.1.1 Problems for foregoing chapters

The data analyses of the caking properties and cake strengths of potash specimens failed to explain some experimental results observed during potash sample preparation and fracture test. For example, the experimental analysis presented in Subsection 3.3.1.4 showed that the moisture adsorption process could consume a longer time than its subsequent moisture desorption process. The data comparison on moisture content and cake strength for two sample sub-groups (Case 0* and Case 0**) revealed that the low moisture desorption humidity could shorten the drying time and increase the cake strengths of potash specimens. However, Wang et al. (2009) showed that long drying periods could enhance the cake strengths of potash specimens.

In addition, the moisture content of a potash specimen, as a macroscopic quantity, cannot quantify the moisture accumulated in any part of the specimen. Because a potash specimen adsorbs moisture from the ambient air through its own top surface, the local moisture content probably has non-uniform distributions in transient states inside the specimen. The occurrence of variational local moisture content implies that the number and sizes of crystal bridges generated during moisture desorption are different between parts of the specimen, and that the local tensile strengths in most parts are inconsistent with the cake strength of the specimen computed by the planar DEM model. In other words, the planar DEM model is probably ineffective for cake

strength estimation for a potash specimen if the condensed water does not uniformly distribute inside the potash specimen.

4.1.2 Objective of this chapter

A theoretical study of microscopic moisture transportation and water accumulation inside a potash specimen is developed to solve these problems mentioned in Sub-section 4.1.1. Chen (2004) presented that moisture adsorption and desorption processes inside a potash specimen without external compression were dominated by water vapour diffusion when the moisture content was less than 10% and particle sizes range from 0.9 to 1.18 mm. Numerical models of water vapour diffusion for uncompressed potash specimens is preferentially developed in this chapter, as shown in Figure 4.1.

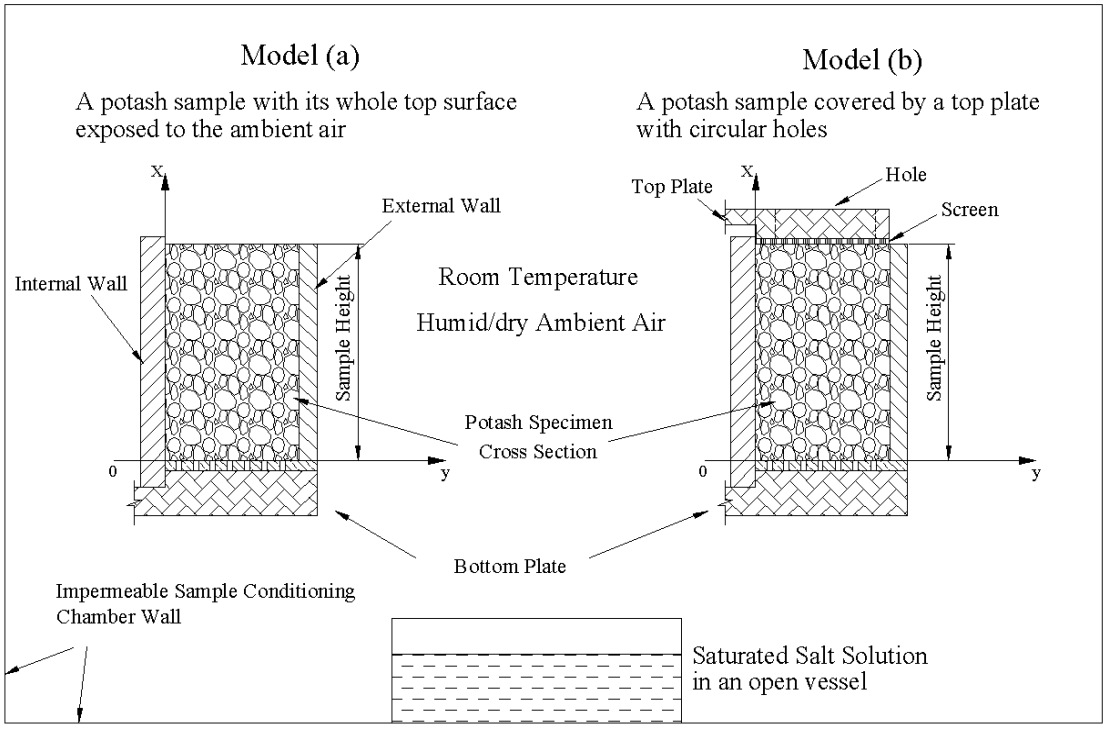

Figure 4.1 Schematics of uncompressed potash specimens placed in a humidity-controlled impermeable sample conditioning chamber during moisture adsorption and desorption

4.2 Numerical Model of Moisture Diffusion

4.2.1 Model assumptions

Figure 4.1 shows two schematics for cross-sections of uncompressed potash test cells, which are based on Case 0* and 0** during sample preparation. For Model (a), the top surface of a potash granular specimen is exposed to the humid or dry air in the sample conditioning chamber. For Model (b), a top clamping plate and screen, placed on the potash specimen, reduce the top interface area between the potash specimen and the ambient air in the chamber. Several important assumptions are used for the water vapour diffusion model.

a. Sample conditioning chamber

The air in the sample conditioning chamber is considered to be in the steady state with a constant relative humidity and room temperature. The free mass convection near test specimens can occur due to the very small variations of the total gas density.

b. Top clamping plate

The weight of a top plate and screen can be neglected relative to the stiffness of potash granules packed in a test cell. The top clamp plate and screen is deemed not to impact the shape and internal microscopic structures of the potash sample. Model (b) has the same condition of zero external loading as Model (a).

c. Internal thermal energy transfer

The initial temperature of potash specimens during sample preparation is the same as the room temperature. The research of Peng et al. (2000) shows that the enthalpy change of a test specimen in this research results in a temperature change of less than $1^{o}C$ during the long moisture adsorption and desorption processes. The very small temperature change is expected to insignificantly impact the bulk potash isotherm of the relative humidity and moisture content. The water vapour diffusion process inside a potash sample is hardly impacted by the trivial

temperature changes of the specimen. In other words, potash specimens are in the steady state at room temperature during sample preparation.

d. Homogenization of potash granular specimens

Because irregular potash granules with a small size range from 0.9 to 1.18 mm are randomly packed in each test cell, each potash specimen is assumed to be homogeneous and isotropic during sample preparation and have uniform physical properties in the initial state (e.g. porosity, density, and water vapour adsorption capacity) before moisture adsorption.

e. Water vapour and accumulated water distributions inside test samples

Water vapour is assumed to diffuse uni-dimensionally within a potash sample where moisture adsorption or desorption occurs on the particle surfaces. The bottom plate and internal and external walls are impermeable, as shown in Figure 4.1. The contact interface effects of diffusion through a particle bed at these walls are expected to be restricted to the distance about one particle diameter. The physical properties of potash particles and water vapour are considered to be homogeneous in any cross plane of a potash specimen perpendicular to the direction of water vapour diffusion. These assumptions are consistent with the homogeneous property modeling of porous media.

f. Boundary conditions

The top surface of a potash specimen is available for moisture exchange between the sample and the chamber air. The other three interfaces between the packed potash particles and the outer and inner plastic rings with a bottom plate are considered as impermeable boundaries. The total air density difference of the ambient air in the pre-conditioning chamber and the local air near the top sample surface can cause free mass convection.

g. The insignificant volume change of solid and liquid phases

The low moisture content indicates that the volume of condensed water is very small relative to the solid phase volume of potash particles. The salt impurities dissolved in condensed water cannot cause a significant decrease in the sizes of potash particles. With the dissolution of salt impurities, the condensed water becomes the salt solution and the liquid phase volume increases somewhat. Based on the research of Peng et al. (2000), the increased liquid phase volume can cancel out the decreased solid phase volume in a wetted potash sample. Thus, during moisture adsorption and desorption, it is thought that the solid phase change is neglected and the liquid phase change is equivalent to the increase and decrease of condensed water in a potash specimen.

4.2.2 Modelling of water vapour diffusion

The local volume averaging technique (Kaviany 1991) and the foregoing assumptions were used to develop the numerical model for one-dimensional water vapour diffusion. As shown in Figure 4.2, a control volume in a potash sample is defined as the unit element where water vapour and condensed water remain uniform throughout the sample preparation process. This definition also implies that each control volume has homogeneous moisture absorption and desorption properties. The values of all properties used in the numerical model are found in Appendix E. In the moisture adsorption stage, the regions above and below that are bordering the selected control volume have higher and lower relative humidity respectively. Control volumes at the same level are considered to have the same physical conditions. Water vapour molecules diffuse down through the selected volume (Refer to Figure 4.1 and 4.2). On the contrary, water vapour moves away from the control volume from bottom to top in the moisture desorption stage.

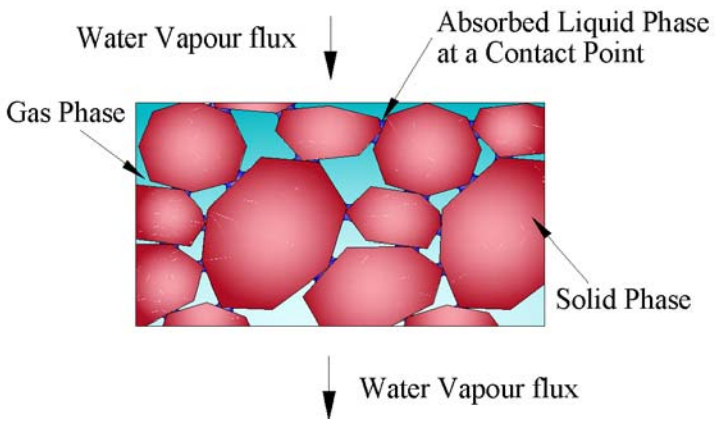

Figure 4.2 Water vapour diffusion through a control volume

a. Governing equation for water vapour diffusion within a potash sample

According to the mass conservation principles, a partial differential equation can be developed to characterize the dynamic course of moisture transfer and accumulation inside a potash granular sample:

$$\frac{\partial}{\partial t}\left(\varepsilon_g \rho_v\right) - \dot{m} = \frac{\partial}{\partial x}\left(D_{v,eff}\frac{\partial \rho_v}{\partial x}\right) \tag{4-1}$$

where the symbol, ρ_v, denotes the water vapour density inside a potash specimen, $\dot{m}$ is the mass rate of phase change (water vapour condensation or water evaporation) per unit volume, ε_g is the volume fraction of gas phase, $D_{v,eff}$ denotes the effective diffusion coefficient of water vapour in a potash specimen, which is expressed as

$$D_{v,eff} = \frac{\varepsilon_g \cdot D_v}{\tau} \tag{4-2}$$

where the symbol, D_v, is the diffusion coefficient of water vapour in air and τ is the tortuosity of potash granular specimen.

b. Boundary conditions

Based on Assumption f in Section 4.2.1, the bottom boundary condition at x=0 is expressed as,

$$\left.\frac{\partial \rho_v}{\partial x}\right|_{x=0} = 0 \tag{4-3}$$

The top boundary condition at $x=h$ is considered to be free mass convection. The mass conservation of water vapour at this interface can be formulated as,

$$D_{v,eff} \left.\frac{\partial \rho_v}{\partial x}\right|_{x=h} = h_m (\rho_{v,\infty} - \rho_v|_{x=h}) \tag{4-4}$$

where the effective diffusion coefficient, $D_{v,eff}$, may be determined by Equation (4-2), the free mass convection coefficient, h_m, is correlated to the Sherwood number, Sh, which is defined as

$$Sh = \frac{h_m L_c}{D_v} \tag{4-5}$$

where the symbol, L_c, denotes the characteristic length of potash specimen.

For the case of free mass convection, the Sherwood number, Sh, is usually correlated with the Rayleigh number, Ra, in Equation (4-6).

$$Sh = C \cdot (Ra)^n \tag{4-6}$$

The Rayleigh number is calculated by using the gravity acceleration, g, the effective difference of total gas density, $\Delta\rho_{g,eff}$, the characteristic length, L_c, the dynamic viscosity, v, the Schmidt number, Sc, and the average total gas density, $\rho_{g,m}$. That is,

$$Ra = \frac{g \cdot \Delta\rho_{g,eff} \cdot L_c^{\,3}}{\rho_{g,m} \nu^2} Sc \tag{4-7}$$

Equation (4-8) is used to estimate the effective difference of total gas density. The symbols, $\rho_g|_{\infty}$ and $\rho_g|_{x=h}$, respectively denote total gas densities for the overall environment in a conditioning chamber and the local surrounding near the top surface of a potash specimen. Although the temperature variation caused by water vapour condensation and salt dissolution is

trivial inside a potash specimen, the temperature variation appear to affect $\rho_g\big|_{x=h}$ and $\Delta\rho_{g,eff}$. Thus, the empirical coefficient, λ, is introduced in Equation (4-8) to estimate the effect of temperature change on $\Delta\rho_{g,eff}$. The coefficient is determined by comparing simulation results with experimental data.

$$\Delta\rho_{g,eff} = \lambda\left(\rho_g\big|_{\infty} - \rho_g\big|_{x=h}\right) \tag{4-8}$$

The following equations from (4-9) to (4-12) are used to calculate the total gas density, ρ_g,

$$\rho_g = \rho_a + \rho_v \tag{4-9}$$

$$\frac{P_a}{\rho_a} = R_a T \tag{4-10}$$

$$\frac{P_v}{\rho_v} = R_v T \tag{4-11}$$

$$P_{atm} = P_a + P_v \tag{4-12}$$

where the symbols, ρ_a and ρ_v, denote the partial densities of dry air and water vapour, P_a and P_v denote the partial pressures of air and water vapour, R_a and R_v are the air and water vapour constants, T is the constant room temperature for potash specimens and ambient air, and P_{atm} is the atmosphere pressure.

The characteristic length, L_c, was defined by Goldstein et al. (1973) as,

$$L_c = \frac{A_b}{P_b} \tag{4-13}$$

where the symbols, A_b and P_b, respectively denote the area and perimeter of the top surface of a potash specimen.

The air constant, R_a, is smaller than the water vapour constant, R_v, as shown in Appendix E. Based on Equation (4-10) and (4-11), the partial air density is higher than the partial water vapour density when their partial pressures are same. In other words, the total gas density of the dry air is heavier than the total gas density of the humid air. For Model (a) in Figure 4.3, when the local air near the top surface of a potash specimen becomes drier because of moisture adsorption, the total gas density of the local air will increase in the moisture adsorption stage. The air will uni-directionally move from top to bottom. During moisture desorption, the local air close to the potash sample becomes more humid compared with the outermost environment. The decrease of the total gas density causes the local air circulation as shown by Model (a) in Figure 4.3.

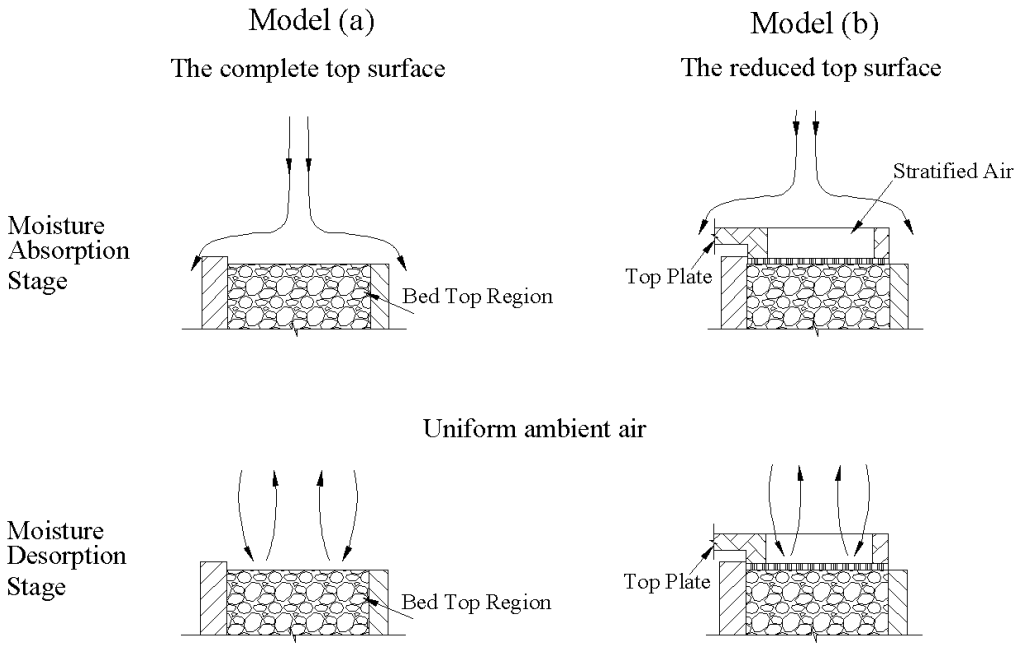

Figure 4.3 Free convection schematics for Model (a) and (b) during moisture adsorption and desorption

For Model (b) in Figure 4.3, holes inside the top plate can result in the air stratification to constrain the air bulk movement. However, free mass convection is still overwhelming beyond the top plate. It is thought that Model (b) has the similar boundary condition of free mass convection to Model (a). This is because holes in the top plate cause the air stratification that Model (b) has a much slower moisture adsorption rate than Model (a).

The top surface of a potash bed may be thought of as a horizontal rough ring plate to sustain the free convection of water vapour. The constant values of C and n in Equation (4-6) for this type of free convection are determined by referring to the research of Goldstein et al. (1973) and listed in Table 4.1.

Table 4.1 Values of constants for Equation (4-6)

The correlation constant, C	The power constant, n
0.96	$\frac{1}{6}$

c. Initial conditions of potash samples and ambient air in a chamber

The initial relative humidity ($\phi|_{x,t=0}$) of dry potash specimens is considered to be zero. The initial vapour density ($\rho_v|_{x,t=0}$) and phase change ($\dot{m}|_{x,t=0}$) are assumed to be zero as well,

$$\phi|_{x,t=0} = 0,\ \ \rho_v|_{x,t=0} = 0,\ \dot{m}|_{x,t=0} = 0 \tag{4-14}$$

The sample conditioning chamber keeps the room temperature and relative humidity (ϕ_∞) steady. The relative humidity is determined by the selected saturated brine (refer to Table 3.1), that is,

$$\phi_\infty = \phi_A \ or\ \phi_D \tag{4-15}$$

where the symbols, ϕ_A and ϕ_D, denote the invariable moisture adsorption and desorption humidity of ambient air.

d. Phase change

During sample preparation, the water vapour condensation and water evaporation cause the phase change (i.e. the conversion between gas and liquid phases) inside a potash specimen. The continuity equation is used to formulate the phase change,

$$\rho_l\left(\frac{\partial \varepsilon_l}{\partial t}\right)+\dot{m}=0 \tag{4-16}$$

where the symbol, ρ_l, denotes the water density, ε_l is the volume fraction of water in a potash specimen, and $\dot{m}$ is the quantity of phase change in a potash specimen expressed as,

$$\dot{m}=-\varepsilon_s \rho_s \frac{\partial X}{\partial t} \tag{4-17}$$

where the symbol, ε_s, is the volume fraction of potash particles in a test specimen, ρ_s denotes the potash crystal density, and X expresses the local moisture content inside a potash sample.

The volume fractions (ε_s, ε_l and ε_g) satisfy the following equation,

$$\varepsilon_s+\varepsilon_l+\varepsilon_g=1 \tag{4-18}$$

e. Isotherm of moisture content and relative humidity

Peng et al. (1999) pointed out that the impurities on the surfaces of potash particles were the main factors in determining the amount of liquid water captured by a potash specimen. They presented the multiple-stage bulk potash isotherms of the relative humidity and moisture content in the equilibrium state at room temperature by using his theoretical analysis and experimental data. However, with the improvement of potash handling processes in the past decade, the impurities on potash granular products have been possibly diminished to a lower level. The experimental data of the potash specimens prepared in this research and the method of Peng et al. were applied to obtain the double-stage fit isotherm curves of the equilibrium moisture content and relative humidity at room temperature for the current water vapour diffusion models, as shown in Figure 4.4.

The relative humidity, ϕ, is defined as

$$\phi=\frac{P_v}{P_{sv}} \tag{4-19}$$

where P_v denotes the partial pressure of water vapour and P_{sv} is the saturation pressure of water vapour (Appendix E).

The equations of the fit isotherm curves are as follows,

$$\text{Stage I:}\quad X = \frac{X_m \cdot C \cdot \phi}{(1-\phi)\cdot(1+(C-1)\phi)} \quad (\phi \le 43\%) \tag{4-20}$$

where X_m=0.00098, C=1.54, obtained by Peng et al. (1999)

$$\text{Stage II:}\quad X = \frac{1}{A + B\cdot\phi + C\cdot\phi^2 + D\cdot\phi^3} \quad (43\% \le \phi < 84\%) \tag{4-21}$$

where A= 11202, B= -43619, C= 57883, D= -25990. The calculated value of equilibrium moisture content at the relative humidity of 43%, measured data of equilibrium moisture content for the relative humidity of 69% and 75%, and the solubility of potassium chloride corresponding to the relative humidity of 84% at room temperature are applied to obtain coefficients in Equation (4-21) and the fit curve for Stage II in Figure 4.4. The correlation coefficient of the fit curve for Stage II is 99%.

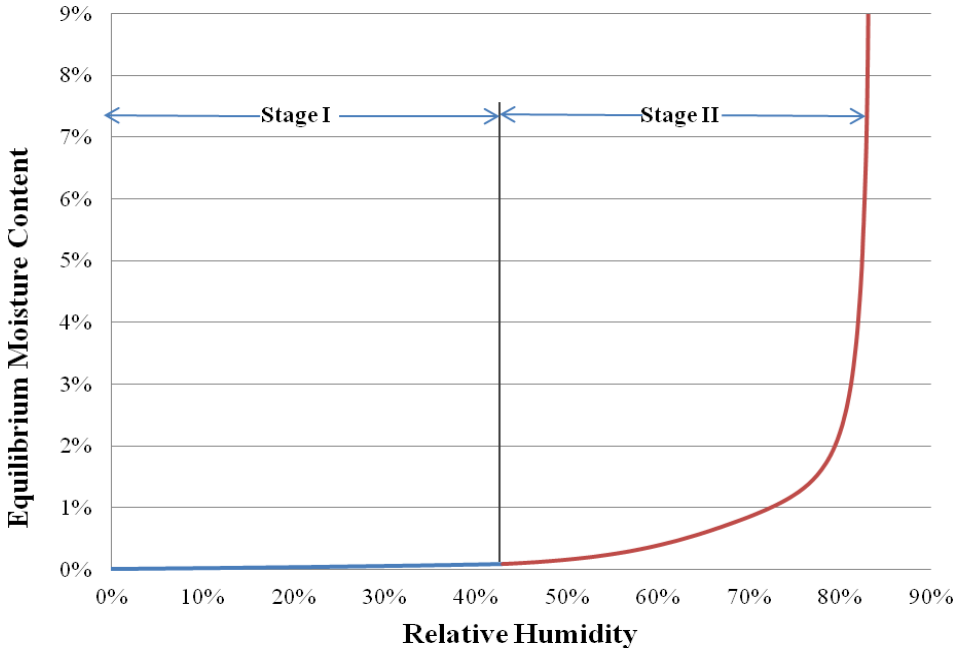

Figure 4.4 Bulk potash isotherm of equilibrium moisture content and relative humidity at room temperature

4.2.3 Mathematical Method

Backward time and central space finite difference operators (Minkowycz et al. 1988) were used to transform the governing equation, continuity equation, and boundary conditions to the group of linear equations shown in Appendix F. These linear equations were solved by the Gauss-Seidel iteration method (Rao, 2002) with a precise convergence criterion of 10^{-7}. Meanwhile, the summation for the residuals of these linear equations was controlled under a small number of 10^{-7}. Errors of mass balance on moisture absorption and desorption were limited to less than 1% as well.

4.3 Numerical Results and Discussions

The sensitivity studies of grid size (x) and time step (Δt) in Appendix G demonstrate that the numerical solutions of the water vapour diffusion model are reasonable in the mathematical aspect and in agreement with the corresponding experimental data when the grid size and time step respectively equal 0.5 mm and 6 s. The numerical model of water vapour diffusion inside the test cell can not only compute the free mass convection coefficient and sample moisture content measured during sample preparation but also predict the spatial distributions of the physical quantities in transient state inside a potash specimen, such as relative humidity and moisture content.

4.3.1 Free Mass Convection Coefficient

Figure 4.5 (a) and (b) show that the variations of free mass convection coefficients over storage time for Model (a) and (b). The free mass convection coefficients quickly drop at the short early stages of moisture adsorption and desorption. Subsequently, the rates of decrement become low. Especially for Model (b), the change curves of the free mass convection coefficients tend to be smooth as the water vapour density differences between the ambient air and potash specimens are reduced. The two figures also illustrate that the values of the free mass convection coefficients in the early stage of moisture desorption are higher than in the early stage of moisture adsorption. The obvious differences of free mass convection coefficients between moisture adsorption and desorption indicate that the local air circulation during moisture

desorption can cause faster mass transfer relative to the uni-directional air flows over moisture adsorption, as shown in Figure 4.3.

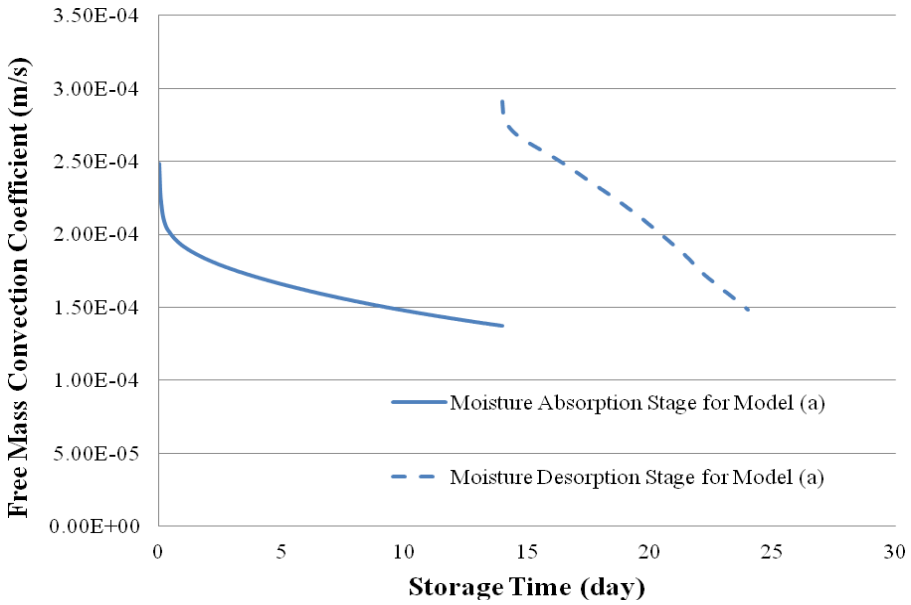

(a)

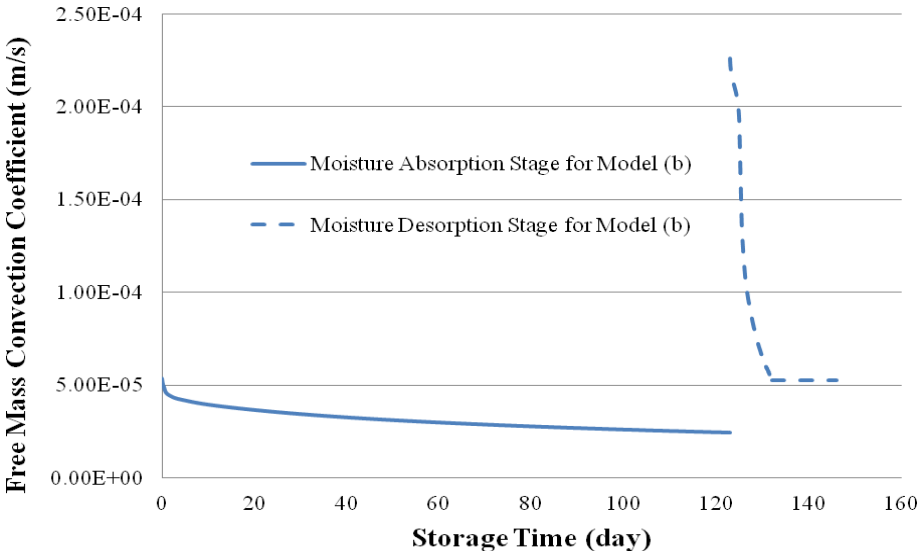

(b)

Figure 4.5 Plots of free mass convection coefficient versus storage time for Model (a) and (b)

For Case 0* and 0**, respectively corresponding to Model (a) and (b), the internal structure and properties of an uncompressed potash specimen (i.e. height, porosity, and impurity contents) nearly kept constant during moisture adsorption and desorption with the negligible effect of condensed water. This meant that the effective diffusion coefficient presented in Equation (4-1) hardly changed in the potash specimen during sample preparation. For other cases with nonzero external loads, the sample height and porosity decreases, as shown in Figure 3.6 and 3.7, indicated that the effective diffusion coefficient of a compressed sample for moisture desorption was smaller than for moisture adsorption. In other words, the water vapour diffusion capacity inside an uncompressed or compressed potash sample did not speed up the moisture desorption process. Hence, the free mass convection boundary quantified by Equation (4-4) is the major factor to explain why the moisture desorption processes have shorter time constants than the foregoing moisture adsorption processes, as shown in Figure 3.8 and 3.9.

4.3.2 Sample moisture content and model validation

The numerical results of sample moisture content for Model (a) and (b), plotted in Figure 4.6 (a) and (b), are in agreement with the corresponding experimental data of Case 0* and 0**. The agreement signifies that the numerical model of water vapour diffusion is effective in simulating the moisture adsorption and desorption processes of potash specimens without external compression. The rates of water accumulation and evaporation in Model (a) and (b) are relatively high at the start and then get lower over storage time for moisture adsorption and desorption. At inflexion points shown in Figure 4.6 (a) and (b), numerical results and experimental data of maximum sample moisture content both approach the equilibrium moisture content of potash specimens (Refer to Figure 4.4).

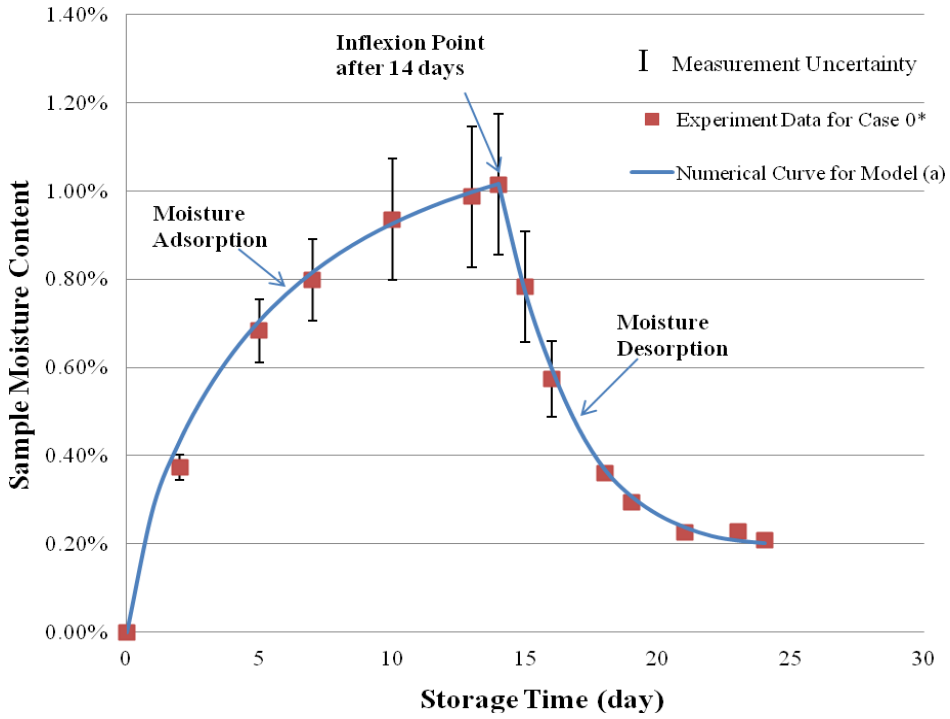

(a)

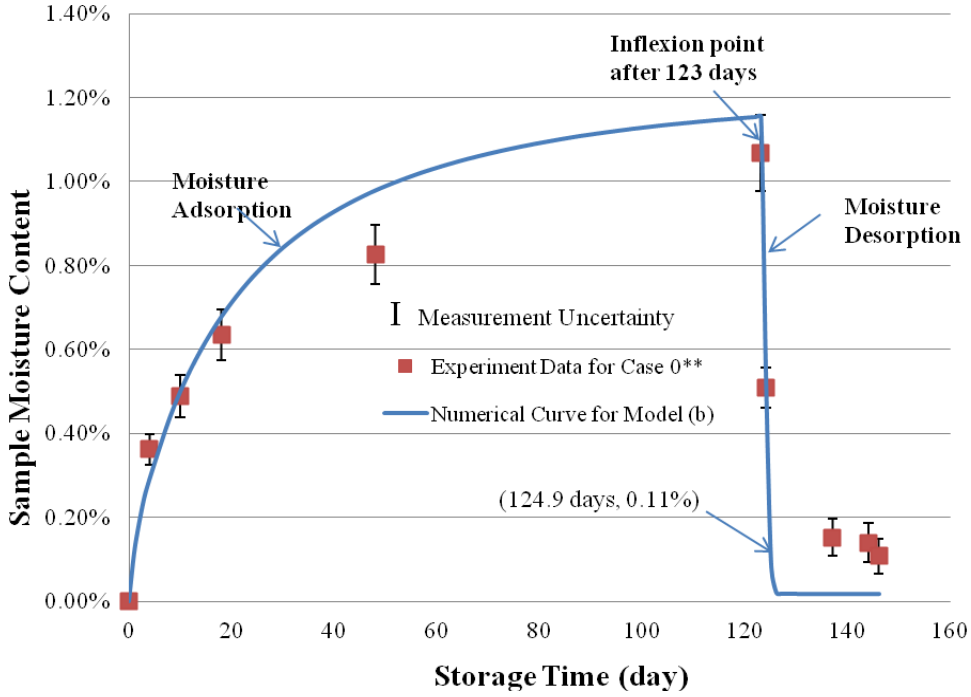

(b)

Figure 4.6 Comparison of simulated and measured sample moisture content over storage time for Model (a) and (b)

Figure 4.6 (a) shows that the experimental data of sample moisture content were lower than the simulation curve in the early stage of moisture adsorption. The internal space of a sample pre-conditioning chamber was limited, relative to a sub-group of about ten potash samples without external compression (Refer to Figure 3.4). The finite space possibly confined the free mass convection of local air near potash samples, the top surfaces of which were completely exposed to the ambient air. With the decrease of the free mass convection coefficient, the effect of the finite space in the pre-conditioning chamber on free mass convection was reduced to the trivial level. Hence, the simulation curve of sample moisture content was consistent with the corresponding data points in the later stage of moisture adsorption.

For Model (b), the deviation between experimental data and numerical results occurs in the later stage of moisture adsorption, as shown in Figure 4.6 (b). In Case 0**, the top surfaces of potash samples, exposed to the ambient air, were highly reduced by the ring screens and top clamping plates with circular holes. Compared with the reduced top surface areas of potash specimens, the space in the pre-conditioning chamber was enough to perform the free mass convection above these potash samples in the early stage of moisture adsorption. While the free mass convection coefficient diminished, the air stratification in circular holes became the significant cause to restrict the free mass convection between the potash samples and the ambient air. Therefore, the experimental data of sample moisture content were lower than the theoretical curve in the later moisture adsorption stage.

In the following moisture desorption course, the experimental data and simulation curves in Figure 4.6 (a) and (b) show that the sample moisture content quickly decreases in the early stage and then trends to a constant in the late stage. Model (a) gives a numerical curve of moisture desorption consistent with the experimental data of Case 0*. For Model (b) in Figure 4.6 (b), similar to its moisture adsorption process, the experimental data of sample moisture desorption are lower than the corresponding numerical results in the final stage of moisture desorption. For Case 0**, the residual moisture content of potash samples diminished to about 0.11% after the 146 days moisture adsorption/desorption process. The corresponding simulation result in Figure 4.6 (b) shows that the residual sample moisture content drops to 0.11% after about 125 days. The contrast implies that the brine bridges in a potash specimen were partly

transformed to the crystalline bridges during moisture desorption and that some brine was possibly sealed in a potash sample by the crystalline bridges. Thus, in the final stage of moisture desorption, the experimental data of sample moisture content were higher than the corresponding numerical results.

As shown in Table 4.2, the measured data for residual sample moisture content for Case 0* and 0** are different from the corresponding numerical result of Model (a) and (b). Their own relative errors indicate that the slower moisture desorption process can cause more water to evaporate and more salt to recrystallize near contact regions between potash particles. It is consistent with the conclusion of Wang et al. (2009). However, it is found in Table 4.2 that Case 0** has a measured residual sample moisture content much smaller than Case 0*. With the similar maximum sample moisture content, potash specimens for Case 0** have a higher moisture content difference and cake strength than Case 0* (Refer to Tables 3.8, 3.9, and 3.10). Thus, the sample moisture content difference, relative to the maximum and residual sample moisture content, is one of the important parameters to determine the cake strength of potash specimens.

Table 4.2 Data comparisons of the measured residual moisture content, corresponding numerical results, and relative errors between Case 0* and Case 0**

	Case 0*	Case 0**
Relative humidity for desorption	52%	11%
Measured residual MC (X_r)	0.21%	0.11%
Numerical results of X_r	0.20%	0.02%
Relative error	4.8%	82%

4.3.3 Variation of air humidity

The water vapour diffusion model can compute the local relative humidity in transient states for a potash specimen. The local relative humidity was used to quantify the local water vapour distribution anywhere inside a specimen and calculate the corresponding local moisture content in the specimen. The Spatial relative humidity distributions of Model (a) and (b) during moisture adsorption and desorption are respectively plotted in Figure 4.7 (a) and (b). The local relative humidity distributions of Model (a) show distinct gradient variations after the first day of

moisture adsorption and tend to be uniform by the two ends of moisture adsorption and desorption, that is, the solid and dashed lines in Figure 4.7 (a). The almost level solid and dashed lines mean that water vapour may be considered to be uniformly distributed in a potash sample after moisture adsorption and desorption for Case 0*.

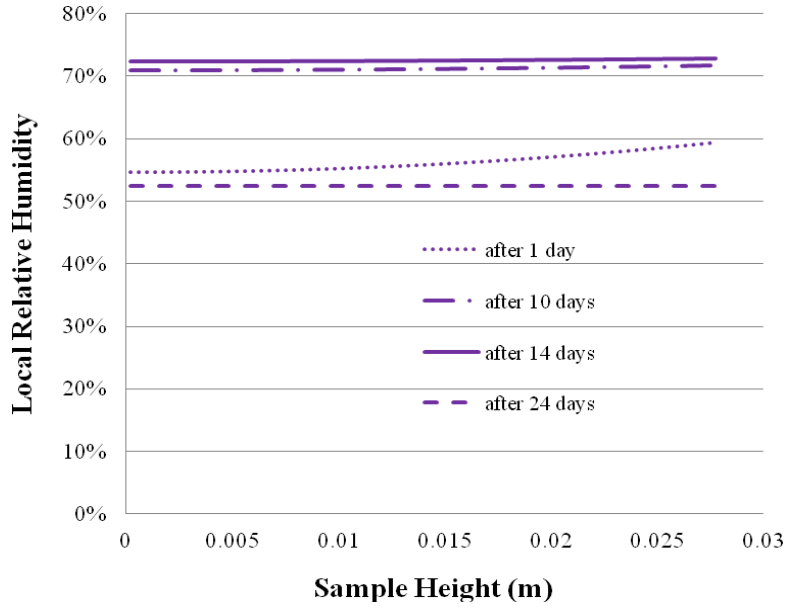

(a)

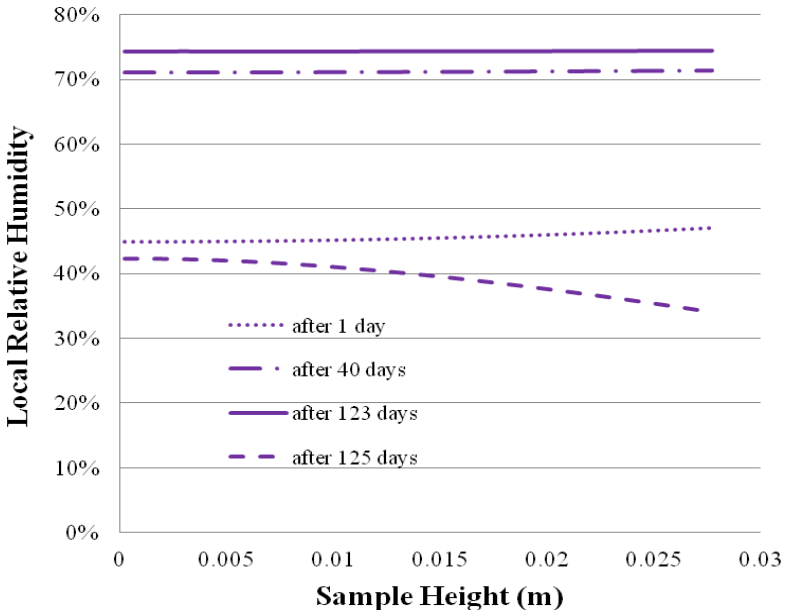

(b)

Figure 4.7 Simulated spatial distributions of the relative humidity inside a potash bed at multiple time points for Model (a) and (b)

Except for the dashed curve in Figure 4.7 (b), the nearly even local relative humidity distributions of Model (b) signify that the partial water vapour density at any position within a potash specimen increases at almost the same pace in the whole moisture adsorption process for Case 0**. These relative humidity lines also imply that the water vapour diffusion rates inside a potash sample are sufficiently high relative to the reduced free mass convection near the top surface of the sample.

4.3.4 Accumulation of liquid water

Equations (4-20) & (4-21) were applied in Model (a) and (b) to predict the local moisture content variations inside potash specimens for Case 0* and 0**. As shown in Figure 4.8 (a) and (b), Model (a) and (b) give the local moisture content distributions analogous to their own spatial arrangements of local relative humidity plotted in Figure 4.7 (a) and (b).

The nearly level solid and dashed lines of local moisture content in Figure 4.8 (a) correspond to the inflexion point and end point of the sample moisture content curve in Figure 4.6 (a). The solid and dashed lines of Model (a) indicate that the maximum and residual local moisture contents evenly distribute in a potash specimen. It is also expected that the differences between the two moisture contents are constant in the specimen for Case 0*.

Similar to Model (a), the level solid line of Model (b) in Figure 4.8 (b), corresponding to the inflexion point in Figure 4.6 (b), shows the even distribution of maximum local moisture content in a potash specimen for Case 0**. The dashed line of Model (b) is related to the data point (124.9 days, 0.11%) in Figure 4.6 (b). The sample moisture adsorption and desorption period for Case 0** is 146 days. The simulation curve in Figure 4.6 (b) shows that the numerical result drops to the measured value of residual sample moisture content (0.11%) after about 125 days. The variation of sample moisture content is trivial in the remaining 16 days. This also means that the dashed line in Figure 4.8 (b) represents the final distribution of local moisture content in a potash specimen at the end of moisture desorption. The almost constant interval between the solid and dashed lines in Figure 4.8 (b) signifies that the difference between local maximum and residual moisture content is very similar for Case 0**.

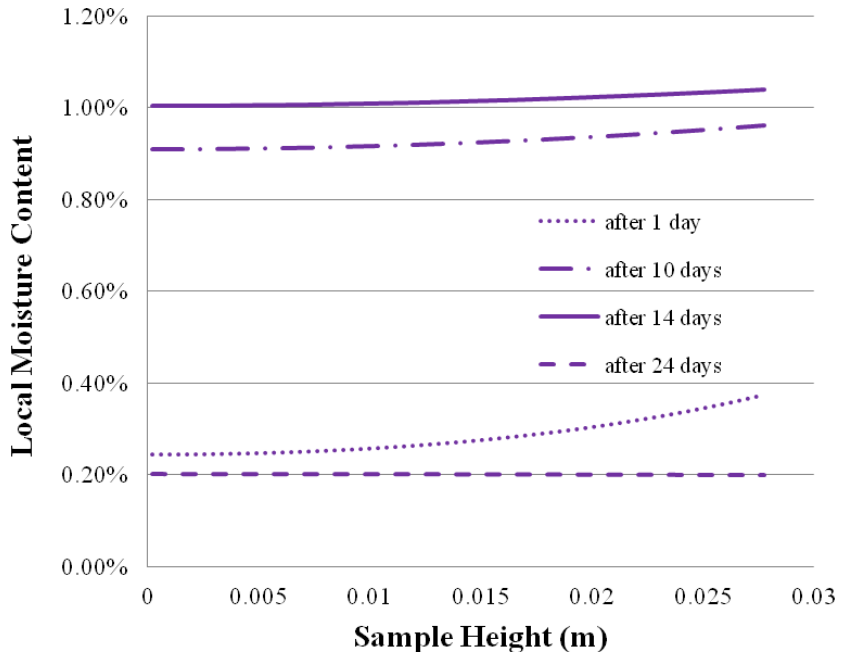

(a)

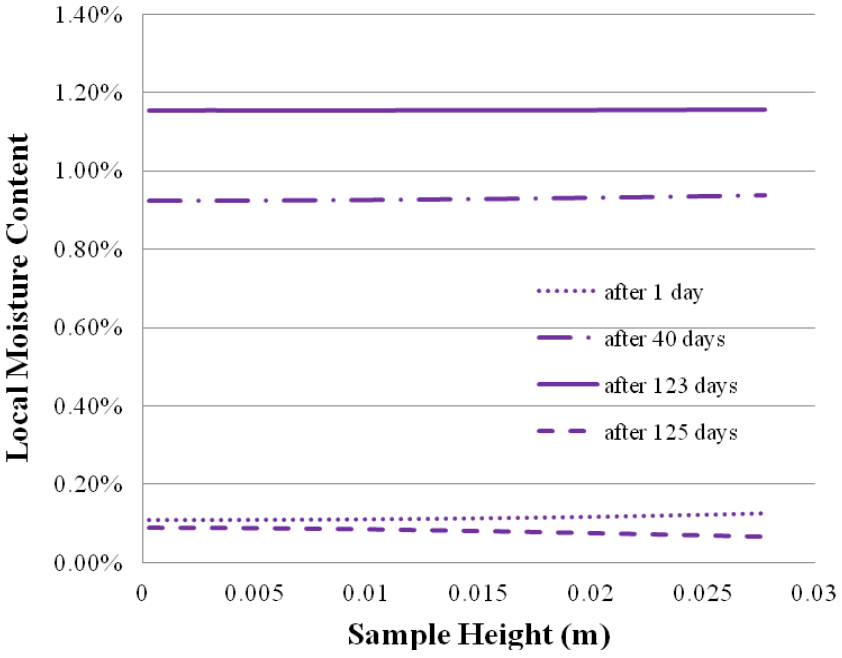

(b)

Figure 4.8 Simulated spatial distributions of moisture content inside a potash bed at multiple time points for Model (a) and (b)

The moisture content difference is the main factor in determining the tensile strength and sizes of crystal bridges inside a potash specimen. The uniform difference of local maximum and residual moisture contents (solid and dashed lines) signifies that crystal bridges are almost same inside a potash specimen for Case 0* and 0**. It is also shown that the sample cake strength computed by the planar DEM model can effectively quantify the local tensile strength anywhere within an uncompressed potash specimen for Case 0* and 0**.

4.4 Summary

The numerical model of water vapour diffusion is able to predict spatial distributions of the local relative humidity and moisture content in transient states and compute changes of the free mass convection coefficient and sample moisture content over storage time. Numerical results on the sample moisture content are in agreement with the corresponding experimental data for Case 0* and 0**. The agreement demonstrates that the water vapour diffusion model can reasonably simulate the moisture adsorption and desorption processes of potash specimens without external loads.

The calculated values of free mass convection coefficient during sample moisture desorption are much higher than during moisture adsorption. The contrast indicates that the local air circulation near potash specimens during moisture desorption can cause a higher mass transfer rate than the uni-directional air flow from top to bottom during moisture adsorption. The comparison result can explain the experimental phenomenon that the moisture adsorption process of potash specimens consumes a longer duration than the subsequent desorption course for the same specimens.

In long moisture adsorption and desorption processes, the uniform spatial distributions of local moisture content in transient states signify that the differences of the maximum and residual local moisture content inside a potash sample are almost constant. This prediction implies that the crystal bridges inside the potash specimen are similar. It is shown that the planar DEM model is effective in the cake strength estimations for potash specimens without compression

The comparisons of the simulation results and experimental data of sample moisture content for Case 0* and 0** show that the higher moisture desorption relative humidity can generate a slower drying rate and cause relatively more recrystallized salt. This result is consistent with the conclusion of Wang et al. 2009. However, a lower desorption relative humidity can result in a smaller residual sample moisture content. With the similar maximum sample moisture content, smaller residual sample moisture content means a bigger difference of sample moisture content, which can determine the tensile strength and sizes of crystal bridges between potash particles. That is to say, the lower moisture desorption relative humidity can cause the higher cake strength of potash specimens without compression when the adsorption relative humidity is constant.

CHAPTER 5

CORRELATION OF POTASH CAKE STRENGTH AND STORAGE CONDITIONS

5.1 Introduction

The literature on the caking of granular media shows that researchers place emphasis on correlations between caking properties and cake strength of granular media. For example, Leaper et al. (2003) thought that the properties of caked sugar samples, such as porosity, particle size, and crystal bridge strength, determined cake strengths of sugar samples. Wang et al. (2009) found that the initial moisture content and drying time constant also impacted the cake strength of potash granular specimens besides potash particle sizes. These studies were not concerned with storage conditions, which can also affect the caking processes of granular media. Before using these correlations, a lot of experiments have to be done to obtain data of caking properties.

Walker et al. (1999) found that agglomerate strengths of soft NPK fertilizer granules were linearly enhanced with an increase of external pressure. In the current research, the experimental data analyses indicated that the storage conditions, the external load and ambient air relative humidity, influenced caking properties and cake strength of potash specimens during potash caking. The external load and ambient air relative humidity were found to be the main factors in determining the cake strength of potash samples because the potash particle size and salt impurity contents on potash particle surfaces were considered as constants in this research. Relative to caking properties required for correlations of Leaper and Wang, data of external load and ambient air relative humidity can be easily measured on stroage sites. Therefore, a new correlation is developed in this chapter to predict the cake strength of bulk potash by using the external equivalent load and ambient air relative humidity.

5.2 Multi-Factor Correlation for Cake Strength

5.2.1 Influential factors of cake strength

The correlation of Wang et al. (2009) for uncompressed potash specimens showed that the cake strength, σ_c, was proportional to the initial moisture content, inversely proportional to the square of particle size, and had a power-function relation with the drying time constant. Their correlation is written as

$$\sigma_c = C \cdot S \tag{5-1}$$

where the symbol, σ_c (Pa), denotes the cake strength of a potash sample; the symbols, C and S, are defined as the correlation coefficient and characteristic parameter. C is equal to 192 with a dimension of (kPa·min$^{-0.4}$·mm^2) and the expression for S is,

$$S = t_d^{\,0.4} X_i d_{pm}^{\,-2} \tag{5-2}$$

where t_d is the specimen drying time constant (min), defined as the time required to achieve 63% of the maximum change after a step change in the ambient air conditions, X_i denotes the initial moisture content before drying in the paper of Wang et al. (2009) or the maximum sample moisture content in this research, d_{pm} is the mean value of potash particle diameter (mm).

The Rumpf's equation for sugar tensile strength modified by Leaper et al. (2003) is

$$\sigma_c = F_b \frac{9}{8} \frac{(1-\varepsilon)}{\varepsilon} d_{pm}^{\,-2} \tag{5-3}$$

where F_b denotes the tensile fracture force of crystal bridge (N) and ε is the porosity of a specimen. Leaper et al. defined the crystal bridge fracture force as

$$F_b = \sigma_b \pi r_b^{\,2} \tag{5-4}$$

where the symbols, σ_b and r_b, repectively denote the tensile fracture strength (Pa) and cross sectional radius (m) of a crystal bridge.

Leaper et al. thought that the liquid bridge between sugar particles had the same volume of the corresponding crystal bridge after drying. Dependent on the research of Tanaka (1978) for solid spheres without external compression, r_b can be determined by the average particle diameter, d_{pm}, and the volume of liquid bridge, V_b. That is,

$$r_b = 0.41 \cdot d_{pm} \left(\frac{8V_b}{(d_{pm})^3} \right)^{1/4} \tag{5-5}$$

By contrast, it is found that the maximum sample moisture content, X_i, in Equation (5-2) can determine the parameters, V_b and r_b, in Equation (5-5). The drying time constant, t_d, affects the average tensile fracture strength of crystal bridges, σ_b. The porosity of potash specimens, as a constant in the research of Wang et al. (2009), is one of the components, which constitute the correlation coefficient C in Equation (5-1). Hence, Equation (5-1) is an expression equivalent to Equation (5-3).

Equation (5-3) shows that a unique crytal bridge fracture force is used to calculate the cake strength of a potash specimen. The crystal bridges inside a potash specimen are considered to be almost the same. Analogous differences between the maximum and residual local moisture contents shown in Figure 4.8 (a) and (b) indicate that similar quantities of saturated brine are evaporated anywhere inside a potash sample without external compression. It is expected that analogous crystal bridges are formed between potash particles for the whole sample. Therefore, Equation (5-3) applies to the potash specimens for Case 0* and 0**.

In long moisture adsorption and desorption processes, the maximum and residual moisture content of potash specimens for Case 0* and 0**, X_i and X_r, approach their own equilibrium values of moisture content corresponding to the moisture adsorption and desorption humidity at room temperature, as shown in Table 3.8 and Figure 4.4. It is expected that the uniform spatial distributions of the maximum and residual local moisture contents can be certainly obtained. Other sub-groups of potash specimens with nonzero external loads and relative humidity of 69% and 75% basically have faster moisture adsorption rates than Case 0** and their own maximum sample moisture content, X_i, approaches the corresponding equilibrium

values of moisture content as well. Thus, it is believed that a compressed specimen should have a uniform spatial distribution of the maximum local moisture content after adsorption.

The residual local moisture content in a compressed specimen is probably nonuniformly distributed. Figure 3.9 illustrates that the compressed specimens follow a similar moisture desorption process to the uncompressed specimens. It is thought that the nonuniformity of residual local moisture content is trivial relative to the uniform maximum local moisture content. That is to say, the differences of maximum and residual local moisture contents are considered to be similar inside compressed potash specimens with the adsorption relative humidity of 69% and 75%. The analogous local moisture content differences signify that the crystal bridges inside a compressed specimen are almost the same. Therefore, Equation (5-3) applies to the compressed potash specimens.

The two macroscopic parameters, X_i and X_r, can be used to respectively index the maximum and residual local moisture contents almost uniformly distributed inside compressed and uncompressed potash specimens. The sample moisture content difference (ΔX) of X_i and X_r can determine the fracture force of similar crystal bridges (F_b in Equation (5-4) inside a specimen with or without compression. The planar DEM model is effective for cake strength predictions of the potash specimens prepared with the adsorption relative humidity of 69% and 75%.

Equations (5-3), (5-4), and (5-5) suggest that the compressed sample height and porosity influence the cake strength of a potash specimen. The height alteration of compressed samples implies an increase of interparticle contact areas which determine the locations of recrystallized salt and affect the fracture force of crystal bridges. The compressed porosity can result in the occurrence of extra contact regions inside a specimen to enhance the cake strength. Data for the compressed sample height and porosity are collected in Tables 3.6 and 3.7. If the crystal bridge fracture force inside a specimen was known, the specimen cake strength could be calculated. In fact, the properties of crystal bridges are hardly obtained through experiments and literature. Because the cake strength of a potash specimen can be predicted by the planar DEM model, the crystal bridge fracture force in the specimen can be obtained by using Equation (5-3).

5.2.2 Variables in Correlation

The caking properties that quantify variations of potash specimens in moisture adsorption and desorption processes, are designated here as the process quantities of potash specimens. The values of caking properties measured by the two ends of moisture adsorption and desorption can respectively characterize the final quasi-equilibrium states of potash specimens after moisture adsorption and desorption. Quantities such as compressed sample heights (h_{ca} & h_{cd}), compressed sample porosities (ε_{ca} & ε_{cd}), and maximum and residual sample moisture contents (X_i & X_r) after moisture adsorption and desorption, may be termed the quasi-state parameters of potash specimens. The data analyses in Section 3.3 of Chapter 3 signify that the external equivalent loads and ambient air relative humidity, as the state parameters of storage conditions, dominate the alterations of these caking properties. Therefore, the external equivalent load and ambient air relative humidity were defined as independent variables to develop the new correlation of predicting cake strength.

During sample preparation, it took long periods for potash specimens to reach sample moisture contents close to equilibrium moisture contents corresponding to levels of moisture adsorption humidity at room temperature. However, in courses of potash handling and transportation, bulk potash products always experience forced convection conditions, which can speed up moisture adsorption and desorption processes. Experimental data of Zhou (2000) showed that potash granular samples could obtain their equilibrium moisture contents with forced convection storage conditions in several hours. Hence, the new correlation can predict the cake strength of compressed bulk potash with a wide range of storage periods. The applicable ranges of the independent state parameters were determined by the sample preparation process in Chapter 3, as shown in Table 5.1.

Table 5.1 The application ranges of state parameters for Equations (5-6) and (5-7)

Moisture Absorption and Desorption Type	Free Mass Convection
RH for Moisture Absorption	69%-75%
RH for Moisture Desorption	11%-52%
Equivalent External Load (m)	0-16
Potash Particle Size (mm)	0.9-1.18
Moisture Content	<1.2%

5.2.3 Correlation development

Because cases with the zero external load are included, a modified characteristic parameter *S'* , corresponding to the parameter *S* in Equation (5-2), is written as

$$S' = \phi_A{}^a \phi_D{}^b (H+1)^c \tag{5-6}$$

where ϕ_A and ϕ_D denote the relative humidity for moisture absorption and desorption expressed as a fraction less than 1, *H* is the external load equivalent to the nominal sample depth with the dimension of metre.

In this research, the potash particle sizes ranged from 0.9 to 1.18 mm. The average diameter of potash particles (1.04 mm), as a constant, is included in the coefficient, *C*. the correlation may be expressed as

$$\sigma_c = C \cdot S' \tag{5-7}$$

Test data for eleven sample sub-groups, shown in Table 5.2, were used to determine the best fit line by multiple-variable linear regression.

Table 5.2 Data for relative humidity for moisture absorption and desorption processes, external load, and average cake strength of the eleven sub-groups of potash specimens

Number	RH for Absorption	RH for Desorption	Nominal sample depth (m)	External Equivalent Load (m)	Average Cake Strength (Pa)
1	75%	52%	0	0	1.32×10^4
2	75%	11%	0	0	4.43×10^4
3	69%	11%	4	3.90	8.65×10^4
4	75%	11%	4	3.90	1.54×10^5
5	84%	11%	4	3.90	3.39×10^5
6	69%	11%	8	7.79	1.69×10^5
7	75%	11%	8	7.79	1.91×10^5
8	84%	11%	8	7.80	1.46×10^5
9	69%	52%	16	15.92	2.30×10^5
10	75%	52%	16	15.84	2.73×10^5
11	84%	52%	16	15.76	1.85×10^5

Figure 5.1 shows the best fit line for Equations (5-6) and (5-7). The coefficient, *C*, was found to be equal to 41702 Pa/m$^{0.96}$and the power index, *a*, *b*, and *c*, respectively, are 3.91, -0.37, and 0.96. The correlation coefficient of linear regression, $\hat{r}$, is 0.95. Equations (5-6) and (5-7) may therefore be rewritten as

$$S' = \phi_A^{\,3.91}\phi_D^{\,-0.37}(H+1)^{0.96} \tag{5-8}$$

$$\sigma_c = 41702 \cdot S' \tag{5-9}$$

The negative exponent of ϕ_D in Equation (5-8) shows that the cake strengths of potash specimens increase as the moisture desorption humidity drops. The result is consistent with the analysis in Subsections 3.3.2 and 4.3.2. The moisture content difference between X_i and X_r impacts the fracture force of crystal bridges. The low moisture desorption humidity can generate a large moisture content difference to enhance the cake strengths of potash specimens. Therefore, the exponent of ϕ_D is negative in Equation (5-8).

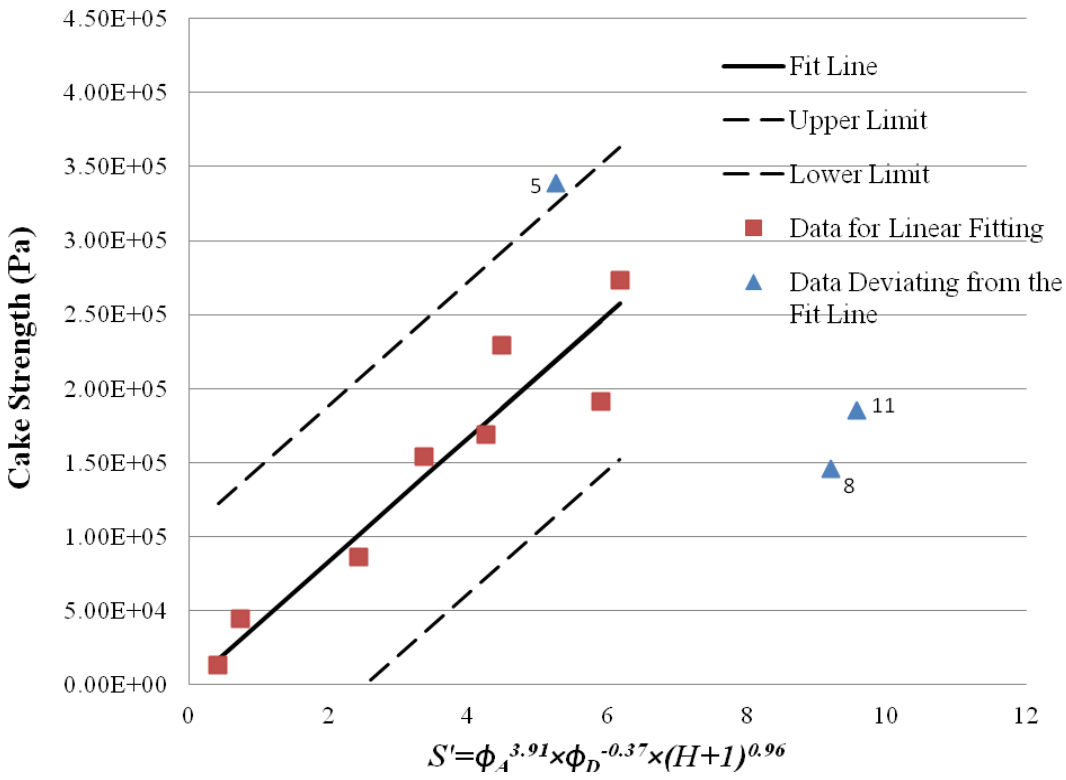

Figure 5.1 Data and linear fit for the average cake strength of the eleven sample sub-groups with lower and upper uncertainty limits for Equation (5-9)

Figure 5.1 illustrates that eight experimental data points (squares) have a good fit with the correlation expressed by Equations (5-8) and (5-9). The eight data points are the average cake strengths of the eight sample sub-groups with three nomimal sample depths (0, 4, and 8 m) and two levels of moisture adsorption relative humidity (69% and 75%), as shown in Table 5.2. Three other data points (triangles) in Figure 5.1, corresponding to the average cake strengths of No. 5, 8, and 11 in Table 5.2, deviate from the fit line. No. 5, 8, and 11 represent the three subgroups of potash specimens individually with the three nominal sample depths and the same moisture adsorption humdity of 84%. Table 3.1 and Figure 4.4 signify that the expected moisture content value for the three sample sub-groups is much smaller than the corrsponding value in the equilibrium state at the ambient air relative humidity of 84%. According to the analysis in Subsection 5.2.1, it may be conjectured that the spatial distibutions of local moisture content for the three sub-groups of specimens were nonuniform. The observed results of fracture tests

mentioned in Subsection 3.3.2 also indicate that a little water was retained in the bottom region of each potash specimen after desorption when the high external equivalent load and relative humidity (e.g. 16 m and 84%) were applied to potash specimens during moisture adsorption. The observed results verify the conjecture derived from Subsection 5.2.1. When these incomplete-caked samples ruptured in the centrifuge, the measured fracture rotary speed actually related to the caking state in the bottom part of the sample. For the three sub-groups of specimens, the cake strength results computed by using the planar DEM model and fracture rotary speed data are not equivalent to the macroscopic tensile strength values determined by the sample moisture content differences (ΔX), as mentioned in Subsection 5.2.1. Hence, the sample cake strength data points (triangles) for the three sample sub-groups deviate from the fit line shown in Figure 5.1.

5.3 Conclusions

A new correlation was successfully developed to predict the mutual impacts between ambient air relative humidity for moisture absorption and desorption and external equivalent load on potash sample cake strength. The correlation shows that the cake strength of potash specimen is enhanced with an increase of moisture absorption relative humidity and external equivalent load and a decrease of desorption relative humidity, and applies as long as the adsorption relative humidity does not exceed 75%. The correlation is not applicable for cases when the moisture adsorption relative humidity is 84%.

CHAPTER 6

SUMMARY, CONCLUSIONS AND FUTURE WORK

6.1 Summary

The caking of bulk potash is a universal phenomenon in the potash industry. Potash granules can be strongly agglomerated in the bottom region of a stored potash pile. Besides the inherent hygroscopicity of bulk potash, the external conditions, such as ambient air relative humidity and external compressive load, have considerable influences on the cake strength of bulk potash. In order to investigate potash caking properties and cake strength altered by the external conditions, this research was separated into the following four parts: DEM modelling, sample preparation & fracture testing, moisture transfer simulation, and cake strength correlation. The tasks accomplished in every part are summarized as follows,

a. A planar DEM model was developed to predict the tensile contact forces inside a potash specimen and estimate the sample cake strength. Comparison with the solid continuum model of Wang et al. (2006) showed the validity and merits of the DEM model. The fracture behaviour of a caked potash specimen in the centrifuge was predicted by the planar DEM model.

b. The sample preparation process of Wang et al. (2006) was used to prepare potash ring specimens. The calibrated springs and saturated salt solutions were used to respectively generate external loads equivalent to nominal sample depths in a potash pile and ambient air relative humidity for the sample compression and caking storage. Caking properties of potash specimens were measured during caking storage. After caking, the centrifuge fracture method of Wang et al. (2006) was applied to test the fracture rotary speed of each specimen which was input into the planar DEM model to compute the cake strength

of each specimen. The relevant data analyses showed the effects of the variable external equivalent load and ambient air relative humidity on caking properties and cake strengths of potash specimens with and without external compression.

c. A numerical model of water vapour diffusion with the boundary condition of free mass convection was developed to study the microscopic moisture transportation and accumulation inside an uncompressed potash specimen during caking storage. This model was able to predict variations of the free mass convection coefficient and sample moisture content over storage time and show spatial distributions of the local relative humidity and moisture content in transient states inside an uncompressed potash specimen. In order to confirm the numerical model, the numerical results of sample moisture content were compared with the corresponding experimental data. The physical quantities exhibited by the model (i.e. free mass convection coefficient, sample moisture content, and local moisture content in transient states) were analyzed to solve some problems found during sample preparation and fracture testing, such as the difference of moisture adsorption and desorption durations, the effect of moisture desorption relative humidity on salt recrystallization, and the crystal bridge uniformity in a potash specimen.

d. The influences of sample caking properties on the cake strength of potash specimens were studied. The crystal bridge uniformity and DEM model applicability for compressed potash specimens were discussed. A correlation between cake strength, relative humidity for moisture adsorption and desorption, and external equivalent load were obtained by using the multivariable linear regression.

6.2 Conclusions

With the accomplishment of each part, the relevant conclusions are drawn as follows,

a. The stair-like distributions of dimensionless tensile stresses derived from the DEM model are consistent with the dimensionless tensile stress curves generated by the SC model of Wang et al. (2006) when the Poisson’s ratio is equal to zero. The comparison confirms the applicability of planar DEM model. The dimensionless tangential tensile stress curve

of Wang's model deviated from the corresponding stair-like stress distribution as the Poisson's ratio was enhanced. The DEM model showed that the tangential tensile forces concentrating on contact regions between potash particles were much bigger than the radial tensile forces, and the major factor contributing to the fracture of potash ring samples. The almost uniform distribution of tangential tensile forces implies that the fracture surfaces of a potash ring sample are in agreement with the sample cross sections parallel to the radial direction.

b. The sample preparation process was used to generate potash specimens with steady initial caking properties, such as mass, height, and porosity, before external compression. The increase of external load and moisture adsorption relative humidity and the decrease of moisture desorption relative humidity resulted in larger variations in the caking properties of compressed specimens such as height, porosity, and moisture content. When the adsorption relative humidity does not exceed 75%, the higher external load and moisture adsorption humidity can cause the higher sample cake strength. As moisture adsorption relative humidity reaches 84%, an increased external load cannot enhance the cake strength of bulk potash.

c. The agreement between the numerical results for sample moisture content and corresponding experimental data with their measurement uncertainties confirm the water vapour diffusion model with the boundary condition of free mass convection. Relative to the foregoing moisture adsorption of potash specimens, the moisture desorption can generate the higher free mass convection coefficients and efficient mass transfer near the top surfaces of potash specimens. This comparison can verify the observed result that the subsequent moisture desorption process can be completed faster than the foregoing adsorption process. The almost uniform spatial distributions of the maximum and residual local moisture contents signify nearly constant local moisture content differences and similar crystal bridges evenly spread in a potash specimen after drying. It is also implied that the two macroscopic parameters, the maximum and residual sample moisture content, can quantify the local moisture content at any position within a specimen respectively after moisture adsorption and desorption. The difference between numerical

results of residual sample moisture content and corresponding experimental data in the later moisture desorption stage indicates that a lower moisture desorption relative humidity can result in a faster drying rate and prevent more salt from recrystallizing in a potash specimen. However, relative to the final sample moisture content difference, the inhibited amount of recrystallized salt is trivial. The lower moisture desorption humidity causes more water to evaporate and more salt to recrystallize near contact regions between potash particles. When the moisture adsorption relative humidity is invariable and not higher than 75%, a lower desorption relative humidity can cause the stronger caking of bulk potash.

d. The cake strength of potash specimens can be predicted by a correlation relating it to the external equivalent load and ambient air relative humidity for moisture adsorption and desorption. The upper limits of external equivalent load and ambient air relative humidity for the correlation are 16 m and 75%. The correlation shows that the cake strength of a potash specimen has positive power-function relations with the moisture absorption relative humidity and the external equivalent load and a negative power-function relation with the moisture desorption relative humidity. If the moisture adsorption relative humidity reaches 84%, the correlation will be inapplicable. The deviation and agreement between the sample cake strength data and the correlation also imply that the crystal bridge uniformity in a potash specimen is the prerequisite for applications of the planar DEM model and the correlation.

6.3 Future Work

The objectives of this research have been accomplished by using the relevant numerical models and physical experiments. Some limitations have to be applied in this research. In the planar DEM model, idealized potash ellipsoidal and spherical particles in contact were used. Potash specimens were agglomerated in the single cyclic process of moisture adsorption and desorption. The water vapour diffusion model was only usable for uncompressed potash specimens. These limitations reveal that the numerical modelling and experimental testing with the consideration of the practical handling and storage of bulk potash should be tackled in future work. Specifically,

a. The simulation and experimentation on the formation of crystal bridges between potash particles should be a future objective. The physical properties of crystal bridges, such as geometry, Young's modulus, stiffness, strength, and so on, should be measured and predicted.

b. More levels of the moisture adsorption humidity between 75% and 84% and external equivalent loads from zero to 4 metres should be used to investigate the variations of bulk potash caking. The correlation of cake strength should be applicable over extensive ranges of external equivalent load and ambient air relative humidity.

c. The potash sample preparation process should be modified to prepare specimens caked in multiple cyclic courses of moisture adsorption and desorption. Variations on caking properties and cake strength of potash specimens in the multiple cyclic courses should be investigated.

d. The moisture transfer model should be developed to investigate the microscopic transportation behaviour of water vapour and condensed water inside a compressed potash specimen.

REFERENCES

ASHRAE, 2004 HVAC Systems and Equipment Handbook, ASHRAE, Atlanta.

ASME PTC 19.1 Uncertainty Analysis, 2005.

ASTM Standards, D6128-06, 2007 Standard Test Method for Shear Testing of Bulk Solids Using the Jenike Shear Cell, ASTM International, Pennsylvania, USA.

ASTM Standards, D6773-08, 2008 Standard Test Method for Bulk Solids Using Schulze Shear Tester, ASTM International, Pennsylvania, USA.

ASTM Standards, E104-02, 2007 Standard Practice for Maintaining Constant Relative Humidity by Means of Aqueous Solutions, ASTM International, Pennsylvania, USA.

Benenati, R.F. and Brosilow, C.B., 1962 Void Fraction Distribution in Packed Beds, AIChE J., Vol. 8, pp.359-361.

Budynas, R.G., 1999 Advanced Strength and Applied Stress Analysis, 2nd edition, McGraw-Hill, New York, NY.

Burch, D.M., Allen, R.W., Peavy, B.A., 1976 Transient Temperature Distributions within Porous Slabs Subjected to Sudden Transpiration Heating, ASME, Heat Transfer, Vol. 98, pp.221-225.

Chen, R. G., 2004 Measurement and Numerical Simulation of Moisture Transportation by Capillarity, Gravity and Diffusion in Porous Potash Beds, M.Sc Thesis, University of Saskatchewan.

Christakis, N., Wang, J., Patel, M. K., Bradley, M. S. A., Leaper, M. C., and Cross, M., 2006 Aggregation and Caking Processes of Granular Materials: Continuum Model and Numerical Simulation with Application to Sugar, Advanced Powder Technol., Vol. 17, No. 5, pp .543-565.

Coleman, H.W., Steele, W. G., 1999 Experimentation and Uncertainty Analysis for Engineers, 2nd edition, John Wiley & Sons, Inc., New York, USA.

Cundall, P.A. & Strack, O.D., 1979 A Discrete Numerical Model for Granular Assemblies, Geotechnique, Vol. 29, No. 1, pp.47-65.

Felbeck, D.K., Atkins, A.G., 1984 Strength and Fracture of Engineering Solids, Prentice-Hall, Inc., Englewood Cliffs.

Garrett, D.E., 1996, Potash-Deposits, Processing, Properties, and Uses, 1st edition, Chapman & Hall, New York, NY.

Goldstein, R.J., Sparrow, E. M., and Jones, D. C., 1973 Natural Convection Mass Transfer Adjacent to Horizontal Plates, International Journal of Heat and Mass Transfer, Vol.16, pp.1025-1035.

Gröger, T., Tüzün, U., and Heyes, D. M., 2003 Modeling and Measuring of Cohesion in Wet Granular Materials, Powder Technology, Vol. 133, pp.203-215.

Hansen, L.D., Hoffmann, F., Strathdee, G., 1998 Effects of Anticaking Agents on the Thermodynamics and Kinetics of Water Sorption by Potash Fertilizers, Powder Technology, Vol. 98, pp.79-82.

Harr, M.E., 1977 Mechanics of Particulate Media, McGraw-Hill, Inc., USA.

Incropera, F.P., Dewitt, D.P., 1996 Fundamentals of Heat and Mass Transfer, 4th Ed, John Willey & Sons, New York.

Iwashita, K., Oda, M., 2000 Micro-deformation Mechanism of Shear Banding Process Based on Modified Distinct Element Method, Powder Technology, Vol. 109, pp.192-205.

Kaviany, M., 1995 Principles of Heat Transfer in Porous Media, 2nd edition, Springer-Verlag New York Inc., NY, USA.

Kawaguchi, T., Tanaka, T., and Tsuji, Y., 1998 Numerical Simulation of Two-Dimensional Fluidized Beds Using the Discrete Element Method (Comparison between the Two-and Three-Dimensional Models), Powder Technology, Vol. 96, pp.129-138.

Kruyt, N. P., Rothernburg, L., 2001 Statistics of the Elastic Behaviour of Granular Materials, International Journal of Solids and Structures, Vol. 38, pp.4879-4899.

Leaper, M. C., Bradley, M. S. A., Bridle, I., Reed, A. R., Abou-Chakra, H., and Tüzün, U., 2003 Measuring the Tensile Strength of Caked Sugar Produced from Humidity Cycling, Proc. Instn Mech. Engrs, Vol. 217, Part E, pp.41-47.

Li, J., Pandiella, S. S., Campbell, G. M., and Webb, C., 2003 Separation of Particulate Solids by Screening- A Discrete Particle Simulation, Numerical Modeling in Micromechanics via Particle Methods, Swets & Zeitlinger, Lisse, The Netherlands.

Minkowycz, W.J., Sparrow, E.M., Schneider, G.E., and Pletcher, R.H., 1988 Handbook of Numerical Heat Transfer, Wiley, New York.

Morrsion, H. L., Richmod, O., 1976 Sphere Flattening with Application to the Moderate Plastic Compaction of the Regular Sphere Assemblies, Powder Technology, Vol. 14, pp.153-160.

Ouwerkerk, C.E.D., 1991, A Micro-Mechanical Connection between the Single-Particle Strength and the Bulk Strength of Random Packing of Spherical Particles, Powder Technology, Vol. 65, pp.125-138.

Peng, S.W., Strathdee, Graeme, and Besant, R.W., 1999 Dissolution Reaction of Potash Fertilizer with Moisture, The Canadian Journal of Chemical Engineering, Vol. 77, pp.1127-1133

Peng, S.W., Besant, R.W., and Strathdee, Graeme, 2000 Heat and Mass Transfer in Granular Potash Fertilizer with a Surface Dissolution Reaction, The Canadian Journal of Chemical Engineering, Vol. 78, pp.1076-1086.

Peng, S.W., Besant, R.W., and Strathdee, Graeme, 2001 Measurement of the Enthalpy Change During Potash-Moisture Interactions, Int. J. Therm. Sci., Vol. 40, pp.586-594.

Rao, S.S., 2002 Applied Numerical Methods for Engineers and Scientists, Prentice Hall, NJ.

Rockland, L.B., 1960 Saturated Salt Solutions for Static Control of Relative Humidity between 5^{o} and 40^{o}C, Analytical Chemistry, Vol.32, No. 10, pp.1375-1376.

Rumpf, H., 1958 Grundlagen und Methoden des Granulierens. Chemie Ing. Tech., 30, pp.144-158.

Schulze, D., Hernrici, H. and Zetzener, H., 2001 The Ring Shear Tester as a Valuable Tool for Silo Design and Powder Characterization, Powder Handling and Processing, Vol. 13, No. 1, pp.19-24.

Schwedes, J., 2003 Review on Testers for Measuring Flow Properties of Bulk Solids, Granular Matter, Vol. 5, pp.1-43.

Schweiger, A., Zimmermann, I., 1999 A New Approach for the Measurement of the Tensile Strength of Powders, Powder Technology, Vol. 101, pp.7-15.

Seville, J., Tüzün, U., and Clift, R., 1997 Processing of Particulate Solids, 1^{st} edition, Chapman & Hall, London, UK.

Sun, J., Besant, R.W., and Evitts, R. W., 2006 Fracture Stress Measurements and Images of Caked Particles of KCl and NaCl, In the Proceedings of CHOPS-05 Conference.

Tanaka, T., 1978 Evaluating the Caking Strength of Powders, Ind. Eng. Chem. Prod. Res. Dev., Vol. 17, No. 3, pp.241-246.

Tomas, J., 2004 Fundamentals of Cohesive Powder Consolidation and Flow, Granular Matter, Vol. 6, pp.75-86.

Wahl, M., Bröckel, U., Brendel, L., Feise, H. J., Weigl, B., Röck, M., and Schwedes, J., 2008 Understanding Powder Caking: Predicting Caking Strength from Individual Particle Contacts, Powder Technology, Vol. 188, pp.147-152.

Walker, G.M., Holland, C.R., and Ahmad, M.N., 1999 Granular Fertilizer Agglomeration in Accelerated Caking Tests, Ind. Eng. Chem. Res., Vol. 38, pp.4100-4103.

Wang, Y., Besant, R.W., Evitts, R. W., and Dolovich, A. T., 2006 Measurement of Cake Strength in Potash Using a Centrifuge, Part. Part. Syst. Charact., Vol. 23, pp.339-407.

Wang, Y., Evitts, R. W., and Besant, R.W., 2008 Modeling Crystal Growth between Potash Particles near Contact Points during Drying Process. Part I: Problem Formulation, The Canadian Journal of Chemical Engineering, Vol. 86, pp.192-198.

Wang, Y., Evitts, R. W., and Besant, R.W., 2008 Modeling Crystal Growth between Potash Particles near Contact Points during Drying Process. Part II: Analysis, Result, and Comparison with Experimental Data, The Canadian Journal of Chemical Engineering, Vol. 86, pp.199-206.

Wang, Y., Evitts, R.W., and Besant, R.W., 2009 The Relationship between Cake Strength of Potash Fertilizer and Initial Moisture Content, Particle Size, and Drying Time, Particulate Science and Technology, Vol. 27, pp.166-176.

Wang, Y., 2006 Characterization of Caking and Cake Strength in a Potash Bed, M.Sc Thesis, University of Saskatchewan.

Zhou, Q., 2000 Measurement and Simulation of Transient Moisture and Heat Diffusion in a Potash Layer, M.Sc Thesis, University of Saskatchewan.

APPENDIX A

DEVELOPMENT OF COMPATIBILITY EQUATIONS

In the planar DEM model, ellipsoidal and spherical potash particles are regularly arranged as shown in Figure 2.1. As a caked particle system rotating in the centrifuge, potash particles are in force balance, which is shown in Equation (2-1). These particles and crystal bridges connecting them keep in geometric coordination with one another. In the appendix, coordination relations, that is, compatibility equations, between potash particles will be obtained by using the technique of complementary energy.

A.1 Complementary Energy

Budynas (1999) summarized the definition and relevant applications of complementary energy. Figure A-1 (a) shows a nonlinear locus of elastic force-deformation relation. The area of Region I in Figure A-1 (a) denotes the elastic work, W_e, with respect to the force, F, and the displacement, δ. That is,

$$W_e = \int_0^{\delta} F \cdot d\delta \tag{A-1}$$

Relative to the elastic work, W_e, the area of Region II in the same figure may be termed the complementary work, W_c, which is

$$W_c = \int_0^{F} \delta \cdot dF \tag{A-2}$$

The complementary energy, Φ, is defined to equal the complementary work. The complementary energy, Φ, may be written as,

$$\Phi = \int_0^F \delta \cdot dF \tag{A-3}$$

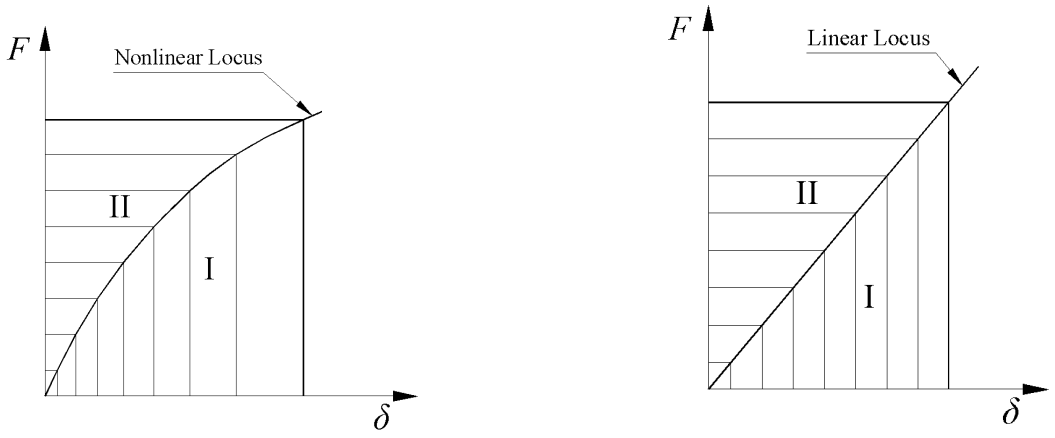

(a) (b)

Figure A-1 Schematics of elastic work and complementary energy: (a) the nonlinear force-deformation locus, (b) the linear force-deformation locus

For most cases, a quantity (q) of forces acts on a common object. The complementary energy may be expressed as,

$$\Phi = \sum_{k=1}^{q} \int \delta^k \cdot dF^k \tag{A-4}$$

If the k^{th} force, F^k, increase infinitesimally, that is, ΔF^k, the corresponding minute increment of the complementary energy, $\Delta\Phi$, is,

$$\Delta\Phi = \delta^k \cdot \Delta F^k \tag{A-5}$$

When the ΔF^k trend to zero, Equation (A-5) may be transformed to the expression of displacement, δ^k with respect to F^k,

$$\delta^k = \frac{\partial \Phi}{\partial F^k} \tag{A-6}$$

Equation (A-6) shows that the displacement, δ^k, caused by the force, F^k, equals the partial differential of the complementary energy with respect to the force, F^k.

A.2 Complementary Energy Application on Potash Particles

For caked potash particles, it is assumed that crystal bridges are subject to the linearly elastic force-deformation relation as shown in Figure A-1 (b). All of crystal bridges are considered to have the same Young's modulus, E, and bridge length, L, based on Assumption g in Section 2.2.1 of Chapter 2. Figure A-1 (b) shows that the area of Region II is equivalent to the area of Region I. In other words, the complementary energy in Equation (A-3) equals the elastic work in Equation (A-1). So, the tangential and radial complementary energy, Φ_t^i and Φ_r^i, acted on a particle in the i^{th} ring by crystal bridges in the tangential and radial directions may be respectively expressed as,

Complementary energy in the tangential direction

$$\Phi_t^i = \frac{1}{2}\frac{L\left(F_t^i\right)^2}{E \cdot A_t^i} \tag{A-7}$$

where A_t^i is defined as the cross section area of the tangential crystal bridge, equivalent to the area of the tangential contact region situating the tangential crystal bridge, A_{ct}^i (Refer to Appendix B).

Complementary energy in the radial direction

$$\Phi_r^i = \frac{1}{2}\frac{L\left(F_r^i\right)^2}{E \cdot A_r^i} \tag{A-8}$$

where A_r^i is defined as the cross section area of the radial crystal bridge, equivalent to the area of the radial contact region situating the radial crystal bridge, A_{cr}^i (Refer to Appendix B).

According to Equation (A-6), the partial differential of Equation (A-8) with respect to F_r^i is equivalent to the radial local displacement of the potash particle in the i^{th} ring, δ_r^i. That is,

$$\delta_r^i = \frac{F_r^i \cdot L}{E \cdot A_r^i} \tag{A-9}$$

The total complementary energy, Φ_s , for a group of ellipsoidal and spherical potash particles in the radial direction (Refer to Figure 2.1 (c)) is,

$$\Phi_s = \sum_{i=1}^{N} \Phi_t^i + \sum_{i=1}^{N-1} \Phi_r^i \tag{A-10}$$

Based on Equation (A-6), the total radial displacement of the potash particle in the i^{th} ring, δ_{rs}^i, equals the partial differential of Φ_s with respect to the centrifugal force, F_c^i , acting on the particle in the i^{th} ring,

$$\delta_{rs}^i = \frac{\partial \Phi_s}{\partial F_c^i} \tag{A-11}$$

According to the geometry of idealized potash particles in the radial direction inside the DEM model, the total radial displacement, δ_{rs}^i, of the particle in the i^{th} ring equals the summation of local radial displacements of the particles in the (i-1) rings and the radial translation, ΔR_{bi}, of the inner edge of the potash ring specimen. The expression is,

$$\delta_{rs}^i = \Delta R_{bi} + \sum_{l=1}^{i-1} \delta_r^l \tag{A-12}$$

Using Equation (A-9) and (A-11), Equation (A-12) can be rewritten as,

$$\frac{\partial \Phi_s}{\partial F_c^i} = \Delta R_{bi} + \sum_{l=1}^{i-1} \frac{F_r^l \cdot L}{E \cdot A_r^l} \tag{A-13}$$

Applying Equation (A-7), (A-8), (A-10), (A-13) and Equation (2-1), the group of equations concerning centrifugal, tangential and radial tensile forces can be expressed as,

$$\frac{\left(F_c^1 + F_r^1\right)\cdot L}{4\sin^2(\frac{\beta}{2})\cdot E\cdot A_t^1} = \Delta R_{bi}\,,\ (i=1) \tag{A-14}$$

$$\frac{\left(F_c^i + F_r^i - F_r^{i-1}\right)\cdot L}{4\sin^2(\frac{\beta}{2})\cdot E\cdot A_t^i} = \Delta R_{bi} + \sum_{j=1}^{i-1}\frac{F_r^j\cdot L}{A_r^j\cdot E},\ (i=2\cdots\cdots N-1) \tag{A-15}$$

$$\frac{\left(F_c^N - F_r^{N-1}\right)\cdot L}{4\sin^2(\frac{\beta}{2})\cdot E\cdot A_t^N} = \Delta R_{bi} + \sum_{j=1}^{N-1}\frac{F_r^j\cdot L}{A_r^j\cdot E},\ (i=N) \tag{A-16}$$

A.3 Equations for Compatibility

Because the angle β is very small (Figure 2.4), the following equation is valid,

$$\beta/2 \approx \sin(\beta/2) \tag{A-17}$$

Using Equation (2-1) and (A-17), Equation (A-14) to (A-16) can be transformed to Equation (2-3) in Chapter 2. That is,

$$-F_t^{i-1} - \frac{A_t^{i-1}}{A_r^{i-1}}\beta\cdot F_r^{i-1} + \frac{A_t^{i-1}}{A_t^i}F_t^i = 0\,,\ (i=1\cdots\cdots N) \tag{2-3}$$

APPENDIX B

DETERMINATION OF CONTACT AREAS BETWEEN IDEALIZED POTASH PARTICLES

During sample preparation, elastic and plastic deformations occur inside compressed potash specimens. The contact points between potash particles are changed to the corresponding contact regions. According to Assumption g in Section 2.2.1 of Chapter 2, the problem of determining the cross section areas of crystal bridges can be transformed into how to estimate the contact regions situating the crystal bridges between potash particles.

B.1 Particle Deformations Parallel to the External Force

The elastic stress-strain relations are used at contact points between potash particles when the entire specimen is subject to an external force. Figure B-1 indicates that the long axes of ellipsoidal particles are assumed to be perpendicular to the particle layer and parallel to the external load. The deformation and deflection of the top clamp cell under the external load can be neglected according to Assumption d in Section 2.2.1 of Chapter 2. Thus, all of potash particles have the same deformation in the direction of external compression in Figure B-1. That is,

$$\delta_{cl}^{1} = \ldots = \delta_{cl}^{i} = \ldots = \delta_{cl}^{N} \tag{B-1}$$

where the symbol, δ_{cl}^{i}, expresses the compressed deformation at the end of long axis of the potash particle in the i^{th} potash ring and N denotes the number of rings in the cell or the number of idealized potash particles in the radial direction.

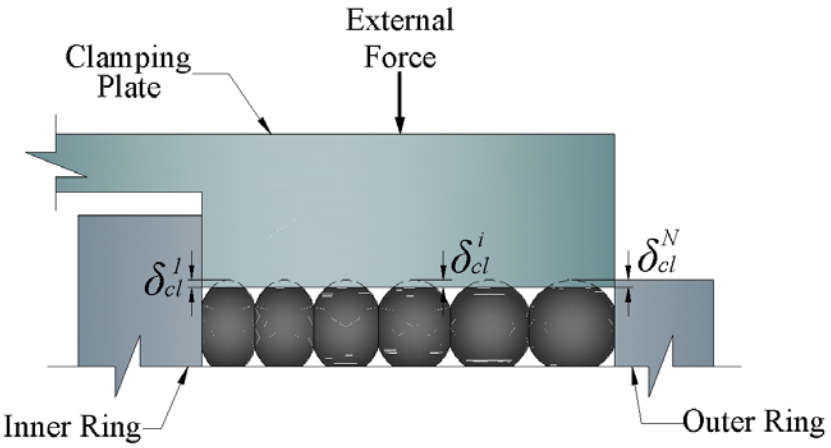

Figure B-1 Schematic for the DEM model under an exterior load

The three contact points on the pair of potash particles before compression are shown in Figure B-2. And the four dashed circles denote the curvature circles at the three contact points. The theory of Hertz stress (Budynas 1999) is applied to estimate the deformations and forces acting at the contact points. The contact regions between particles and the top clamp cell are considered to be circular planes because the cross sections normal to the long axes of a potash particle are round in shape. The contact regions at the ends of short axes of potash particles are thought of as elliptic planes because the cross sections normal to the short axes of potash particles are elliptic in shape.

The formula of deformation (δ_{cl}^{i}), shown in Figure B-3(a) at the long axis end of potash particle in the i^{th} potash ring is,

$$\delta_{cl}^{i} = \frac{(r_{cl}^{i})^2}{d_{pcl}^{i}} \tag{B-2}$$

where r_{cl}^{i} and d_{pcl}^{i} respectively denote the radius of contact region under compression (Refer to Figure B-3(a)) and the diameter of curvature circle at the end of long axis of Particle *i* before compression (Refer to Figure B-2).

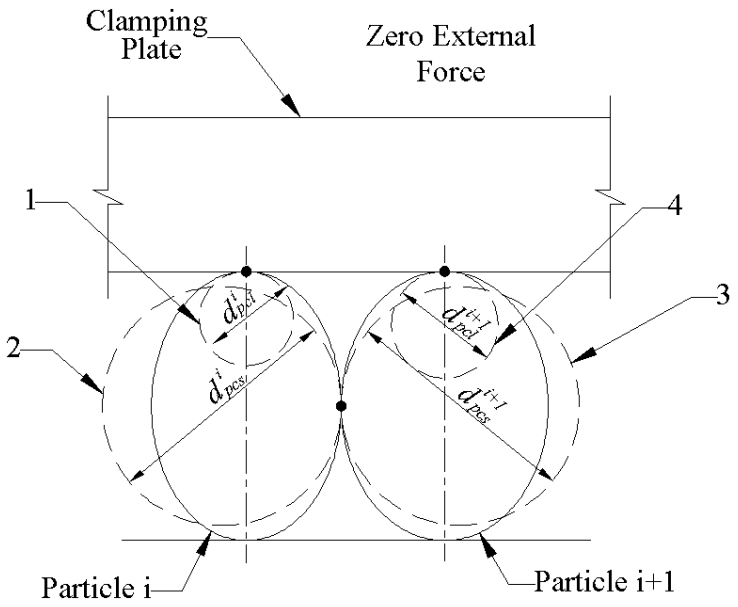

Figure B-2 Contact points on potash particles and their curvature circles without external forces: 1-- the curvature circle for the contact point at the long axis end of Particle *i*, 2-- the curvature circle for the contact point at the short axis end of Particle *i*, 3-- the curvature circle for the contact point at the short axis end of Particle *i+1*, 4-- the curvature circle for the contact point at the long axis end of Particle *i+1*

The curvature circle diameter (d^i_{pcl}) as shown in Figure B-2 is expressed by the short and long diameters of Particle *i*, d^i_p and d^N_p, before compression,

$$d^i_{pcl} = \frac{(d^i_p)^2}{2 \cdot d^N_p} \tag{B-3}$$

In Figure B-3(a), the compressive contact force (P^i_c), located on Particle *i*, can cause a deformed region at the contact point. The radius of contact region (r^i_{cl}) is also written as,

$$r_{cl}^{i} = \left\{ \frac{3}{8} P_{c}^{i} \cdot d_{pcl}^{i} \frac{1-(\upsilon_{p})^{2}}{E_{p}} \right\}^{\frac{1}{3}} \tag{B-4}$$

where υ_p is the Poisson's ratio of potash particle and E_p is the Young's modulus of potash particle.

Through Equation (B-2), (B-3), and (B-4), the compressive contact force (P_c^i) acting on Particle *i* is expressed as,

$$P_{c}^{i} = \frac{8}{3} \cdot \frac{E_{p}}{1-(\upsilon_{p})^{2}} \cdot (2 \cdot d_{p}^{N})^{-\frac{1}{2}} \cdot \delta_{cl}^{i\frac{3}{2}} \cdot d_{pcl}^{i} \tag{B-5}$$

The summation of compressive contact forces acting on potash particles in the radial direction equals the external load (F_{el}),

$$F_{el} = n \cdot \sum_{i=1}^{N} P_{c}^{i} \tag{B-6}$$

where *n* is the number of potash particles in a ring.

Meanwhile, the external load is caused by a high potash pile. It may be expressed as,

$$F_{el} = \rho_{b} \cdot g \cdot H \cdot \pi \cdot [(R_{bo})^{2} - (R_{bi})^{2}] \tag{B-7}$$

where ρ_b is the density of potash specimen, *g* is the gravitational acceleration, *H* is the height of potash pile, R_{bi} and R_{bo} are respectively the interior and exterior radii of a potash specimen.

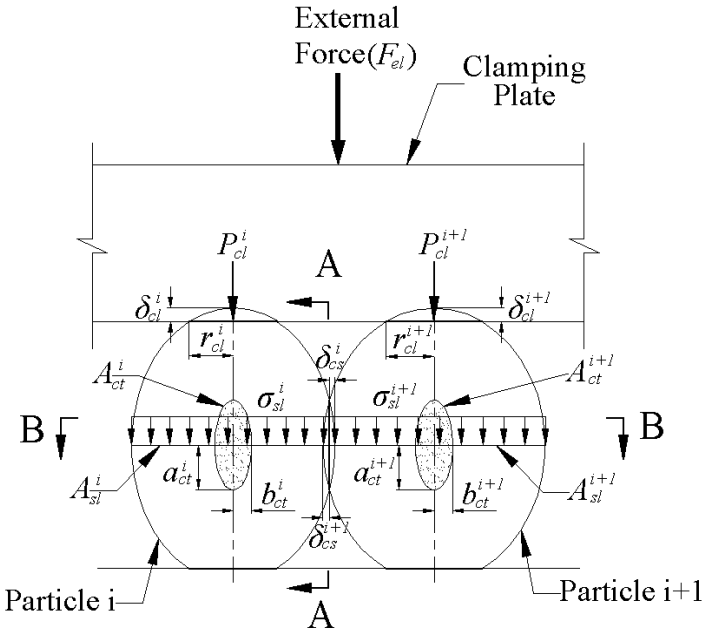

(a)

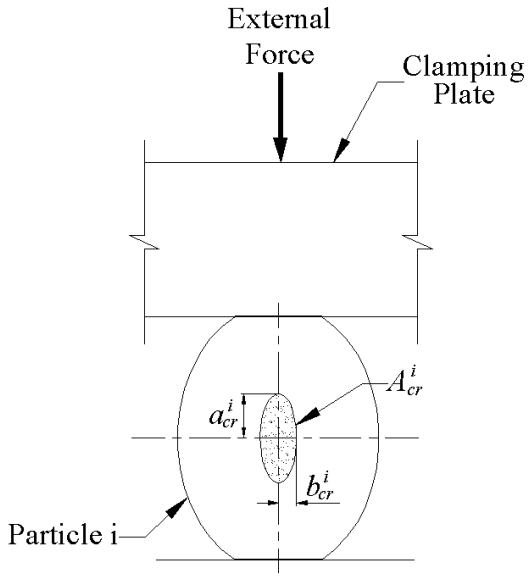

Section A-A

(b)

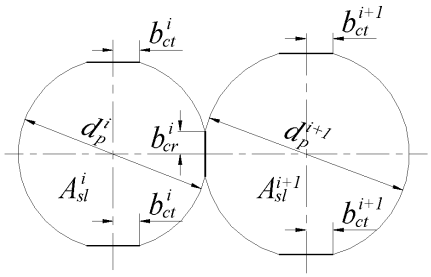

Section B-B

(c)

Figure B-3 Schematics of contacts between compressed potash particles: (a) concentrated forces, uniform stresses, and deformations on potash particles, (b) the contact region at short axis ends of potash particles, (c) the cross sections through the short axes of potash particles

Combining Equation (B-6) and (B-7) gives the force balance equation,

$$n \cdot \sum_{i=1}^{N} P_c^i = \rho_b \cdot g \cdot h \cdot \pi[(R_{bo})^2 - (R_{bi})^2] \tag{B-8}$$

Substituting Equation (B-1) and (B-5) into Equation (B-8) gives an expression for the deformation at the long axis end of the potash particle in the i^{th} ring,

$$\delta_{cl}^i = \left\{ \frac{3\left[1-(\upsilon_p)^2\right] \cdot (2d_p^N)^{\frac{1}{2}} \cdot \rho_b \cdot g \cdot h \cdot \pi\left[(R_{bo})^2 - (R_{bi})^2\right]}{8n \cdot E_p \cdot \sum_{i=1}^{N} d_{pcl}^i} \right\}^{\frac{2}{3}} \tag{B-9}$$

Now, substituting Equation (B-3) and (B-9) into Equation (B-5) can calculate the corresponding compressive contact force (P_c^i).

B.2 Particle Deformations Perpendicular to the External Force

In this step, the compressed deformations at the short axis ends of potash particles are determined. Because the cross section through the short axis of a particle is far from the long axis end of the particle as shown in Figure B-3(a), the average compressive stress can be used to index the stress state on the cross section.

The compressive stress, σ_{sl}^i, uniformly distributed on the cross section through the short axis of Particle *i* (Refer to Figure B-3(a)) may be written as,

$$\sigma_{sl}^i = \frac{P_c^i}{A_{sl}^i} \tag{B-10}$$

where A_{sl}^i denotes the cross section area relative to σ_{sl}^i .

Based on Hook's law, the compressive strain (ε_{sl}^{i}) caused by the compressive stress (σ_{sl}^{i}) can be written as,

$$\varepsilon_{sl}^{i} = \frac{\sigma_{sl}^{i}}{E_p} \tag{B-11}$$

When a potash particle, as elastic continuum, is compressed in the direction parallel to its long axis, the corresponding stress (σ_{sl}^{i}) can also result in an extra strain (ε_{ss}^{i}) in the short axis directions of the particle. The strain (ε_{ss}^{i}) can be determined by the Poisson's ratio (υ_p),

$$\varepsilon_{ss}^{i} = \upsilon_p \cdot \varepsilon_{sl}^{i} \tag{B-12}$$

Consequently, the deformation (δ_{cs}^{i}) at the short axis end of Particle *i* (Refer to Figure B-3(a)) can be estimated by the strain (ε_{ss}^{i}),

$$\delta_{cs}^{i} = \varepsilon_{ss}^{i} \cdot \frac{d_p^{i}}{2} \tag{B-13}$$

B.3 Contact Areas between Potash Particles

As shown in Figure B-3(b) & (c), the stretched strain (ε_{ss}^{i}) causes the contact regions at the short axis ends of Particle *i*. The contact regions are considered to be elliptic planes.

The tangential contact area (A_{ct}^{i}) between two same particles in the i^{th} ring in Figure B-3 (a) is,

$$A_{ct}^{i} = \pi \cdot a_{ct}^{i} \cdot b_{ct}^{i} \tag{B-14}$$

where a_{ct}^{i} and b_{ct}^{i} are the long and short radii of the ellipse shown in Figure B-3(a) and (c).

Using Hertz stress theory with curvature circles at contact points, the long and short radii will be respectively,

$$a_{ct}^{i} = \sqrt{\delta_{cs}^{i} \cdot d_{p}^{i}} \tag{B-15}$$

$$b_{ct}^{i} = d_{p}^{N} \cdot \sqrt{\frac{\delta_{cs}^{i}}{d_{p}^{i}}} \tag{B-16}$$

Substituting Equation (B-15) and (B-16) into Equation (B-14) gives the expression of the tangential contact area,

$$A_{ct}^{i} = \pi \cdot \delta_{cs}^{i} \cdot d_{p}^{N} \tag{B-17}$$

Equation (B-17) is similar to the equations of Morrsion et al. (1976) and Walker et al. (1999). It is shown that the Hertz stress theory can reasonably estimate the contact area between the same potash particles. Next, the theory can be used to obtain the expression for the contact area between two different potash particles.

As shown in Figure B-3(b), the radial contact area (A_{cr}^{i}) between two particles in the i^{th} and $(i+1)^{th}$ rings is,

$$A_{cr}^{i} = \pi \cdot a_{cr}^{i} \cdot b_{cr}^{i} \tag{B-18}$$

where a_{cr}^{i} and b_{cr}^{i} are respectively long and short radii of the ellipse contact region shown in Figure B-3(b).

The long and short radii will be respectively expressed as,

$$a_{cr}^{i} = \sqrt{\frac{d_{p}^{i} \cdot d_{p}^{i+1}}{d_{p}^{i} + d_{p}^{i+1}} \left(\delta_{cs}^{i} + \delta_{cs}^{i+1} \right)} \tag{B-19}$$

$$b_{cr}^{i} = d_{p}^{N} \cdot \sqrt{\frac{\delta_{cs}^{i} + \delta_{cs}^{i+1}}{d_{p}^{i} + d_{p}^{i+1}}} \tag{B-20}$$

Substituting Equation (B-19) and (B-20) into Equation (B-18) gives the expression of radial contact area:

$$A_{cr}^{i} = \frac{\pi \cdot d_{p}^{N} (\delta_{cs}^{i} + \delta_{cs}^{i+1})}{(d_{p}^{i} + d_{p}^{i+1})} \sqrt{d_{p}^{i} \cdot d_{p}^{i+1}} \tag{B-21}$$

Through calculations based on a series of equations mentioned above, it is found that all of the idealized potash particles have almost the same contact areas in tangential and radial directions because potash particles with a small diameter range from 0.9 to 1.18mm are selected in this research. Therefore, crystal bridges, situated on the same level inside a potash specimen, are considered to be almost the same.

APPENDIX C

UNCERTAINTY ANALYSIS OF EXPERIMENTAL DATA

Measured data of Experimental parameters are distributed around the corresponding true values. Multiple factors impact the deviations between measured data and true value of a parameter. The deviations may be classified into systematic biases and random errors. In this research, Test Uncertainty (ASME PTC 19.1, 2005) and the reference book of Coleman et al. (1999) are used to study these deviations and determine measurement uncertainties.

C.1 Calibration Data of Measurement Instruments

1. Caliper

Bias $=-4\times10^{-6}h^2+8\times10^{-4}h$, sample height ($h$) measurement range: 0 to 75mm

2. Tachometer

Bias: 1 *rpm*, Measurement range: 0 to 2000 *rpm*

3. Weight balance

Relative Bias: 0.04%, measurement range: 0 to 1 kg

4. Compressive springs

The force-deformation relation of springs before experiments is as follows,

$$F_s = 35.03\delta_s \tag{C-1}$$

The force-deformation relation of springs after experiments is as follows,

$$F_s = 34.11\delta_s \quad \text{(Force uncertainty: } \pm 25.8\ N\text{)} \tag{C-2}$$

where F_s and δ_s respectively denotes the force (N) and deformation (mm) on the springs.

Calibration uncertainty of spring forces: $U_{sc} = \pm 25.8N$ (C-3)

C.2 Uncertainty of Measured Parameters

The uncertainty analyses on experimental data are mainly determined by the instrumental biases and random errors. The random error, S, for a measured parameter, Z, is expressed as,

$$S = \left[\frac{\sum_{i=1}^{M} \left(Z_i - \overline{Z}\right)^2}{M-1} \right]^{1/2} \tag{C-4}$$

where the symbols, M and $\overline{Z}$, respectively denotes the reading number and mean value of the measured parameter. The mean value, $\overline{Z}$, is calculated by,

$$\overline{Z} = \frac{1}{M}\sum_{i=1}^{M} Z_i \tag{C-5}$$

The random error, $S_{\overline{Z}}$, for the mean value is expressed as,

$$S_{\overline{Z}} = \frac{S}{\sqrt{M}} \tag{C-6}$$

The uncertainty for the measured parameter, dominated by the biases and random errors, is,

$$U_{RSS} = \left[B^2 + \left(t \cdot S_{\bar{Z}}\right)^2\right]^{1/2} \quad \text{(C-7)}$$

where B denotes the instrumental biases and the coefficient, *t*, is the two-tailed Student *t* in the 95% confidence level. Because the biases of instruments, such as weight balance and tachometer, are very small, the uncertainties of sample mass and fracture rotary speed are mainly determined by their random errors.

C.3 Uncertainty of Calculated Quantities

1. Uncertainty Propagation

A parameter, y, is derived from a multivariable function, f, which can be written as,

$$y = f\left(x_1, x_2, \ldots x_n\right) \quad \text{(C-8)}$$

The parameter uncertainty (U_y) can be determined by the uncertainties and partial differentials of the measured variables ($x_1, x_2, \cdots x_n$). The formula is,

$$U_y = \left[\left(\frac{\partial f}{\partial x_1} U_{x_1}\right)^2 + \left(\frac{\partial f}{\partial x_2} U_{x_2}\right)^2 + \cdots + \left(\frac{\partial f}{\partial x_n} U_{x_n}\right)^2\right]^{\frac{1}{2}} \quad \text{(C-9)}$$

2. Uncertainty of External Loads

During sample preparation, the uncertainties of spring force are determined by the spring calibration uncertainty (Equation (C-2)) and the uncertainty propagated by the measurements of compressed spring deformation. Based on Equation (C-9), the propagated uncertainty (U_{se}) is calculated as,

$$U_{se} = 34.11 \cdot t \cdot S_{\bar{\delta}_s} \quad \text{(C-10)}$$

where $S_{\bar{\delta}_s}$ denotes the random error for the mean value of spring deformations.

Using Equation (C-3) and (C-10), the total uncertainty of spring force is expressed as,

$$U_{RSS} = \sqrt{U_{sc}{}^2 + U_{se}{}^2} \tag{C-11}$$

The total spring force uncertainty can be transformed to the uncertainty of equivalent potash pile depth by using Equation (B-7) and (C-9).

3. Uncertainty of Contact force and Stress in DEM Model

The centrifugal force, F_c^i, acting on a potash particle in the i^{th} ring is expressed as,

$$F_c^i = \frac{1}{6\varepsilon_{sd}} \pi \beta \rho_b d_p^N d_p^i \left(R_c^i\right)^2 \omega^2 \tag{C-12}$$

where the symbol, $\varepsilon_{sd,}$ is the volume fraction of solid potash particles in the DEM model and ρ_b denotes the mean density of a potash specimen. That is,

$$\rho_b = \frac{m}{\pi\left(R_{bo}{}^2 - R_{bi}{}^2\right)h} \tag{C-13}$$

where m is the sample mass, R_{bo}, R_{bi}, and h respectively denotes the outer and inner radii and height of the potash specimen.

Substituting Equation (C-13) into Equation (C-12) can obtain an expression of centrifugal force (F_c^i) with respect to the mean mass and fracture rotary speed of the potash specimen.

$$F_c^i = \eta_c^i m \omega^2 \tag{C-14}$$

The coefficient (η_c^i) is expressed as,

$$\eta_c^i = \frac{\beta d_p^N d_p^i \left(R_c^i\right)^2}{6\varepsilon_{sd} h\left(R_{bo}{}^2 - R_{bi}{}^2\right)} \tag{C-15}$$

In the DEM model, a group of idealized potash particles constitute the ring potash bed. A linear equation group (Equation (C-16)) has been found to obtain the solution about the tensile contact forces between these particles.

$$\begin{bmatrix} a_{1,1} & a_{1,2} & \cdots & a_{1,2N-1} \\ a_{2,1} & a_{2,2} & \cdots & a_{2,2N-1} \\ \ddots & & & \\ & \ddots & & \\ & & \ddots & \\ & & & \ddots \\ a_{2N-1,1} & a_{2N-1,2} & \cdots & a_{2N-1,2N-1} \end{bmatrix} \begin{bmatrix} F_t^1 \\ F_r^1 \\ F_t^2 \\ F_r^2 \\ \vdots \\ F_r^{N-1} \\ F_t^N \end{bmatrix} = \begin{bmatrix} F_c^1 \\ 0 \\ F_c^2 \\ 0 \\ \vdots \\ 0 \\ F_c^N \end{bmatrix} \tag{C-16}$$

Assumed that,

$$\begin{bmatrix} b_{1,1} & b_{1,2} & \cdots & b_{1,2N-1} \\ b_{2,1} & b_{2,2} & \cdots & b_{2,2N-1} \\ \ddots & & & \\ & \ddots & & \\ & & \ddots & \\ & & & \ddots \\ b_{2N-1,1} & b_{2N-1,2} & \cdots & b_{2N-1,2N-1} \end{bmatrix} = \begin{bmatrix} a_{1,1} & a_{1,2} & \cdots & a_{1,2N-1} \\ a_{2,1} & a_{2,2} & \cdots & a_{2,2N-1} \\ \ddots & & & \\ & \ddots & & \\ & & \ddots & \\ & & & \ddots \\ a_{2N-1,1} & a_{2N-1,2} & \cdots & a_{2N-1,2N-1} \end{bmatrix}^{-1} \tag{C-17}$$

$$\begin{bmatrix} F_t^1 \\ F_r^1 \\ F_t^2 \\ F_r^2 \\ \\ F_r^{N-1} \\ F_t^N \end{bmatrix} = \begin{bmatrix} b_{1,1} & b_{1,2} & \cdots & b_{1,2N-1} \\ b_{2,1} & b_{2,2} & \cdots & b_{2,2N-1} \\ \ddots & & & \\ & \ddots & & \\ & & \ddots & \\ & & & \ddots \\ b_{2N-1,1} & b_{2N-1,2} & \cdots & b_{2N-1,2N-1} \end{bmatrix} \begin{bmatrix} F_c^1 \\ 0 \\ F_c^2 \\ 0 \\ \vdots \\ 0 \\ F_c^N \end{bmatrix} \tag{C-18}$$

Substituting Equation (C-14) into Matrix (C-18), tangential and radial tensile contact forces (F_t^i & F_r^i) are respectively expressed as,

$$F_t^i = \eta_t^i m\omega^2 \tag{C-19}$$

$$F_r^i = \eta_r^i m\omega^2 \tag{C-20}$$

where the coefficients (η_t^i & η_r^i) are separately expressed as,

$$\eta_t^i = \eta_c^i \sum_{j=1}^{N} b_{2i-1,2j-1} \tag{C-21}$$

$$\eta_r^i = \eta_c^i \sum_{j=1}^{N} b_{2i,2j-1} \tag{C-22}$$

Using Equation (C-9), the uncertainties of tangential and radial contact forces are expressed as,

$$U_{F_t^i} = \left[\left(\eta_t^i \omega^2 U_m \right)^2 + \left(2\eta_t^i m\omega U_\omega \right)^2 \right]^{\frac{1}{2}} \tag{C-23}$$

$$U_{F_r^i} = \left[\left(\eta_r^i \omega^2 U_m \right)^2 + \left(2\eta_r^i m\omega U_\omega \right)^2 \right]^{\frac{1}{2}} \tag{C-24}$$

According to Section 2.2.5 in Chapter 2, the uncertainties of tangential and radial tensile stresses are as follows,

$$U_{\sigma_t^i} = \frac{U_{F_t^i}}{A_p^i} \tag{C-25}$$

$$U_{\sigma_r^i} = \frac{U_{F_r^i}}{A_p^i} \tag{C-26}$$

APPENDIX D

DATA ANALYSES OF POTASH SPECIMENS

D.1 Sample mass

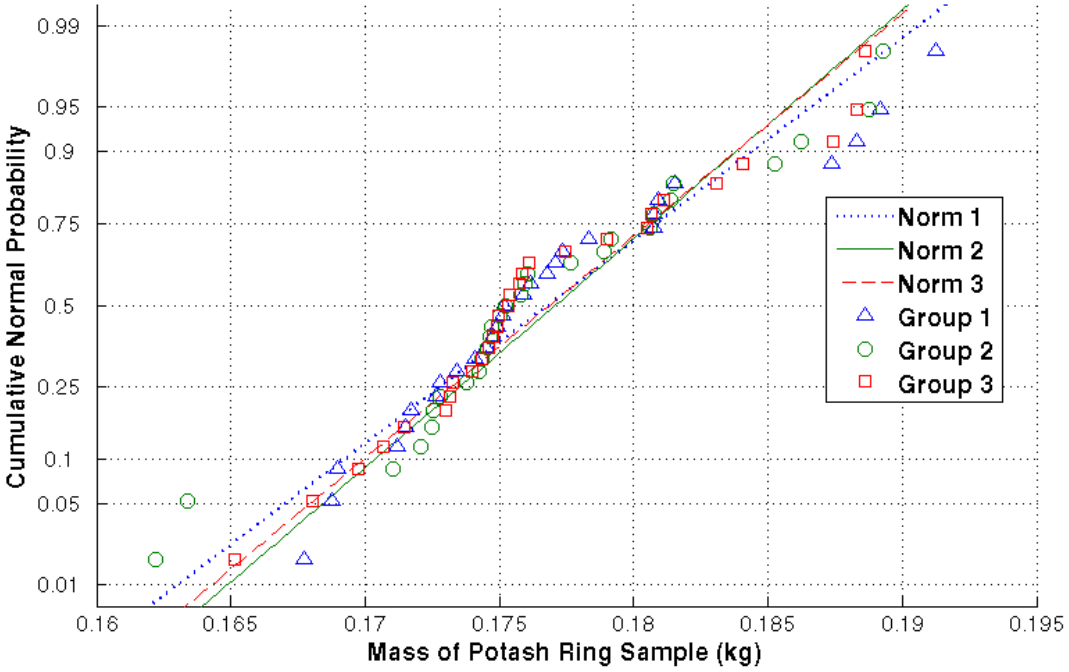

Figure D-1 Normality tests of the initial sample mass (m_i) for three groups of about 30 potash specimens with three external loads shown in Table 3.3

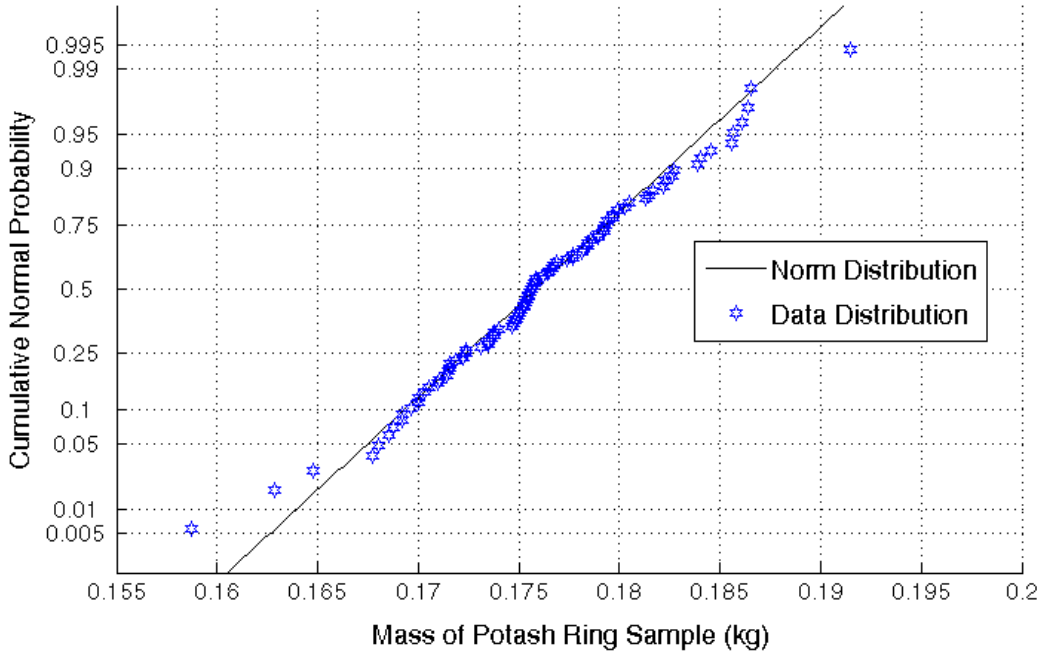

Figure D-2 Normality test of the initial sample mass (m_i) for all of over 90 potash specimens

D.2 Sample height

Table D-1 Two-factor statistical analysis on post-desorption compressed height (h_{cd})

			Moisture Adsorption Relative Humidity ϕ_A			**Total**
			69%	75%	84%	
Nominal sample depth (m)	4	Count	9	9	9	27
		Sum	2.50×10^{-1}	2.43×10^{-1}	2.50×10^{-1}	7.43×10^{-1}
		Average	2.78×10^{-2}	2.70×10^{-2}	2.78×10^{-2}	2.75×10^{-2}
		Variance	1.91×10^{-8}	5.75×10^{-8}	2.82×10^{-7}	2.49×10^{-7}
	8	Count	9	9	9	27
		Sum	2.42×10^{-1}	2.43×10^{-1}	2.42×10^{-1}	7.27×10^{-1}
		Average	2.69×10^{-2}	2.70×10^{-2}	2.69×10^{-2}	2.69×10^{-2}
		Variance	1.19×10^{-7}	1.24×10^{-7}	2.54×10^{-7}	1.58×10^{-7}
Total		Count	18	18	18	
		Sum	4.93×10^{-1}	4.86×10^{-1}	4.92×10^{-1}	
		Average	2.74×10^{-2}	2.70×10^{-2}	2.73×10^{-2}	
		Variance	2.68×10^{-7}	8.53×10^{-8}	4.67×10^{-7}	

ANOVA						
Source of Variation	SS	df	MS	F	P-value	F crit
Rows	4.64×10^{-6}	1	4.64×10^{-6}	32.54	7.06×10^{-7}	4.04
Columns	1.26×10^{-6}	2	6.30×10^{-7}	4.42	1.73×10^{-2}	3.19
Interaction	2.47×10^{-6}	2	1.23×10^{-6}	8.65	6.18×10^{-4}	3.19
Within	6.85×10^{-6}	48	1.43×10^{-7}			
Total	1.52×10^{-5}	53				

D.3 Sample porosity

Table D-2 Two-factor statistical analysis on the post-desorption compressed porosity (ε_{cd})

			Moisture Adsorption Relative Humidity ϕ_A			**Total**
			69%	75%	84%	
Nominal sample depth (m)	4	Count	9	9	9	27
		Sum	3.615	3.625	3.606	10.847
		Average	0.402	0.403	0.401	0.402
		Variance	2.61×10^{-5}	1.23×10^{-4}	1.29×10^{-4}	8.65×10^{-5}
	8	Count	9	9	9	27
		Sum	3.356	3.649	3.435	10.440
		Average	0.373	0.405	0.382	0.387
		Variance	8.17×10^{-4}	1.48×10^{-4}	5.15×10^{-4}	6.51×10^{-4}
Total		Count	18	18	18	
		Sum	6.971	7.274	7.041	
		Average	0.387	0.404	0.391	
		Variance	6.16×10^{-4}	1.29×10^{-4}	3.99×10^{-4}	
ANOVA						
Source of Variation	SS	df	MS	F	P-value	F crit
Rows	3.07×10^{-3}	1	3.07×10^{-3}	10.47	2.20×10^{-3}	4.04
Columns	2.80×10^{-3}	2	1.40×10^{-3}	4.77	1.29×10^{-2}	3.19
Interaction	2.33×10^{-3}	2	1.16×10^{-3}	3.97	2.54×10^{-2}	3.19
Within	1.41×10^{-2}	48	2.93×10^{-4}			
Total	2.23×10^{-2}	53				

APPENDIX E

PHYSICAL PROPERTIES FOR WATER VAPOUR DIFFUSION MODEL

Physical Properties	References
$\rho_s = 1987 kg/m^3$	Garrett, Donald E., 1996 "Potash", Saline Processors
$\rho_l = 997 kg/m^3$	Incropera, F.P., Dewitt, D.P., 1996 "Fundamentals of Heat and Mass Transfer", 4th Ed, New York, John Willey & Sons
$\nu = 1.589 \times 10^{-5} m^2/s$	
$P_{atm} = 101325 Pa$	
$R = 8.315 kJ/(kmol \cdot K)$	
$D_v = 2.6 \times 10^{-5} m^2/s$	
$\varepsilon_g = 0.43$	Experimental Data
$\tau = 1.33$	Chen, R.G. 2004 M.Sc Thesis
$R_{bo} = 0.0775 m$	Design Size
$R_{bi} = 0.0655 m$	Design Size
$R_a = R/M_a = 287 J/(kg \cdot K)$	
$R_v = R/M_v = 462 J/(kg \cdot K)$	
$P_{sv} = C_1/T + C_2 + C_3 T + C_4 T^2 + C_5 T^3 + C_6 \ln T$ $C_1 = 5.8002206 \times 10^3$, $C_2 = 1.3914993$, $C_3 = 4.8640239 \times 10^{-2}$, $C_4 = 4.1764768 \times 10^{-5}$, $C_5 = 1.4452093 \times 10^{-8}$, $C_6 = 6.5459673$	2004 ASHRAE HVAC Systems and Equipment Handbook

APPENDIX F

FINITE DIFFERENCE OF WATER VAPOUR DIFFUSION MODEL

F.1 Discretion of equations

Governing equation:

$$\frac{\varepsilon_{g,i}^{n,k}-\varepsilon_{g,i}^{n-1}}{\Delta t}\rho_{v,i}^{n}+\varepsilon_{g,i}^{n}\frac{\rho_{v,i}^{n,k}-\rho_{v,i}^{n-1}}{\Delta t}-\dot{m}=\frac{D_{V,eff,i+1}^{n,k}-D_{V,eff,i-1}^{n,k}}{2\Delta x}\frac{\rho_{V,i+1}^{n,k}-\rho_{V,i-1}^{n,k}}{2\Delta x}+D_{V,eff,i}^{n,k}\frac{\rho_{V,i+1}^{n,k}-2\rho_{V,i}^{n,k}+\rho_{V,i-1}^{n,k}}{(\Delta x)^2}$$

Continuity equation:

$$\rho_l\frac{\varepsilon_{l,i}^{n,k}-\varepsilon_{l,i}^{n-1}}{\Delta t}+\dot{m}=0$$

Boundary conditions:

The bottom boundary: $\dfrac{-3\rho_{V,0}^{n,k}+4\rho_{V,1}^{n,k}-\rho_{V,2}^{n,k}}{2\Delta x}=0$

The top boundary: $D_{V,eff,N}^{n,k}\dfrac{\rho_{V,N-2}^{n,k}-4\rho_{V,N-1}^{n,k}+3\rho_{V,N}^{n,k}}{2\Delta x}=h_m(\rho_\infty-\rho_{V,N}^{n,k})$

F.2 Algorithm

Gauss-Seidel iteration

$$\hat{\rho}_i^{k+1}=\frac{1}{a_{ii}}(c_i-\sum_{j=1}^{i-1}a_{ij}\rho_j^{k+1}-\sum_{j=i+1}^{n}a_{ij}\rho_j^{k})$$

$$\rho_i^{k+1}=\rho_i^{k}+\omega\left(\hat{\rho}_i^{k+1}-\rho_i^{k}\right)\qquad(0<\omega<1)$$

Criterion of convergence:

$$\sum_{i=0}^{N}\frac{\left|\rho_i^{k}-\rho_i^{k-1}\right|}{(N-1)(\rho_{\max}-\rho_{\min})}\le\varepsilon_c\qquad(\varepsilon_c<10^{-7})$$

APPENDIX G

SELECTION OF GRID SIZES AND TIME STEPS IN MOISTURE DIFFUSION SIMULATIONS

In the water vapour diffusion model, the grid size and time step are mainly sensitive to the internal properties of the model. Both of Model (a) and (b) have the similar internal properties of potash specimens except the complete and reduced top sample surfaces exposed to the ambient air. Thus, Model (a) is selected for the sensitivity analyses of grid size and time step.

G.1 Grid size

In the local volume-averaging technique of Kaviany (1991), the grid size of averaged elementary volume should not be smaller than the mean value of particle size of bulk potash particles. In this research, the average particle size of potash specimens approximates to 1*mm*. In Figure G-1, the numerical solutions of local moisture contents with the grid size of 1*mm* deviates from the numerical curves with the two grid sizes of 0.5*mm* and 0.25*mm*. The water vapour diffusion model with the grid size of 1*mm* generates a mass balance error bigger than 1% as shown in Figure G-1. The model cannot select 1mm as its grid size.

As shown in Figure G-1, the model generates the two consistent curves of local moisture content with the reasonable mass balance errors as the grid size equals 0.5*mm* and 0.25*mm*. The grid size, 0.5*mm*, equivalent to a half of average potash particle diameter, may be used as the typical grid size of unit element representing the microscopic structures inside a potash specimen, relative to the smaller grid size, 0.25*mm*. So, the grid size, 0.5*mm*, will be used in the following simulations.

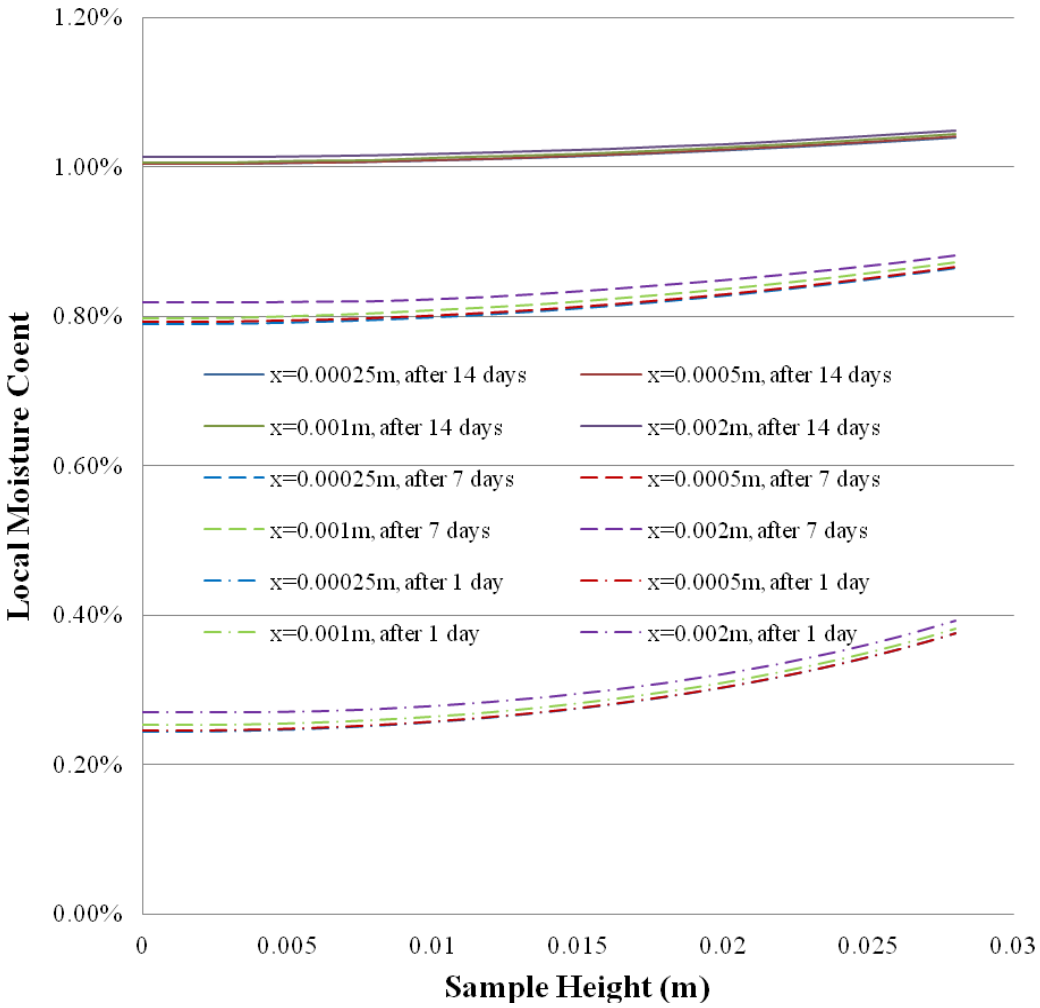

Figure G-1 Spatial distributions of local moisture content in a potash specimen for Model (a) with the four grid sizes (Error of mass balance: 0.04%@x=0.00025m, 0.3%@x=0.0005m, 2.6%@x=0.001m, 6.8%@x=0.002m)

G.2 Time step

With the grid size of 0.5mm, the four time steps, 24s, 12s, 6s, and 3s, are used in the water vapour diffusion model to obtain the numerical curves of sample moisture content plotted in Figure G-2. The plot shows that the water vapour diffusion model is not sensitive to variations of the time step when the time step decreases to 6s because the two numerical curves corresponding to the time steps of 6s and 3s are consistent with one another. The time step, 6s, will be used for the simulations of moisture adsorption and desorption in potash specimens.

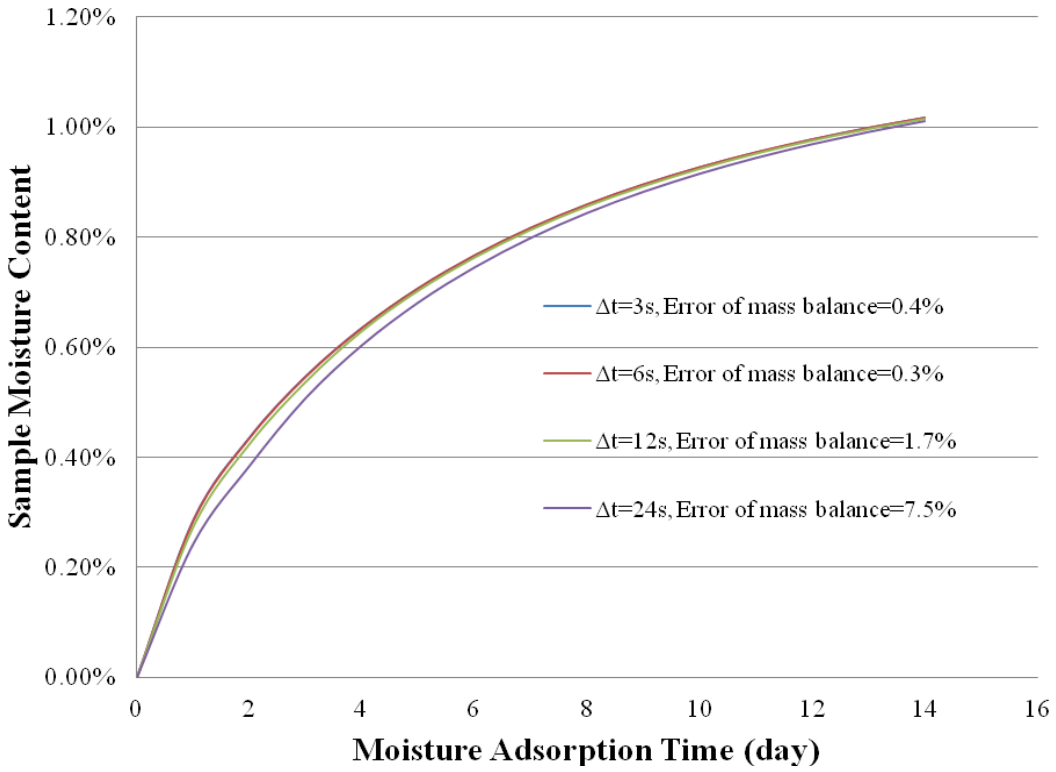

Figure G-2 Sample moisture content variation of Model (a) over moisture adsorption time with the four time steps